FERMILAB-PUB-11-547-E

Measurement of the inclusive jet cross section in $p\bar{p}$ collisions at $\sqrt{s} = 1.96$ TeV

V.M. Abazov,[35] B. Abbott,[73] B.S. Acharya,[29] M. Adams,[49] T. Adams,[47] G.D. Alexeev,[35] G. Alkhazov,[39] A. Alton[a],[61] G. Alverson,[60] G.A. Alves,[2] M. Aoki,[48] A. Askew,[47] B. Åsman,[41] S. Atkins,[58] O. Atramentov,[65] K. Augsten,[10] C. Avila,[8] J. BackusMayes,[80] F. Badaud,[13] L. Bagby,[48] B. Baldin,[48] D.V. Bandurin,[47] S. Banerjee,[29] E. Barberis,[60] P. Baringer,[56] J. Barreto,[3] J.F. Bartlett,[48] U. Bassler,[18] V. Bazterra,[49] A. Bean,[56] M. Begalli,[3] C. Belanger-Champagne,[41] L. Bellantoni,[48] S.B. Beri,[27] G. Bernardi,[17] R. Bernhard,[22] I. Bertram,[42] M. Besançon,[18] R. Beuselinck,[43] V.A. Bezzubov,[38] P.C. Bhat,[48] V. Bhatnagar,[27] G. Blazey,[50] S. Blessing,[47] K. Bloom,[64] A. Boehnlein,[48] D. Boline,[70] E.E. Boos,[37] G. Borissov,[42] T. Bose,[59] A. Brandt,[76] O. Brandt,[23] R. Brock,[62] G. Brooijmans,[68] A. Bross,[48] D. Brown,[17] J. Brown,[17] X.B. Bu,[48] M. Buehler,[48] V. Buescher,[24] V. Bunichev,[37] S. Burdin[b],[42] T.H. Burnett,[80] C.P. Buszello,[41] B. Calpas,[15] E. Camacho-Pérez,[32] M.A. Carrasco-Lizarraga,[56] B.C.K. Casey,[48] H. Castilla-Valdez,[32] S. Chakrabarti,[70] D. Chakraborty,[50] K.M. Chan,[54] A. Chandra,[78] E. Chapon,[18] G. Chen,[56] S. Chevalier-Théry,[18] D.K. Cho,[75] S.W. Cho,[31] S. Choi,[31] B. Choudhary,[28] S. Cihangir,[48] D. Claes,[64] J. Clutter,[56] M. Cooke,[48] W.E. Cooper,[48] M. Corcoran,[78] F. Couderc,[18] M.-C. Cousinou,[15] A. Croc,[18] D. Cutts,[75] A. Das,[45] G. Davies,[43] K. De,[76] S.J. de Jong,[34] E. De La Cruz-Burelo,[32] F. Déliot,[18] R. Demina,[69] D. Denisov,[48] S.P. Denisov,[38] S. Desai,[48] C. Deterre,[18] K. DeVaughan,[64] H.T. Diehl,[48] M. Diesburg,[48] P.F. Ding,[44] A. Dominguez,[64] T. Dorland,[80] A. Dubey,[28] L.V. Dudko,[37] D. Duggan,[65] A. Duperrin,[15] S. Dutt,[27] A. Dyshkant,[50] M. Eads,[64] D. Edmunds,[62] J. Ellison,[46] V.D. Elvira,[48] Y. Enari,[17] H. Evans,[52] A. Evdokimov,[71] V.N. Evdokimov,[38] G. Facini,[60] T. Ferbel,[69] F. Fiedler,[24] F. Filthaut,[34] W. Fisher,[62] H.E. Fisk,[48] M. Fortner,[50] H. Fox,[42] S. Fuess,[48] A. Garcia-Bellido,[69] G.A García-Guerra[c],[32] V. Gavrilov,[36] P. Gay,[13] W. Geng,[15,62] D. Gerbaudo,[66] C.E. Gerber,[49] Y. Gershtein,[65] D. Gillberg,[6] G. Ginther,[48,69] G. Golovanov,[35] A. Goussiou,[80] P.D. Grannis,[70] S. Greder,[19] H. Greenlee,[48] Z.D. Greenwood,[58] E.M. Gregores,[4] G. Grenier,[20] Ph. Gris,[13] J.-F. Grivaz,[16] A. Grohsjean,[18] S. Grünendahl,[48] M.W. Grünewald,[30] T. Guillemin,[16] G. Gutierrez,[48] P. Gutierrez,[73] A. Haas[d],[68] S. Hagopian,[47] J. Haley,[60] L. Han,[7] K. Harder,[44] A. Harel,[69] J.M. Hauptman,[55] J. Hays,[43] T. Head,[44] T. Hebbeker,[21] D. Hedin,[50] H. Hegab,[74] J.G. Hegeman,[33] A.P. Heinson,[46] U. Heintz,[75] C. Hensel,[23] I. Heredia-De La Cruz,[32] K. Herner,[61] G. Hesketh[e],[44] M.D. Hildreth,[54] R. Hirosky,[79] T. Hoang,[47] J.D. Hobbs,[70] B. Hoeneisen,[12] M. Hohlfeld,[24] Z. Hubacek,[10,18] V. Hynek,[10] I. Iashvili,[67] Y. Ilchenko,[77] R. Illingworth,[48] A.S. Ito,[48] S. Jabeen,[75] M. Jaffré,[16] D. Jamin,[15] A. Jayasinghe,[73] R. Jesik,[43] K. Johns,[45] M. Johnson,[48] A. Jonckheere,[48] P. Jonsson,[43] J. Joshi,[27] A.W. Jung,[48] A. Juste,[40] K. Kaadze,[57] E. Kajfasz,[15] D. Karmanov,[37] P.A. Kasper,[48] I. Katsanos,[64] R. Kehoe,[77] S. Kermiche,[15] N. Khalatyan,[48] A. Khanov,[74] A. Kharchilava,[67] Y.N. Kharzheev,[35] J.M. Kohli,[27] A.V. Kozelov,[38] J. Kraus,[62] S. Kulikov,[38] A. Kumar,[67] A. Kupco,[11] T. Kurča,[20] V.A. Kuzmin,[37] J. Kvita,[9] S. Lammers,[52] G. Landsberg,[75] P. Lebrun,[20] H.S. Lee,[31] S.W. Lee,[55] W.M. Lee,[48] J. Lellouch,[17] L. Li,[46] Q.Z. Li,[48] S.M. Lietti,[5] J.K. Lim,[31] D. Lincoln,[48] J. Linnemann,[62] V.V. Lipaev,[38] R. Lipton,[48] Y. Liu,[7] A. Lobodenko,[39] M. Lokajicek,[11] R. Lopes de Sa,[70] H.J. Lubatti,[80] R. Luna-Garcia[f],[32] A.L. Lyon,[48] A.K.A. Maciel,[2] D. Mackin,[78] R. Madar,[18] R. Magaña-Villalba,[32] N. Makovec,[16] S. Malik,[64] V.L. Malyshev,[35] Y. Maravin,[57] J. Martínez-Ortega,[32] R. McCarthy,[70] C.L. McGivern,[56] M.M. Meijer,[34] A. Melnitchouk,[63] D. Menezes,[50] P.G. Mercadante,[4] M. Merkin,[37] A. Meyer,[21] J. Meyer,[23] F. Miconi,[19] N.K. Mondal,[29] G.S. Muanza,[15] M. Mulhearn,[79] E. Nagy,[15] M. Naimuddin,[28] M. Narain,[75] R. Nayyar,[28] H.A. Neal,[61] J.P. Negret,[8] P. Neustroev,[39] S.F. Novaes,[5] T. Nunnemann,[25] G. Obrant[‡],[39] J. Orduna,[78] N. Osman,[15] J. Osta,[54] G.J. Otero y Garzón,[1] M. Padilla,[46] A. Pal,[76] N. Parashar,[53] V. Parihar,[75] S.K. Park,[31] R. Partridge[d],[75] N. Parua,[52] A. Patwa,[71] B. Penning,[48] M. Perfilov,[37] Y. Peters,[44] K. Petridis,[44] G. Petrillo,[69] P. Pétroff,[16] R. Piegaia,[1] M.-A. Pleier,[71] P.L.M. Podesta-Lerma[g],[32] V.M. Podstavkov,[48] P. Polozov,[36] A.V. Popov,[38] M. Prewitt,[78] D. Price,[52] N. Prokopenko,[38] J. Qian,[61] A. Quadt,[23] B. Quinn,[63] M.S. Rangel,[2] K. Ranjan,[28] P.N. Ratoff,[42] I. Razumov,[38] P. Renkel,[77] M. Rijssenbeek,[70] I. Ripp-Baudot,[19] F. Rizatdinova,[74] M. Rominsky,[48] A. Ross,[42] C. Royon,[18] P. Rubinov,[48] R. Ruchti,[54] G. Safronov,[36] G. Sajot,[14] P. Salcido,[50] A. Sánchez-Hernández,[32] M.P. Sanders,[25] B. Sanghi,[48] A.S. Santos,[5] G. Savage,[48] L. Sawyer,[58] T. Scanlon,[43] R.D. Schamberger,[70] Y. Scheglov,[39] H. Schellman,[51] T. Schliephake,[26] S. Schlobohm,[80] C. Schwanenberger,[44] R. Schwienhorst,[62] J. Sekaric,[56] H. Severini,[73] E. Shabalina,[23] V. Shary,[18] A.A. Shchukin,[38] R.K. Shivpuri,[28] V. Simak,[10] V. Sirotenko,[48] P. Skubic,[73] P. Slattery,[69] D. Smirnov,[54] K.J. Smith,[67] G.R. Snow,[64] J. Snow,[72] S. Snyder,[71] S. Söldner-Rembold,[44] L. Sonnenschein,[21] K. Soustruznik,[9] J. Stark,[14] V. Stolin,[36] D.A. Stoyanova,[38] M. Strauss,[73] D. Strom,[49] L. Stutte,[48] L. Suter,[44] P. Svoisky,[73] M. Takahashi,[44] A. Tanasijczuk,[1] M. Titov,[18] V.V. Tokmenin,[35] Y.-T. Tsai,[69] K. Tschann-Grimm,[70] D. Tsybychev,[70] B. Tuchming,[18] C. Tully,[66] L. Uvarov,[39]

S. Uvarov,[39] S. Uzunyan,[50] R. Van Kooten,[52] W.M. van Leeuwen,[33] N. Varelas,[49] E.W. Varnes,[45] I.A. Vasilyev,[38] P. Verdier,[20] L.S. Vertogradov,[35] M. Verzocchi,[48] M. Vesterinen,[44] D. Vilanova,[18] P. Vokac,[10] M. Voutilainen[h],[64] H.D. Wahl,[47] M.H.L.S. Wang,[48] J. Warchol,[54] G. Watts,[80] M. Wayne,[54] M. Weber[i],[48] L. Welty-Rieger,[51] A. White,[76] D. Wicke,[26] M.R.J. Williams,[42] G.W. Wilson,[56] M. Wobisch,[58] D.R. Wood,[60] T.R. Wyatt,[44] Y. Xie,[48] R. Yamada,[48] W.-C. Yang,[44] T. Yasuda,[48] Y.A. Yatsunenko,[35] Z. Ye,[48] H. Yin,[48] K. Yip,[71] S.W. Youn,[48] J. Yu,[76] T. Zhao,[80] B. Zhou,[61] J. Zhu,[61] M. Zielinski,[69] D. Zieminska,[52] and L. Zivkovic[75]

(The D0 Collaboration*)

[1]*Universidad de Buenos Aires, Buenos Aires, Argentina*
[2]*LAFEX, Centro Brasileiro de Pesquisas Físicas, Rio de Janeiro, Brazil*
[3]*Universidade do Estado do Rio de Janeiro, Rio de Janeiro, Brazil*
[4]*Universidade Federal do ABC, Santo André, Brazil*
[5]*Instituto de Física Teórica, Universidade Estadual Paulista, São Paulo, Brazil*
[6]*Simon Fraser University, Vancouver, British Columbia, and York University, Toronto, Ontario, Canada*
[7]*University of Science and Technology of China, Hefei, People's Republic of China*
[8]*Universidad de los Andes, Bogotá, Colombia*
[9]*Charles University, Faculty of Mathematics and Physics, Center for Particle Physics, Prague, Czech Republic*
[10]*Czech Technical University in Prague, Prague, Czech Republic*
[11]*Center for Particle Physics, Institute of Physics, Academy of Sciences of the Czech Republic, Prague, Czech Republic*
[12]*Universidad San Francisco de Quito, Quito, Ecuador*
[13]*LPC, Université Blaise Pascal, CNRS/IN2P3, Clermont, France*
[14]*LPSC, Université Joseph Fourier Grenoble 1, CNRS/IN2P3, Institut National Polytechnique de Grenoble, Grenoble, France*
[15]*CPPM, Aix-Marseille Université, CNRS/IN2P3, Marseille, France*
[16]*LAL, Université Paris-Sud, CNRS/IN2P3, Orsay, France*
[17]*LPNHE, Universités Paris VI and VII, CNRS/IN2P3, Paris, France*
[18]*CEA, Irfu, SPP, Saclay, France*
[19]*IPHC, Université de Strasbourg, CNRS/IN2P3, Strasbourg, France*
[20]*IPNL, Université Lyon 1, CNRS/IN2P3, Villeurbanne, France and Université de Lyon, Lyon, France*
[21]*III. Physikalisches Institut A, RWTH Aachen University, Aachen, Germany*
[22]*Physikalisches Institut, Universität Freiburg, Freiburg, Germany*
[23]*II. Physikalisches Institut, Georg-August-Universität Göttingen, Göttingen, Germany*
[24]*Institut für Physik, Universität Mainz, Mainz, Germany*
[25]*Ludwig-Maximilians-Universität München, München, Germany*
[26]*Fachbereich Physik, Bergische Universität Wuppertal, Wuppertal, Germany*
[27]*Panjab University, Chandigarh, India*
[28]*Delhi University, Delhi, India*
[29]*Tata Institute of Fundamental Research, Mumbai, India*
[30]*University College Dublin, Dublin, Ireland*
[31]*Korea Detector Laboratory, Korea University, Seoul, Korea*
[32]*CINVESTAV, Mexico City, Mexico*
[33]*Nikhef, Science Park, Amsterdam, the Netherlands*
[34]*Radboud University Nijmegen, Nijmegen, the Netherlands and Nikhef, Science Park, Amsterdam, the Netherlands*
[35]*Joint Institute for Nuclear Research, Dubna, Russia*
[36]*Institute for Theoretical and Experimental Physics, Moscow, Russia*
[37]*Moscow State University, Moscow, Russia*
[38]*Institute for High Energy Physics, Protvino, Russia*
[39]*Petersburg Nuclear Physics Institute, St. Petersburg, Russia*
[40]*Institució Catalana de Recerca i Estudis Avançats (ICREA) and Institut de Física d'Altes Energies (IFAE), Barcelona, Spain*
[41]*Stockholm University, Stockholm and Uppsala University, Uppsala, Sweden*
[42]*Lancaster University, Lancaster LA1 4YB, United Kingdom*
[43]*Imperial College London, London SW7 2AZ, United Kingdom*
[44]*The University of Manchester, Manchester M13 9PL, United Kingdom*
[45]*University of Arizona, Tucson, Arizona 85721, USA*
[46]*University of California Riverside, Riverside, California 92521, USA*
[47]*Florida State University, Tallahassee, Florida 32306, USA*
[48]*Fermi National Accelerator Laboratory, Batavia, Illinois 60510, USA*
[49]*University of Illinois at Chicago, Chicago, Illinois 60607, USA*
[50]*Northern Illinois University, DeKalb, Illinois 60115, USA*
[51]*Northwestern University, Evanston, Illinois 60208, USA*
[52]*Indiana University, Bloomington, Indiana 47405, USA*

[53]Purdue University Calumet, Hammond, Indiana 46323, USA
[54]University of Notre Dame, Notre Dame, Indiana 46556, USA
[55]Iowa State University, Ames, Iowa 50011, USA
[56]University of Kansas, Lawrence, Kansas 66045, USA
[57]Kansas State University, Manhattan, Kansas 66506, USA
[58]Louisiana Tech University, Ruston, Louisiana 71272, USA
[59]Boston University, Boston, Massachusetts 02215, USA
[60]Northeastern University, Boston, Massachusetts 02115, USA
[61]University of Michigan, Ann Arbor, Michigan 48109, USA
[62]Michigan State University, East Lansing, Michigan 48824, USA
[63]University of Mississippi, University, Mississippi 38677, USA
[64]University of Nebraska, Lincoln, Nebraska 68588, USA
[65]Rutgers University, Piscataway, New Jersey 08855, USA
[66]Princeton University, Princeton, New Jersey 08544, USA
[67]State University of New York, Buffalo, New York 14260, USA
[68]Columbia University, New York, New York 10027, USA
[69]University of Rochester, Rochester, New York 14627, USA
[70]State University of New York, Stony Brook, New York 11794, USA
[71]Brookhaven National Laboratory, Upton, New York 11973, USA
[72]Langston University, Langston, Oklahoma 73050, USA
[73]University of Oklahoma, Norman, Oklahoma 73019, USA
[74]Oklahoma State University, Stillwater, Oklahoma 74078, USA
[75]Brown University, Providence, Rhode Island 02912, USA
[76]University of Texas, Arlington, Texas 76019, USA
[77]Southern Methodist University, Dallas, Texas 75275, USA
[78]Rice University, Houston, Texas 77005, USA
[79]University of Virginia, Charlottesville, Virginia 22901, USA
[80]University of Washington, Seattle, Washington 98195, USA

(Dated: October 17, 2011)

We present a measurement of the inclusive jet cross section using the Run II cone algorithm and data collected by the D0 experiment in $p\bar{p}$ collisions at a center-of-mass energy $\sqrt{s}$ =1.96 TeV, corresponding to an integrated luminosity of 0.70 fb^{-1}. The jet energy calibration and the method used to extract the inclusive jet cross section are described. We discuss the main uncertainties, which are dominated by the jet energy scale uncertainty. The results cover jet transverse momenta from 50 GeV to 600 GeV with jet rapidities in the range -2.4 to 2.4 and are compared to predictions using recent proton parton distribution functions. Studies of correlations between systematic uncertainties in transverse momentum and rapidity are presented.

PACS numbers: 13.87.Ce, 12.38.Qk

I. INTRODUCTION AND MOTIVATION

The measurement of the cross section for inclusive production of hadronic jets in hadron collisions provides stringent tests of quantum chromodynamics (QCD). The inclusive jet cross section in $p\bar{p}$ collisions for jets with large momentum transverse to the beam axis (p_T) is directly sensitive to the strong coupling constant (α_s) [1] and the parton distribution functions (PDFs) of the proton [2]. At the Tevatron $p\bar{p}$ collider, data are divided into two sets corresponding to Run I (1992—1996) and Run II (2002—2011). The increased $p\bar{p}$ center-of-mass energy between Run I ($\sqrt{s} = 1.8$ TeV) and Run II ($\sqrt{s} =$ 1.96 TeV) leads to a significant increase in the cross section at large p_T – a factor of three at $p_T \approx 550$ GeV, as shown in Fig. 1 obtained using the next-to-leading order (NLO) QCD calculation as implemented in NLOJET++ [3]. This increases the sensitivity to potential new observations such as quark compositeness and extra dimensions [4]. The integrated luminosity of the inclusive jet cross section measurement discussed in this Article exceeds the Run I luminosity by more than a factor of five, allowing for more stringent constraints on the PDFs. In Fig. 2 we show the different subprocesses that contribute to the inclusive jet cross section. In particular the gluon density can be further constrained using these data, since the gg and qg initial states contribute significantly to the cross section across almost the full p_T range of the measurement. The gluon distribution is still poorly known, especially for gluons carrying a large momentum

*with visitors from [a]Augustana College, Sioux Falls, SD, USA, [b]The University of Liverpool, Liverpool, UK, [c]UPIITA-IPN, Mexico City, Mexico, [d]SLAC, Menlo Park, CA, USA, [e]University College London, London, UK, [f]Centro de Investigacion en Computacion - IPN, Mexico City, Mexico, [g]ECFM, Universidad Autonoma de Sinaloa, Culiacán, Mexico, [h]Helsinki Institute of Physics, Helsinki, Finland, and [i]Universität Bern, Bern, Switzerland. [‡]Deceased.

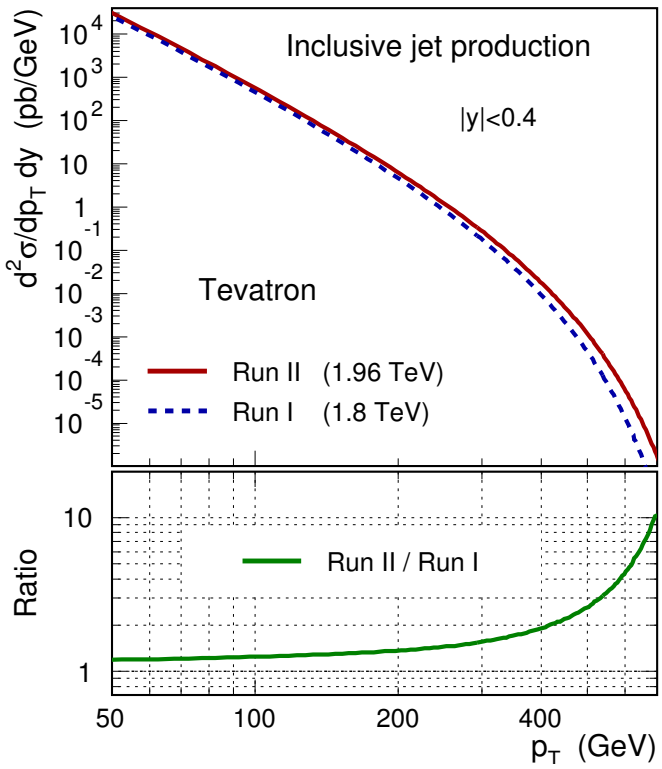

FIG. 1: (color online) Inclusive jet production cross section for central jets ($|y| < 0.4$) for Run I and Run II energies at the Tevatron obtained using NLO QCD as implemented in NLOJET++. The ratio of the two curves is shown in the bottom panel. We note an increase of the Run II cross section with respect to Run I of up to a factor 10 at highest jet p_T.

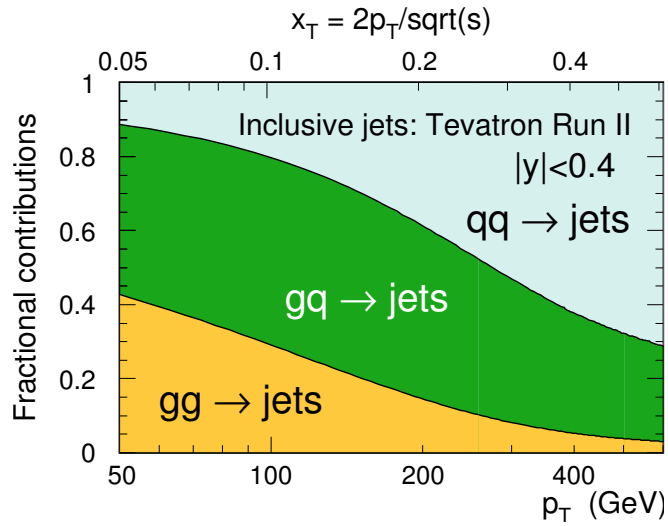

FIG. 2: (color online) Fractional contributions of the qq, qg and gg sub-processes to the inclusive jet cross section for central jets as a function of jet p_T and of the fraction of the beam energy carried by the jet, x_T.

fraction x. In contrast, the quark PDFs are already well constrained by fixed target and electron-proton collider experiments [2].

In this Article, we report measurements by the D0 collaboration of the inclusive jet cross section in $p\bar{p}$ collisions at a center-of-mass energy of $\sqrt{s} = 1.96$ TeV. We give details of the analysis leading to the results published in Ref. [5, 6], with particular attention to the jet energy scale determination. The precision achieved for the jet energy scale in the D0 experiment is unprecedented for any hadron collider experiment to date, and the methods applied to reach this precision will be useful for future hadron collider experiments.

The data sample, collected with the D0 detector during 2004–2005 in Run II of the Fermilab Tevatron, corresponds to an integrated luminosity of $\mathcal{L} = 0.70$ fb^{-1} [7]. The cross section is presented in six bins of jet rapidity (y), extending to $|y| = 2.4$, as a function of jet p_T starting at $p_T = 50$ GeV. The rapidity is related to the polar scattering angle θ with respect to the beam axis by $y = 0.5\ln[(1+\beta\cos\theta)/(1-\beta\cos\theta)]$ with $\beta = |\vec{p}|/E$. The measurement also extends the kinematic reach of earlier measurements of the inclusive jet cross section by the CDF and D0 Collaborations [8–11].

This Article is organized as follows. After a brief description of the D0 detector in Sec. II, we discuss the jet algorithm used in Run II in Sec. III. Section IV describes the theoretical predictions for the inclusive jet cross section before the D0 measurement in Ref. [5]. Section V gives an extensive description of the methods used to measure the jet energy scale and to determine the corresponding uncertainty. This is the leading uncertainty for the measurement of the inclusive jet cross section. Sections VI–XI describe the jet triggers, event and jet selection criteria, determination of the jet p_T resolution and the unfolding method. In Sections XII–XIV, we describe our results and compare them with predictions using recent PDF parameterizations.

II. DETECTOR

In this section, we briefly describe the Run II D0 detector [12] and the main components used in the measurement of the inclusive jet cross section.

A. Calorimeter

The calorimeter and the tracking detectors, used to measure the position of the interaction point, are the most important detector components used to measure the jet p_T. An accurate and stable energy response is required for reliable measurements of the cross section for jet production. The calorimeter consists of the following subdetectors: the uranium/liquid argon calorimeter divided into a central (CC) and two end (EC) sections, the plastic scintillator inter-cryostat detector (ICD), and the massless gap (MG) detectors. Both the CC and ECs

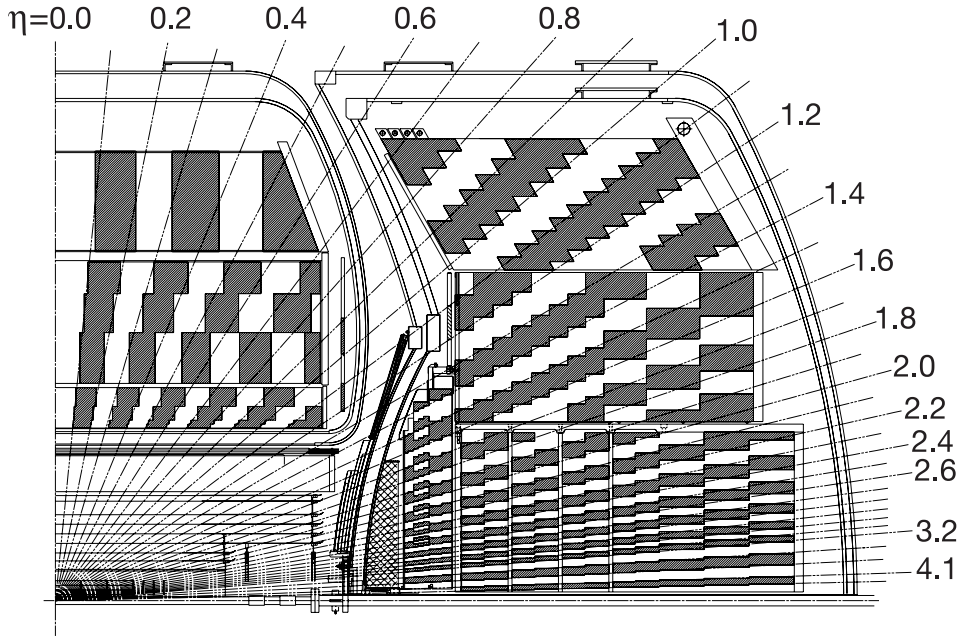

FIG. 3: Side view of a quadrant of the D0 calorimeters (CC, EC and ICR) showing the transverse and longitudinal segmentation [12]. The shading pattern indicates the cells for signal readout. The lines indicate the pseudorapidity intervals defined from the center of the detector. The CC covers the region $|\eta| < 1.2$ and the EC extends the coverage up to $|\eta| \sim 4.2$. The inter-cryostat detector is visible as a thin dark shaded tile between the cryostats, within $1.1 < |\eta| < 1.4$, and the massless gap detectors are inside the cryostats, within $0.8 < |\eta| < 1.2$ (in the CC) and $1.0 < |\eta| < 1.3$ (in the EC).

are segmented longitudinally into electromagnetic (EM), fine hadronic (HAD), and coarse hadronic (CH) sections. A schematic view of the calorimeter showing its projective tower geometry as a function of pseudorapidity $\eta = -\ln\tan(\theta/2)$, where θ is the polar angle from the beamline, is given in Fig. 3. The choice of binning in the inclusive jet cross section measurement closely follows the structure of the calorimeter: $|\eta| < 0.8$ is well-contained within the CC, $1.6 < |\eta| < 2.4$ within the EC, whereas the more challenging inter-cryostat region (ICR) $0.8 < |\eta| < 1.6$ has energy sharing between the four subdetectors.

1. *Central and end calorimeters*

The CC covers detector pseudorapidity $|\eta| < 1.2$, and the two ECs extend the range up to $|\eta| = 4.2$. Both the electromagnetic and fine hadronic calorimeters are sampling calorimeters with an active medium of liquid argon and absorber plates of nearly-pure depleted uranium. Incoming particles traversing the uranium absorber plates initiate showers of secondary particles that ionize the argon in the gaps between the absorber plates. A high-voltage electric field collects the free electrons on resistively-coated copper pads that act as signal boards [12, 13]. The outer part of the calorimeter, the coarse hadronic section, uses copper in the CC and stainless steel in the EC for the absorber plates. The calorimeter is transversely segmented into cells in pseudorapidity and azimuthal angle of 0.1×0.1 (and 0.05×0.05 in the third layer of the EM calorimeter) for $|\eta| < 3.2$ to allow for more precise location of EM shower centroids. At $|\eta| > 3.2$, the cell size grows to 0.2 or more for both η and the azimuthal angle ϕ. These high pseudorapidities are not used for the jet cross section measurements since the jet triggers are limited to $|\eta| < 3.2$. The total depth of the EM calorimeter is about 20 electromagnetic radiation lengths, and the combined thickness of the electromagnetic and hadronic calorimeters is about 7 nuclear interaction lengths [13].

A typical calorimeter cell consists of an absorber plate and a liquid argon gap. The metal plate is grounded, while the resistive plate of the signal board located in the liquid argon gap is kept at a high voltage of ∼2.0 kV. The drift time of the electrons across the typical 2.3 mm gap is 450 ns, longer than the separation between two subsequent Tevatron bunch crossings of 396 ns. To minimize the effect of pile-up from interactions from different bunch crossings, only two-thirds of the charge collected is used in the shaper circuits and then provided to baseline subtraction boards. To remove the baseline, the signal corresponding to a sampling occurring 396 ns earlier (the time between two bunch crossings) is subtracted. Only cells with a signal at least 2.5 times the standard deviation of the electronic noise after baseline subtraction are kept in nominal conditions of data taking. This defines the on-line zero-suppression mode of the calorimeter.

2. Inter-cryostat detector and massless gaps

The regions between the CC and the ECs are instrumented with the inter cryostat detector and massless gaps. The ICD and MG detectors provide energy measurement for the otherwise poorly instrumented regions located at roughly $0.8 < |\eta| < 1.4$, where the depth of the passive material coming from cryostat walls, stiffening rings and cables varies rapidly with rapidity. The ICD relies on photomultipliers to record the signals from plates of scintillating plastic and covers the region $1.1 < |\eta| < 1.4$. The signal from the ICD is stretched in time to match that of the EM calorimeter and augments the EM calorimetry that is absent in the region $1.2 < |\eta| < 1.35$. The ICD is supplemented by the MG detectors that are placed inside the cryostat walls in the CC and the ECs from $0.8 < |\eta| < 1.2$ and $1.0 < |\eta| < 1.3$, respectively. Unlike typical calorimeter cells, the massless gap detectors do not have absorber plates, but they sample the showers that develop in the cryostat walls, calorimeter support structures, and other calorimeter cells.

In addition to the CC, ECs, and ICD, preshower detectors are located in the central and forward regions, but they are not used in this analysis.

B. Tracking detectors

The tracking detectors are not used directly in jet reconstruction since the jet finding algorithms in D0 use only energy deposits in the calorimeter towers. However, the tracking detectors are used to reconstruct the position of the primary vertex of the $p\bar{p}$ interaction, which is necessary to precisely measure the jet rapidity and transverse momentum. The position of the primary vertex is typically distributed as a 20 cm-wide Gaussian distribution along the beamline direction around the nominal interaction point of $(x, y, z) = (0, 0, 0)$ located in the center of the detector. In the detector description and data analysis, we use a right-handed coordinate system in which the z-axis is along the proton direction and the y-axis is upward. The inner tracking system, consisting of the silicon microstrip tracker, provides a 35 μm vertex resolution along the beam line and 15 μm resolution in the $r - \phi$ plane for tracks with a minimum p_T of 10 GeV at $\eta = 0$. The outer tracking system, consisting of the central fiber tracker, uses scintillating fiber technology to complement the silicon tracker. Both detectors are located in the 2 T magnetic field of the superconducting solenoidal magnet to allow measurements of the momentum of charged particles.

C. Muon detector

The muon detector is composed of a combination of proportional drift tubes in the central region ($|\eta| \lesssim 1.0$), and smaller, faster mini drift tubes in the forward region ($1.0 \leq |\eta| \leq 2.0$). Both are separated in three layers (A, B, C). Toroidal magnets are located between the A and B layers of the muon detector in the central and forward regions to allow reconstruction of the muon momentum. The muon system is not used directly in our analysis (we do not correct for muons in jets), but very high energy jets can leak outside the calorimeter and show some hits in the A layer. We do not include these hits in jet reconstruction, but instead correct the jet cross sections for asymmetries introduced in the jet energy resolution (described in Sec IX C).

D. Luminosity detector

The luminosity monitor (LM) is constructed of scintillating tiles on both sides of the interaction point that detect the particles coming from inelastic collisions. The luminosity $\mathcal{L}$ is determined from the average number of observed interactions $\bar{N}_{\rm LM}$ using the formula

$$\mathcal{L} = \frac{f\bar{N}_{\rm LM}}{\sigma_{\rm LM}}, \tag{1}$$

where f is the $p\bar{p}$ bunch crossing frequency, and $\sigma_{\rm LM}$ is the effective cross section for inelastic collisions measured by the LM that takes into account event losses due to inefficiencies and geometric acceptance [7]. In practice, $\bar{N}_{\rm LM}$ is calculated by inverting the expression for the Poisson probability of observing zero LM hits in either of the two arrays

$$P(0) = \mathrm{e}^{-\sigma_{\rm LM}\mathcal{L}/f} \times \left(2\mathrm{e}^{-\sigma_{\rm SS}\mathcal{L}/(2f)} - \mathrm{e}^{-\sigma_{\rm SS}\mathcal{L}/f}\right). \tag{2}$$

The right-most term of Eq. 2 accounts for the possibility of producing double-sided LM hits from a combination of single-sided (SS) LM hits, where $\sigma_{\rm SS}$ is the effective cross section for only one of the arrays to show hits. The uncertainty on the luminosity determination is estimated to be 6.1% [7]. This uncertainty is dominated by the 5.4% uncertainty coming from the determination of $\sigma_{\rm LM}$, roughly half of which is due to acceptance and efficiency of the LM detectors with the remainder due to the uncertainty in the total inelastic cross section at 1.96 TeV described in [7, 14].

III. JET RECONSTRUCTION

Jets are reconstructed using the Run II midpoint cone algorithm [15], which is an iterative cone algorithm that considers energy deposits as four-vectors to construct the jet four-momentum. The same algorithm is used with different inputs in data and Monte Carlo (MC). It is used to build jets from energy deposits in the calorimeter in data or in fully simulated MC events, out of stable particles in simulation, and out of partons produced either

in a parton shower simulation or from a next-to-leading order theoretical calculation.

In data and in MC events processed through a simulation of the response of the D0 detector, the first step is to define the seeds for jet reconstruction. Pseudoprojective towers, as illustrated in Fig. 3, are built by adding the 4-momenta of the calorimeter cells. The 4-momentum associated with the energy deposit in each cell of the calorimeter is computed using the direction defined by the reconstructed $p\bar{p}$ interaction vertex and the center of the cell and assuming $E = |p|$. All non-zero-suppressed cells are used in jet reconstruction. Calorimeter towers are ordered in decreasing transverse momentum and are used as seeds to form preclusters using a simple cone algorithm of radius 0.3 in (η, ϕ) plane, starting with the tower having the highest p_T and then descending the list until no towers remain above a minimum threshold of $p_T > 500$ MeV. All towers added to a precluster are removed from the list, avoiding overlaps between preclusters. Preclusters with $p_T > 1$ GeV are used as seeds for the jet clustering algorithm. The goal of preclustering in data is to reduce the number of seeds and the computing time to reconstruct jets. As verified by MC studies [15], the low value of the p_T threshold on the jet seeds ensures that there are no significant variations in the jet observables for the p_T range considered in this measurement ($p_T > 50$ GeV).

The seeds – preclusters in data and in MC events processed through a simulation of the response of the D0 detector, or stable particles in MC, or partons from NLO calculation – are used as center points for proto-jets. All calorimeter towers, particles or partons within $\Delta R = \sqrt{(\Delta y)^2 + (\Delta\phi)^2} \leq R_{\rm cone}$, where $R_{\rm cone} = 0.7$, are added to the proto-jet. The four-momentum of the proto-jet is the sum of the four-momenta of all included calorimeter towers, particles or partons. The direction of the resulting four-vector is used as the center point for a new cone. When the proto-jet four-momentum does not coincide with the cone axis, the procedure is repeated using the new axis as the center point until a stable solution is found. The maximum number of iterations is 50 and the solution is considered to be stable if the difference in ΔR between two iterations is smaller than 0.001. In the rare cases of bistable solutions the last iteration is retained. Any protojets falling below a threshold, $p_{T,\rm jet} < p_{T,\rm min}$, with $p_{T,\rm min} = 3$ GeV, are discarded.

The presence of a threshold requirement on the cluster seeds introduces a dependency on infrared and collinear radiation. In order to reduce the sensitivity to soft radiation, p_T-weighted mid-points between pairs of proto-jets are used as additional seeds if the distance between pairs, ΔR in the (y, ϕ) plane to the proto-jet, is between 0.7 and 1.4. The list of stable proto-jets obtained from this procedure may contain many overlapping and identical jet candidates. To resolve these ambiguities the proto-jets are sorted in order of decreasing p_T and processed through a split-and-merge procedure to remove overlaps. If two proto-jets have overlapping cones, they are merged if the overlap region contains more than 50% of the transverse momentum of the lower p_T jet. Otherwise, the jets are split with calorimeter cells or particles in the overlap region being assigned to the nearest jet in (y, ϕ). In both cases, the jet four-momenta are recomputed after this reassignment. In case of multiple overlaps, the algorithm always starts with the highest p_T proto-jet to redistribute the shared towers. As mentioned above, the jet four-momentum is computed as the sum of the four-momenta of the (massless) calorimeter energy deposits included in the jet, and consequently the calorimeter jets are massive by construction if the jet cone contains cells with different locations in the (η, ϕ) plane. The variables used to characterize the jets are the jet p_T and y. The split-and-merge procedure may modify the cone axis and jet four-momentum for the final jets, and include towers outside the initial 0.7 cone.

IV. THEORETICAL PREDICTIONS

In this section, we describe how we compute the predictions of the inclusive jet cross sections that are later compared to our measurements.

1. *Jet cross section at NLO*

We use the program FastNLO [16], which is based on the matrix elements implemented in NLOJET++, to calculate the inclusive cross sections to next-to-leading order precision and to evaluate the effects of the choice of proton PDFs, such as CTEQ6 or MRST2004 [17, 18], in a computationally efficient manner. Perturbative QCD (PQCD) requires the specification of the renormalization scale μ_R and the factorization scale μ_F. Typical choices set both $\mu_R = \mu_F$ to the p_T of each of the individual jets, with half and twice this scale used to estimate the theoretical scale uncertainty. The uncertainty on the NLO prediction of the inclusive jet cross section due to the choice of renormalization and factorization scales is given in Fig. 4 and is about 10–20%.

2. *Parton distribution functions*

A discussion of the different PDFs and methods to reduce their uncertainties using various measurements at the Tevatron and the LHC can be found in reference [2]. In this paper, we briefly describe the PDFs used in the comparison between the measurements and the theoretical predictions.

One of the PDF sets used in this analysis is provided by the CTEQ Collaboration. This most recent global fit from the CTEQ Collaboration performed prior to the measurement described in this paper, called CTEQ6.5M [17], utilizes D0 and CDF Run I measurements, as well as the most recent deep inelastic scatter-

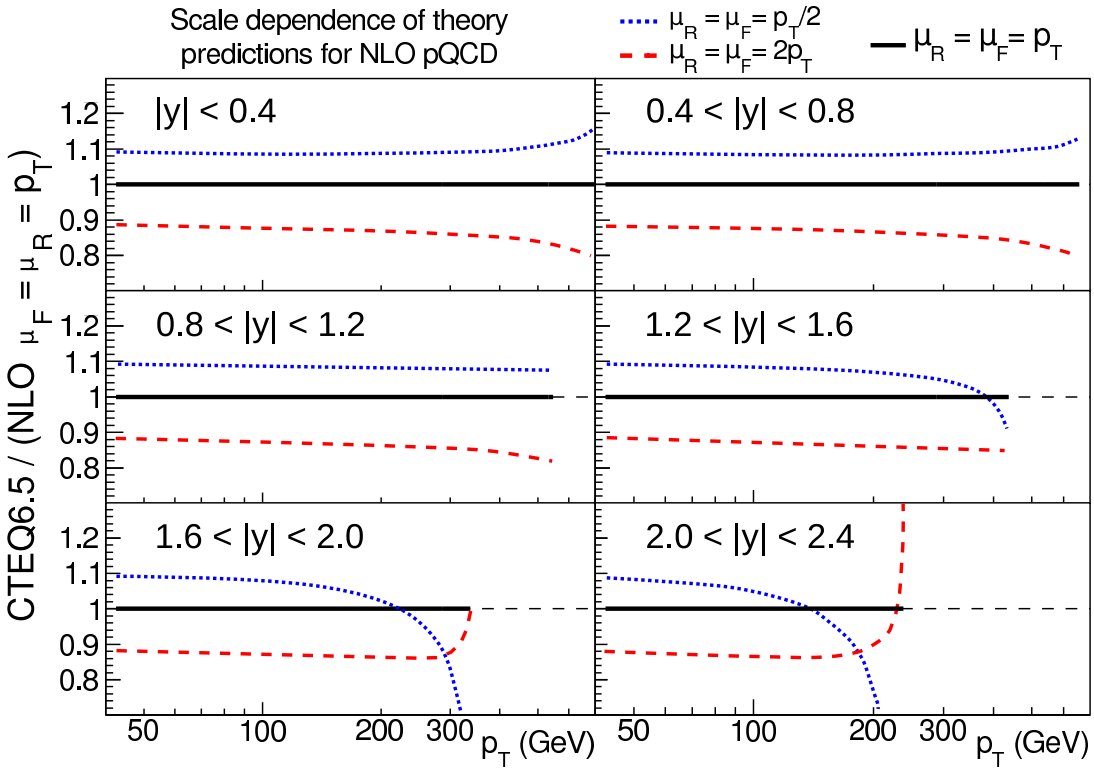

FIG. 4: (color online) Uncertainty on the inclusive jet cross section due to the choice of the renormalization and factorization scales μ_R and μ_F in the NLO QCD calculation using NLOJET++.

ing (DIS) data from the HERA collider at DESY and existing fixed target DIS and Drell-Yan data. The central prediction of the CTEQ6.5M PDF is supplemented with the provision of 20 eigenvector basis PDF sets to estimate the PDF uncertainty, representing independent variations of the PDFs within the 90% C.L. of the data sets used in the fit.

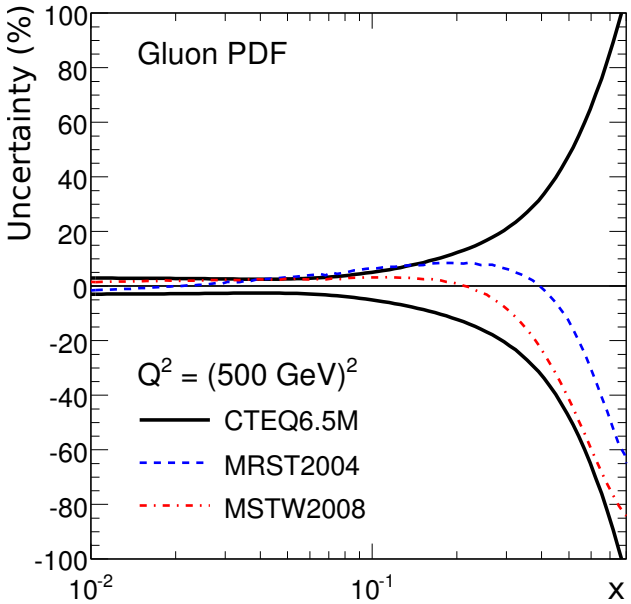

FIG. 5: (color online) Uncertainty of the CTEQ6.5M gluon PDF (solid lines) in percent compared to the differences between CTEQ6.5M and MRST2004 (dashed line), MSTW2008 (dash-dotted line) central values.

Another widely used PDF parameterization is provided by the MRST Collaboration [18]. Our measurements are compared to the MRST2004 parameterization, which does not include our results. A third PDF parameterization is MSTW2008 [19] which uses our results. The differences with respect to CTEQ6.5M are mainly in the description of the gluons at high-x and are within the CTEQ6.5M uncertainty band, as shown in Fig. 5. We also note that the uncertainty on the gluon density calculated by the CTEQ6.5M parameterization is larger than 40% for $x \geq 0.5$ and squared four-momentum transfer $Q^2 = 500^2$ GeV. Comparisons between our data and NLO calculations using these and other PDF parameterizations are given in Sec. XII.

V. JET ENERGY SCALE MEASUREMENT

In this section we describe the method used to obtain the jet energy scale (JES) applied in the measurement of the inclusive jet cross section as a function of jet p_T. To compare the theoretical predictions to data, both need to be corrected to a common reference-level, chosen here to

be the "particle-level jets." We correct the calorimeter jet energies to the particle level, and apply non-perturbative corrections (hadronization and underlying event) to theoretical NLO cross sections to move from the parton to the particle level. Particle jets [20] are clustered from stable particles after fragmentation, including particles from the true underlying event, but excluding undetected energy from muons and neutrinos. The JES procedure provides a correction factor that translates on average the energy of jets measured in the calorimeter to the energy of the corresponding particle jets. The jet energy scale is determined from data acquired during the same running period as used in the measurement of the inclusive jet cross section.

The main effects that need to be considered when correcting jet energies from the calorimeter measurement $E_{\rm meas}$ to the particle level $E_{\rm particle}$ are the offset energy (O), calorimeter response (R), and detector showering (S). These corrections can be expressed as a simple formula

$$E_{\rm particle} = \frac{E_{\rm meas} - O}{R \cdot S}. \tag{3}$$

The offset energy O originates from electronics noise, calorimeter noise from uranium decays, residual energy from previous bunch crossings ("pile-up"), and energy from multiple $p\bar{p}$ collisions during a bunch crossing. The underlying event energy corresponding to multiple parton interactions in a single $p\bar{p}$ collision is not considered as part of the offset energy since it is included in the jet energy at the particle level. This also avoids correcting the data with model dependent offset corrections. The calorimeter response R is the average fraction of the energy measured in the calorimeter for the particles inside the jet cone. The detector showering is the net flow of energy in and out of the jet cone due to detector effects, such as the magnetic field, scattering from passive material, and shower development in the calorimeter. The correction S is defined as the ratio of the response-corrected calorimeter jet energy, in the absence of offset, and the particle jet energy. The correction does not include the effects of real QCD emissions, which arise from partons that shower outside the jet cone. We discuss each correction in turn below.

A. Determination of the offset energy

The offset energy consists of the energy in the jet that is not related to the primary $p\bar{p}$ collision (hard scatter and underlying event). The offset energy is divided into two distinct categories, noise and pile-up (NP), and multiple $p\bar{p}$ interactions (MI). The noise component corresponds to the contributions of calorimeter and electronics noise, as well as the decay of the uranium nuclei in the calorimeter. The pile-up energy corresponds to the energy left in the calorimeter from previous or next collisions because of the long integration time of the calorimeter electronics. The typical value of the NP offset in a cone, $R = 0.7$, is 0.2 GeV in the CC and ECs and 0.5 GeV in the ICR for the instantaneous luminosities considered in this analysis.

The MI offset is the energy deposited by additional collisions during the bunch crossing. The value of the MI offset increases linearly with the number of additional interactions, which is characterized by the number of reconstructed $p\bar{p}$ interaction vertices in a given event. A typical value of MI is of the order of 0.5 GeV in the CC per additional interaction.

The offset energies are measured directly from data using "zero bias" and "minimum bias" data collected at a constant rate of about 0.5 Hz during data taking. The only requirement for zero bias events is coincident timing with the beam crossing; minimum bias events additionally require energy depositions above thresholds in coincidence in the two luminosity monitors, indicating that an inelastic collision took place. The offset is estimated from the average energy density in all calorimeter towers within detector rings of fixed pseudorapidity. The offset energy for a given jet cone is then calculated by summing the average offset in towers within the cone radius around the jet center. The NP offset energy is measured using zero bias data with a veto on the luminosity monitor (no interaction occurred), and the MI energy for a given number N of interactions is the difference in the energy in minimum bias events with $(N+1)$ vertices and with a single vertex.

The offset energy for different numbers of $p\bar{p}$ interactions (measured by the number of reconstructed vertices) is displayed in Fig. 6 and is found to depend linearly on the number of interactions within a 5% uncertainty. The average vertex multiplicity in the sample used to measure the inclusive jet p_T cross section is $\sim$1.5 – 2.0, hence the average offset correction to jet p_T is $\sim$0.5 GeV in the CC and EC and $\sim$0.7 GeV in the ICR. The uncertainties on the offset corrections are of the order of 1% of the overall energy correction at low jet p_T and are negligible for jet p_T above $\sim$100 GeV. They are significantly smaller than the total jet energy scale uncertainties.

B. Determination of the jet energy response

The jet energy response, R, can be factorized into two parts $R = R_{\rm cc}(E) \cdot F_\eta(\eta, E)$. The $R_{\rm cc}$ term uses the p_T balance between the γ and the jet in γ+jet events with a high (photon) purity in the CC region to determine an absolute response correction, while the second term F_η normalizes the response of the calorimeter as a function of jet pseudorapidity.

1. *Jet response in the CC*

The missing transverse energy ($\not\!\!E_T$) projection fraction (MPF) method [21] is applied in $\gamma +$ jet events to mea-

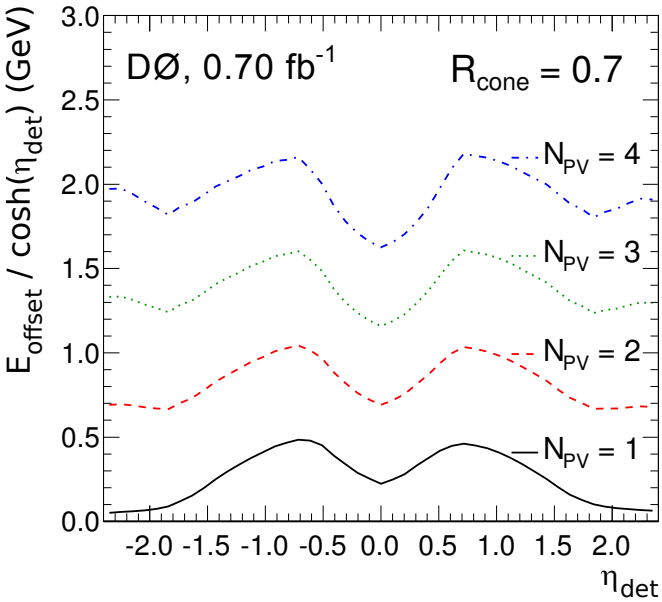

FIG. 6: (color online) Offset corrections as a function of the jet pseudorapidity in the detector (without taking into account the vertex position) for different numbers of reconstructed primary vertices $N_{\rm PV}$. The special case $N_{\rm PV} = 1$ includes only the noise contribution to the offset.

sure the response for jet energies in the CC region. Use of the MPF reduces the sensitivity of the measurement to showering and additional unreconstructed jets. We project the vector sum of all calorimeter tower energies transverse to the beam (including those of the photon), which equals the opposite of the $\not\!\!E_T$ in the event, onto the photon transverse momentum vector $\vec{p}_{T,\gamma}$. At the particle level, the photon is balanced against the hadronic recoil, $\vec{p}_{T,\gamma} + \vec{p}_{T,\rm had} = 0$, where $\vec{p}_{T,\gamma}$ and $\vec{p}_{T,\rm had}$ are the transverse momentum of the photon and the hadronic recoil system, respectively. The measured jet p_T will be affected by the energy response of the calorimeter causing an imbalance in the jet and photon transverse momenta, resulting in a non-zero $\not\!\!E_T$,

$$R_{\rm em} \cdot \vec{p}_{T,\gamma} + R_{\rm had} \cdot \vec{p}_{T,\rm had} = -\vec{\not\!\!E}_T, \tag{4}$$

where $R_{\rm em}$ and $R_{\rm had}$ are the electromagnetic and hadronic calorimeter responses, respectively.

The MPF method necessitates a precise energy calibration for electrons and photons. The electron energy scale is determined from data using $Z \to e^+e^-$ decays [22]. MC simulations tuned to reproduce the response for electrons in data are used to derive the response difference between photons and electrons. The leading uncertainty in this simulation is caused by limited knowledge of the number of radiation lengths of material in front of the calorimeter.

Using the corrected photon energy scale ($R_{\rm em} = 1$), $R_{\rm had}$ is determined after projecting all terms in Eq. 4 on the photon p_T unit vector $\hat{n}_\gamma$. In the MPF method, the jet response $R_{\rm had}$ is thus directly defined through the $\not\!\!E_T$

$$R_{\rm had} = 1 + \frac{\vec{\not\!\!E}_T \cdot \hat{n}_\gamma}{|\vec{p}_{T,\gamma}|}, \tag{5}$$

where we use $|\vec{p}_{T,\gamma}| = -\hat{n}_\gamma \cdot \vec{p}_{T,\rm had}$. When the jet is required to be back-to-back with the photon (difference in azimuthal angle larger than 2.9 radians) and no additional jets are allowed in events with a single $p\bar{p}$ interaction, the hadronic recoil response $R_{\rm had}$ can be identified with the jet response $R_{\rm jet}$. The impact of the proton remnants is small on average. The jet energy response depends on the particle jet energy and the results are usually binned in jet p_T. However, the measured jet energy has poor resolution and can lead to a large bias in the measurement of the response. To avoid this resolution bias, the jet energy response is measured as a function of the estimator

$$E' = p_{T,\gamma} \cdot \cosh \eta_{\rm jet}. \tag{6}$$

E' is strongly correlated to the particle level jet energy and has a better resolution than the measured jet energy. We parameterize all corrections as a function of E' and map back to the measured jet energy $E_{\rm meas}$ on a jet-by-jet basis by inverting the equation

$$E_{\rm meas} - O = R_{\rm had}(E') S_{\rm phys}(E') E', \tag{7}$$

where O is the offset contribution, $R_{\rm had}(E')$ contains all jet energy corrections back to particle level, and $S_{\rm phys}(E') = E^{\rm ptcl}_{\rm jet}/E'$ contains the additional corrections for particle showering, causing energy to flow out of or into the jet cone. The latter component accounts for energy loss from out-of-cone radiation (physics showering), leading to a correction of 0.90–1.00 at jet p_T >50 GeV and $|y|$ <3.0. The equation is iteratively solved using Newton's method. The resulting estimate of the jet energy is observed to agree with the true E' to better than 2% at jet $p_T > 50$ GeV, resulting in less than 0.2% uncertainty on the jet response $R_{\rm had}$.

Another issue in using the MPF is related to photon identification. To have a clean γ+jet sample in data, only CC photons are used with tight selection criteria. However, in some jets a large fraction of their transverse momentum is carried by photons from π^0, η, or K^0_s decays, which form a sample of "electromagnetic" jets ("EM-jets"). If these photons are sufficiently close together, and there is little activity around the photons, the jet can mimic an isolated single photon typical for γ+jet events. Because the cross section for γ+jet events is $\sim$3 – 4 orders of magnitude lower than that of dijet events, these EM-jets contribute a significant background for true γ+jet events. An artificial neural network (ANN) is trained to discriminate between photon and EM-jets [23] using input variables based on the shape of the calorimeter shower and measurements of charged particle tracks in the vicinity of the photon candidate. The distribution of the photon ANN output for the simulated photon signal and for the EM-jet background samples are fitted to

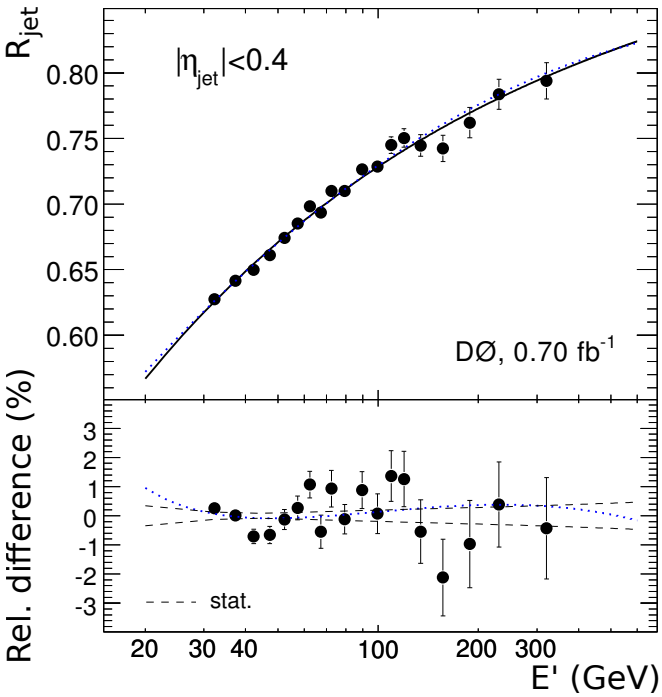

FIG. 7: (color online) Extrapolation of the jet energy response in the CC at high E' using the rescaled MC (see the main text) and a fit to the MC points. The dotted line shows a simple quadratic logarithmic fit to data for comparison with the tuned MC results displayed by the solid line. We also display in the bottom panel the relative difference between both curves and the statistical uncertainty on the fit to the rescaled MC in dashed lines.

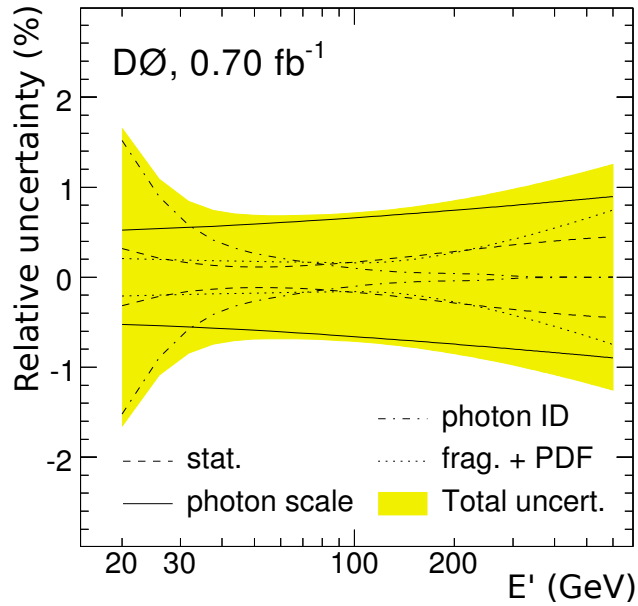

FIG. 8: (color online) Different sources of uncertainty on the jet p_T response in the CC: photon energy scale, photon identification, fragmentation, and PDF.

the data for each E' and η bin using a maximum likelihood optimization to obtain the fractions of signal events in the data. To reduce the uncertainty in the jet energy scale due to contamination from background in the γ+jet events, the difference in the response determined from real γ+jet and dijet events, where one of the jets is misidentified as a prompt photon, is estimated using MC and applied as a correction based on the estimated purity of the selected photons in data. The jet energy response after all corrections as a function of E' in the CC is given in Fig. 7. The main uncertainty is due to the uncertainty on the photon energy scale, which is on the order of 0.5% at $E' \approx 20$ GeV and 0.8% at $E' \approx 500$ GeV. The choice of fragmentation model used in Pythia [24] was an additional source of systematic uncertainty on the photon purity [25].

The statistics of the γ+jets sample limits the direct response measurements in the CC to $E' < 350$ GeV. The measured energy response in this region must be extrapolated to the highest jet energies at ≈ 600 GeV. To avoid a statistical uncertainty of more than 2% at high-p_T in the CC, MC models are used to constrain the high-p_T response. For this purpose, the measurement of the response in γ+jet events in the MC is rescaled to the measurement in data by modifying the response of the calorimeter for single pions in MC. Figure 7 shows the measured response for jets in data compared to the rescaled MC prediction and to a quadratic fit in $\log E'$. The uncertainty in the fragmentation model for the high E' extrapolation is estimated using the differences between the Pythia and Herwig [26] generators after turning off the underlying event modeling. This leads to a systematic uncertainty of about 0.8% at $E' = 600$ GeV. The systematic uncertainties related to PDFs (especially due to the uncertainty on the gluon fraction in the proton) are about 0.2%.

The total uncertainty on the jet p_T response as a function of E' is given in Fig. 8. The dominant uncertainty comes from the photon energy scale. The uncertainty due to photon identification is related to the uncertainty on the sample purity and contributes mainly at E' energies below 50 GeV.

2. *Pseudorapidity dependent corrections*

The purpose of the η-dependent corrections is to equalize the jet response everywhere as a function of pseudorapidity in the calorimeter after the jets are corrected for offset effects. The D0 calorimeter is inter-calibrated at the cell level as a function of the azimuthal angle ϕ by equalizing the response of the calorimeter in dedicated ϕ-symmetric data samples. This yields a jet response that is independent of ϕ, so only the η dependence of the response needs to be corrected. The η dependence of the response is mostly due to the changing calorimeter detector elements, especially in the ICR, different amounts of passive material and the varying angle of incidence

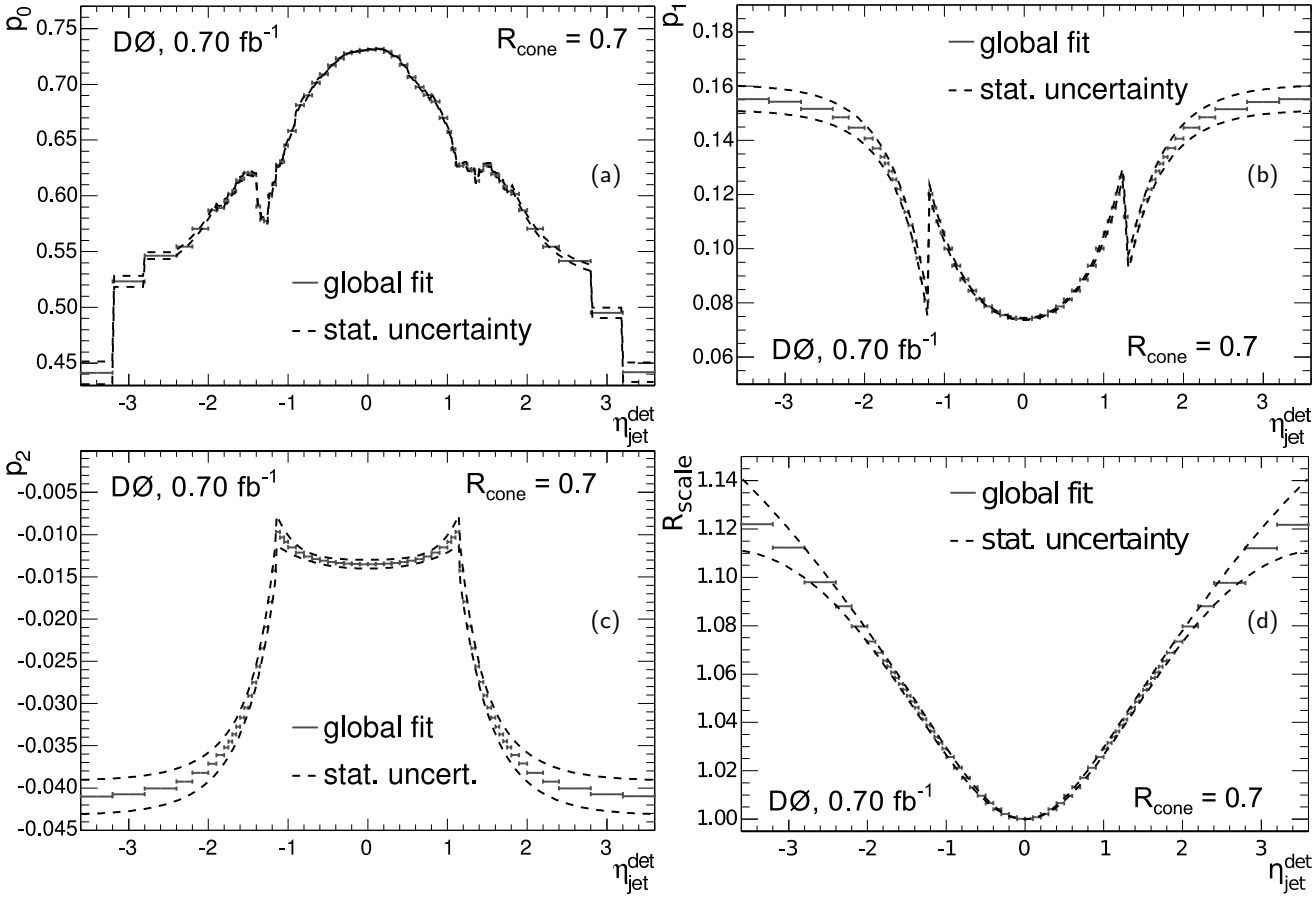

FIG. 9: The (a-c) parameters of the η-dependent correction and (d) the η-dependent scaling factor applied to the dijet samples. The sharp features are due to changes in the detector structure, moving from the central to forward calorimeters.

with jet η. The η-dependent corrections $F_\eta(E,\eta)$ normalize the response at forward pseudorapidities to that measured in the CC (R_{CC}). This leads to the definition

$$F_\eta(E,\eta) \equiv R(E,\eta)/R_{\rm CC}(E), \tag{8}$$

where $R(E,\eta)$ is the response of the detector for a jet of energy E, located at detector pseudorapidity η. We use both dijet and γ+jet samples to determine F_η. The dijet sample provides high statistics and high reach in jet energy for the forward region. One of the jets is required to be central and the response measurement is binned in terms of the p_T of the central jet (using the dijet E', defined as in Eq. 6 where the photon is replaced by the central jet) after correcting for the offset and calorimeter response. This binning leads to a resolution bias, which is later corrected.

The η-dependence of the response, F_η, is fitted using a quadratic-logarithmic function of E'

$$F_\eta(E',\eta) = \frac{p_0(\eta) + p_1(\eta)\ln(E') + p_2(\eta)\ln^2(E')}{R_{\rm CC}(E')}, \tag{9}$$

where the p_i are fitted as a function of detector η. The F_η and p_i's are given in Fig. 9(a-c). As an example of the data used in this fit, we give in Fig. 10 the η-dependent corrections for two bins in η for the dijet and γ+jet samples. Although the correction factors depend on the sample (γ+jet, dijets), we can remove this dependency by scaling the dijet correction in the overlap region between the CC and the EC by an energy-independent factor $R_{\rm scale}$:

$$R_{\rm scale}(\eta) = 1 + q_1 \ln[\cosh(\eta)] + q_2 \ln^2[\cosh(\eta)], \tag{10}$$

where q_1 and q_2 are two parameters fitted to data and the result is given in Fig. 9(d). This functional form is motivated by phenomenological studies of the difference in the jet responses measured in γ+jet and dijet samples, as discussed in the next section.

The jet p_T resolution is worse than the γ p_T resolution. Due to the steeply falling inclusive jet cross section, more jets migrate into a given p_T bin from lower p_T than from higher p_T, giving rise to a p_T bias compared to the particle level. The effect of this resolution bias is taken

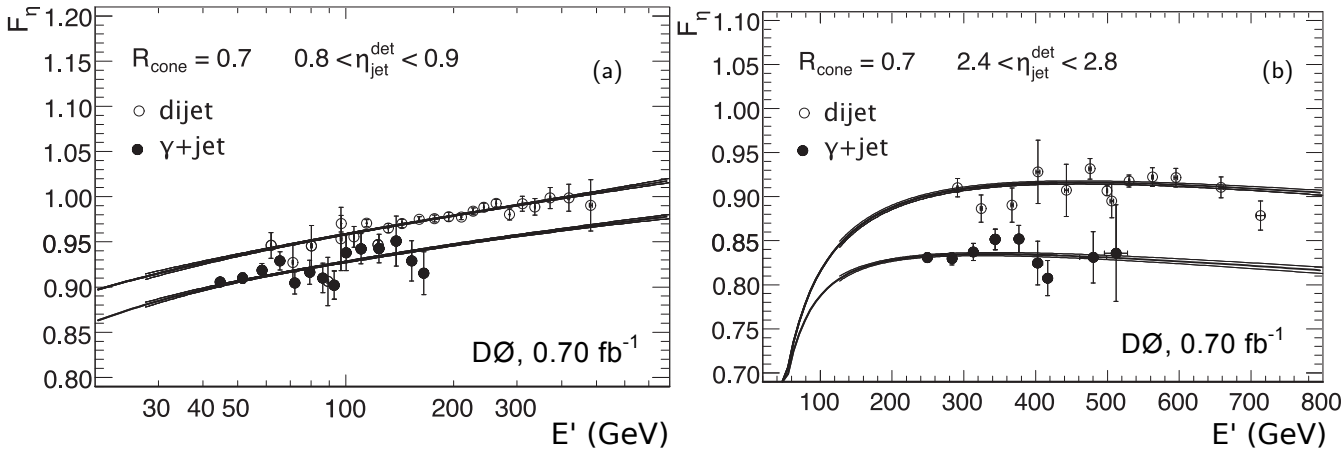

FIG. 10: Fits of F_η in γ+jet and dijet data for two different regions in η as a function of E'. The central fit values and the uncertainty band are displayed on the figure.

into account in the final measurement of the jet p_T response versus η using the CC jet p_T resolutions obtained from dijet events as described in Sec. IX. In particular, the jet transverse momenta in dijet events in the CC are *a priori* perfectly balanced on average by definition $[F_\eta(E', \eta = 0) = R_{\rm scale}(\eta = 0) = 1]$, which provides a strong constraint for the bias correction.

With the application of the dijet-specific scale factor and resolution bias corrections we obtain systematic uncertainties in the η-dependent corrections that are less than 1% for $|\eta| < 2.8$ as illustrated in Fig. 11. The leading systematic uncertainty is from the average residuals of the fits for F_η and is estimated to be 0.5% for $0.4 < |y| < 2.4$ and constant versus energy. This residual accounts for the scatter of the data points around the central fit and covers possible variation in the shape of the fit function. The uncertainty due to the resolution bias correction is of the order of 0.5% at $|\eta| = 2.0$ and reduces to zero at $\eta = 0$.

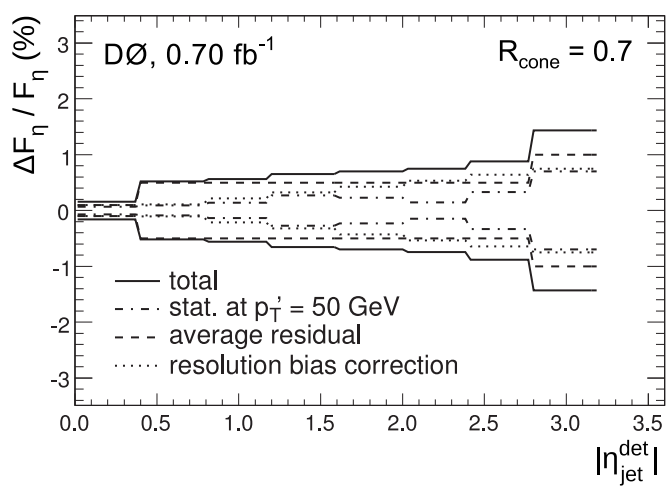

FIG. 11: Relative uncertainties on the η-dependent corrections as a function of jet detector rapidity.

3. *Dijet specific response*

The methods presented so far allow for a precise measurement of the MPF response in the CC for the γ+jet sample. However, the response for dijet and γ+jet events is different. Figure 12 displays response for the quark and gluon initiated jets measured in MC simulations after rescaling the single pion response to data. The gluon-initiated jets have a lower response than quark-initiated jets because they have on average higher particle multiplicity with softer particles. The soft particles lead to a lower jet response due to the falling single pion response at low energy. Figure 13 displays the fraction of gluon-initiated jets in MC for γ+jet and dijet events. The γ+jet jet energy scale cannot be used directly for the measurement of the inclusive jet cross section, because this sample is strongly dominated by dijets. This effect also explains the differences we observe in Fig. 10 for the η-dependent corrections in γ+jet and dijet samples. The difference observed in F_η versus E' at fixed η is due to the different amounts of quark and gluon jets in the samples. The gluon versus quark fractions depend primarily on energy (not p_T or η) which leads to a correction factor dependent on $\cosh(\eta)$. Once this difference is taken into account, it is possible to combine both samples to fit F_η.

To calculate the relative difference in response between γ+jet and dijet samples in the CC, we first scale the single pion response in MC to reproduce the measured jet response in the γ+jet data. The measurement from data of the absolute jet response in γ+jet events in the CC is then scaled to its dijet equivalent. The dijet η-dependent corrections are obtained from a global fit to γ+jet and dijet data, which accounts for the sample-dependent response.

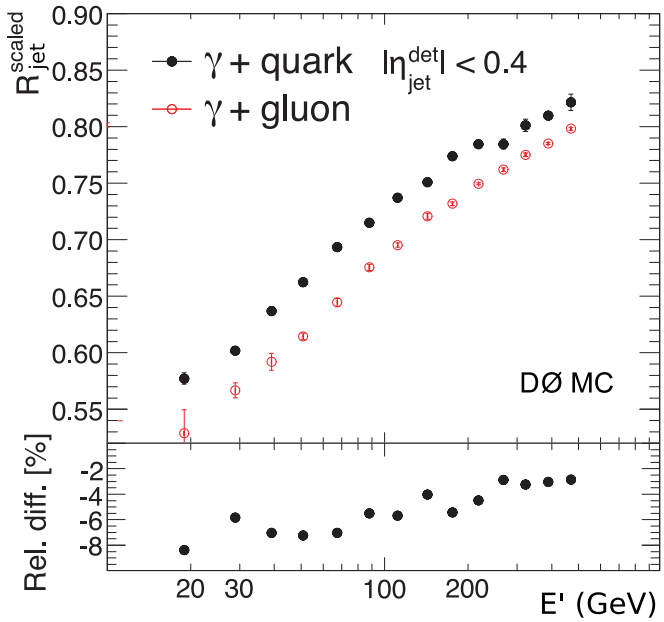

FIG. 12: (color online) Quark- and gluon-initiated jet responses and their relative differences for CC jets as a function of E'.

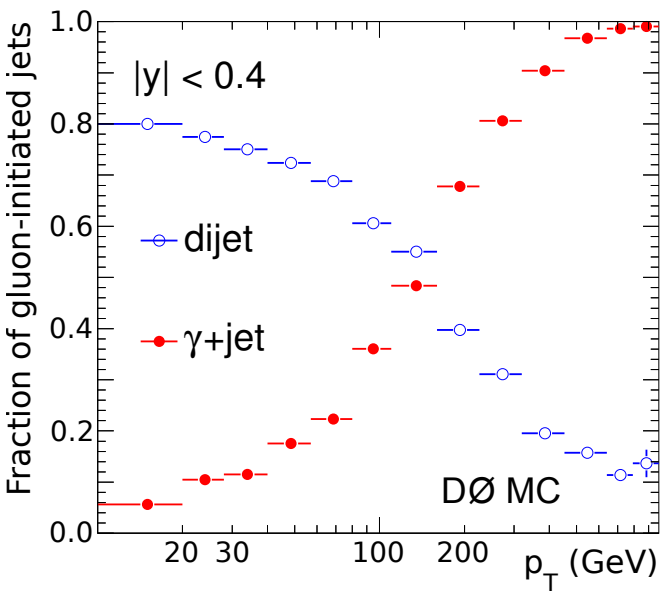

FIG. 13: (color online) Fraction of gluon initiated jets in γ+jet and dijet events in the CC.

The differences between the dijet response used in this analysis and the γ+jet response used in most other analyses are contained in the η-dependent scale factor F_η and the ratio of tuned MC responses $R_{\mathrm{dijet}/\gamma+\mathrm{jet}}$ at $\eta = 0$

$$R_{\mathrm{dijet}}(E',\eta) = R_{\mathrm{dijet}/\gamma+\mathrm{jet}}(E') \cdot F_\eta(\eta) \cdot R_{\gamma+\mathrm{jet}}(E',\eta). \quad (11)$$

The ratio between the dijet and γ+jet responses $R_{\mathrm{dijet}/\gamma+\mathrm{jet}}$ is in practice given by the information presented in Figs. 12 and 13 and can be expressed using the responses for the gluon- and quark-jets[1] (R_{gluon} and R_{quark}) and the fractions of gluon-jets in the dijet and γ+jet samples ($f_{\mathrm{gluon}}^{\mathrm{dijet}}$ and $f_{\mathrm{gluon}}^{\gamma+\mathrm{jet}}$)

$$R_{\mathrm{dijet}/\gamma+\mathrm{jet}} = \frac{(R_{\mathrm{gluon}} f_{\mathrm{gluon}}^{\mathrm{dijet}} + R_{\mathrm{quark}}(1 - f_{\mathrm{gluon}}^{\mathrm{dijet}}))}{(R_{\mathrm{gluon}} f_{\mathrm{gluon}}^{\gamma+\mathrm{jet}} + R_{\mathrm{quark}}(1 - f_{\mathrm{gluon}}^{\gamma+\mathrm{jet}}))}. \quad (12)$$

C. Showering correction

Jets are extended objects and deposit their energy over a wide area in the calorimeter. When the cone algorithm is used, some of this energy is deposited outside the jet cone due to interactions with the magnetic field and passive material. This is called detector showering and needs to be taken into account in the jet energy scale determination. In addition, part of the energy of the incident parton is lost outside the jet cone because of hadronization and the finite size of the jet cone. This is called physics showering and is taken into account in the energy scale correction to the particle level.

The determination of the showering corrections requires a good understanding of the transverse jet energy profile. In a dedicated study, the cell-level information from MC is kept to generate energy density profiles as a function of the distance $\Delta R = \sqrt{(y_{particle} - y_{jet})^2 + (\phi_{particle} - \phi_{jet})^2}$ between the particle and the jet axis for particles originating from inside the particle jet, from outside the jet, and from offset due in particular to pile up or additional interactions in one bunch crossing. The sum of these profiles is fitted to the measured energy profile in data to account for possible response differences between data and MC. The energy profiles are created by summing the energy in the cells at a given radius from the cone axis. The profiles are calculated for back-to-back γ+jet events and show the jet core at ΔR around 0 and the photon contribution at $\Delta R \approx \pi$. The energy density in the range $R_{\mathrm{cone}} < \Delta R < \pi$ is primarily offset energy. Figure 14 shows an example of the showering profiles in MC without any zero bias event overlay (i.e. with only the underlying event and no offset). It gives the average energy in a given rapidity and transverse energy bin coming from inside and outside the jet as a function of the distance ΔR in rapidity and azimuthal angle from the center of the jet. The MC describes the data when both the energies inside and outside the jet are considered.

The estimate of the showering correction $\hat{S}$ for γ+jet events in MC and data is obtained by comparing the energy deposited by all particles inside the calorimeter jet cone $\sum_{\Delta R=0}^{R_{\mathrm{cone}}} E_{\mathrm{in}} + \sum_{\Delta R=0}^{R_{\mathrm{cone}}} E_{\mathrm{out}}$ originating from inside

[1] We note that nearly all the quark-initiated jets come from light quarks.

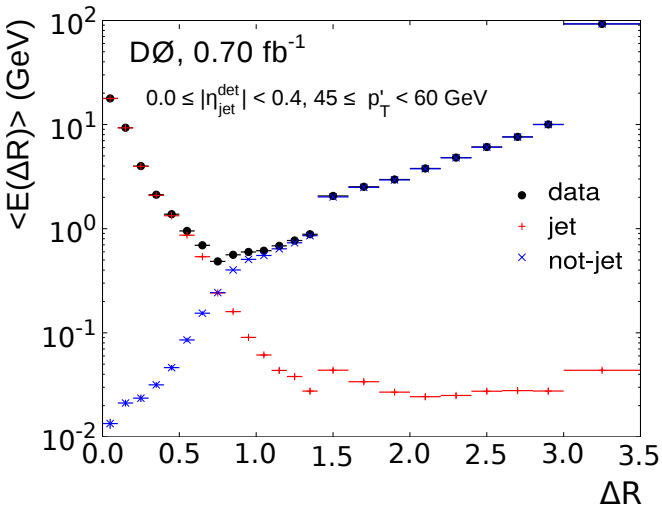

FIG. 14: (color online) Jet energy profiles as a function of distance from the jet axis ΔR for MC and data used to compute showering corrections. The data are corrected for offset energy from noise and additional $p\bar{p}$ collisions and are compared to MC jets without offset (jet) and contributions from the underlying event (not-jet). We note the good agreement between data and the sum of energy contributions from inside and outside the jet in MC.

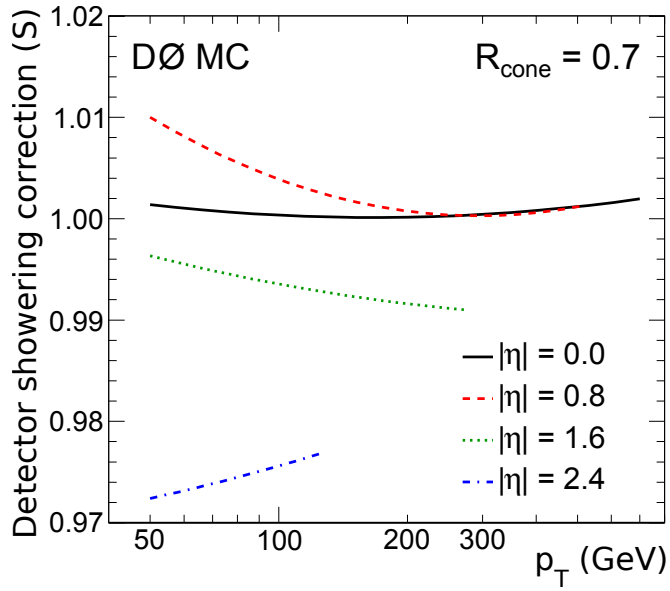

FIG. 15: (color online) Jet showering corrections shown as a function of jet p_T for different regions of jet pseudorapidity.

or outside the particle jet to that from the original particle jet $\sum_{\Delta R=0}^{\infty} E_{\rm in}$ using the fit-weighted templates

$$\hat{S} = \frac{\sum_{\Delta R=0}^{R_{\rm cone}} E_{\rm in} + \sum_{\Delta R=0}^{R_{\rm cone}} E_{\rm out}}{\sum_{\Delta R=0}^{\infty} E_{\rm in}}, \tag{13}$$

where $E_{\rm in}$ and $E_{\rm out}$ are the energies coming from inside and outside the jet. To take into account any potential bias in the method, the final value of the showering correction in data is computed as

$$S_{\rm data} = \hat{S}_{\rm data} \cdot \frac{S^{\rm true}_{\rm MC}}{\hat{S}_{\rm MC}}, \tag{14}$$

where the true showering $S^{\rm true}_{\rm MC}$ is directly available in MC. This bias correction amounts to less than 0.3%.

While the showering templates are measured in energy, the applicable quantity for the cross section measurement is jet p_T. When mapping the showering templates to p_T the deposits in rapidity are weighted by $\cosh(y_0)/\cosh(y_i)$, where y_0 is the cone axis and y_i is the rapidity of the energy deposit. As a result of this weighting, the effects of showering in p_T are generally suppressed relative to energy showering. This can also tilt the jet toward $y = 0$ and cause a net increase in the jet p_T, leading to $S_{\rm data} > 1$. The differences between energy and p_T showering can be up to (1–2)% over the kinematic region of the cross section measurements.

The last step of the showering correction is to make the transition from γ+jet to dijet events. This remaining correction is computed directly using the differences in showering in γ+jet and dijet MC. The final jet p_T showering corrections are given in Fig. 15.

The uncertainties on the showering correction are less than 1% of the overall correction factor at $p_T > 50$ GeV. The main sources of uncertainty come from the difference between data and MC in the single pion response at low p_T, the quality of the fits of MC templates to data, and the description of the underlying event determined by varying PYTHIA tunes for Tevatron data at higher p_T.

D. Potential biases in the method

1. *Topology bias of the MPF method*

The MPF method balances a photon or a central jet against the full remaining hadronic recoil, but the measured MPF response is interpreted as the response of the probe jet. The precision of this interpretation may be biased because the hadronic recoil includes particles not related to the probe jet, for example, particles coming from soft gluon radiation. These additional particles are generally softer than those in the core of the jet and are expected to lower the response of the recoil with respect to that of the jet core.

In the case of the energy measurement, an additional bias is caused by the systematic mismeasurement of the jet rapidity, because the MPF method is inherently based on balancing p_T. As we will see in the following, the rapidity bias is particularly large in the ICR, where the absolute rapidity is systematically underestimated and causes a corresponding increase in the MPF response: the same calorimeter energy now corresponds to higher p_T. Since the bias versus energy has a non-trivial rapidity dependence and the cross section measurement is performed as a function of p_T, we derive and apply topol-

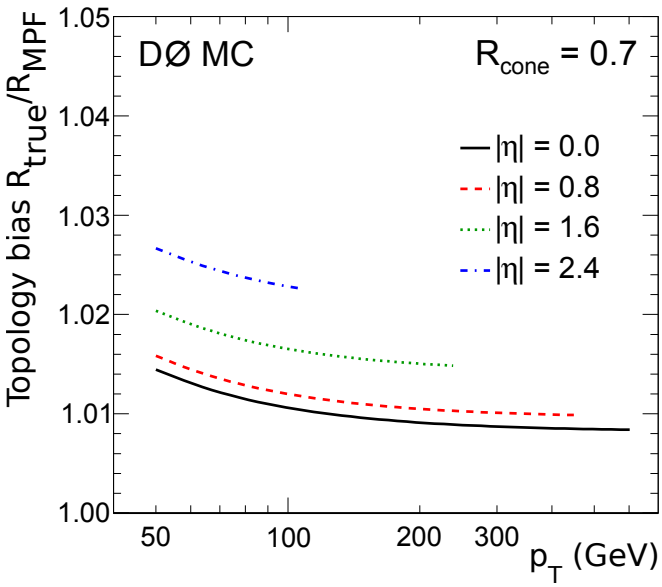

FIG. 16: (color online) Topology bias in the MPF method for jet p_T response.

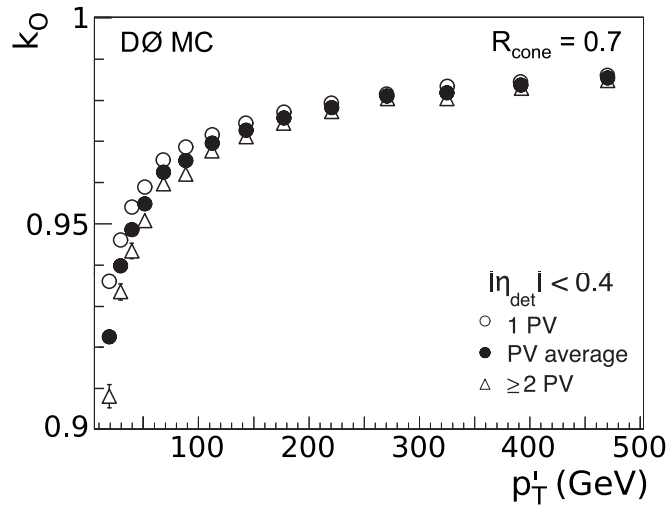

FIG. 17: Bias in the measurement of jet energy, k_O, due to zero suppression effects on the offset correction, shown as a function of p'_T for central jets and different number of reconstructed vertices.

ogy bias corrections as a function of jet p_T.

The bias of the MPF response is determined in tuned MC by comparing the MPF response to the true response defined at the particle level. The result for the p_T response is shown in Fig. 16. This bias is about 1–2.5% for the different rapidity regions with little p_T dependence ($< 0.5\%$) for $p_T > 50$ GeV. The MPF response bias is quite small since the method is based on the p_T balance and the cone size of $R = 0.7$ is large enough to contain most of the hadronic recoil in the absence of additional soft non-reconstructed jets. The bias is significantly larger, 2–4%, for $R = 0.5$ jet cones. The systematic uncertainty on the MPF method bias is computed as the difference between the γ+jet and dijet samples and found to be of the order of 0.1%.

2. *Zero suppression bias*

An off-line zero suppression further suppresses the energies of calorimeter cells in order to reduce the amount of noise, in particular in the coarse hadronic section, that can contribute to jet energies. The algorithm used for this zero-suppression retains calorimeter cells if their energy exceeds the average baseline noise by 4σ, where σ represents the measured standard deviation of the noise for a given cell. Neighboring cells are also retained if their energy exceeds a threshold of 2.5σ.

The zero-suppression algorithm produces a small positive noise offset contribution because of the asymmetric zero suppression (negative energies are never kept). For cells with high enough real energy deposits, as within the jet core, the zero-suppression produces no net offset, and positive and negative noise offset contributions are expected to cancel. Conversely, the energies measured for particles incident on the calorimeter, including those from uranium decay, are reduced by the zero-suppression when cells are below threshold. Therefore the average offset within a jet is different from the offset outside of a jet which we measure using zero bias and minimum bias events.

The true offset is increased inside the jet environment compared to the average energy density measured outside jets in zero bias and minimum bias events. The correction factor for the true offset inside a jet, k_O, is defined as

$$k_O = \frac{\left\langle E^{\rm jet}_{\rm meas}(\text{no ZB overlay})\right\rangle}{\left\langle E^{\rm jet}_{\rm meas}(\text{ZB overlay}) - O_{\rm meas}\right\rangle}, \qquad (15)$$

where $E^{\rm jet}_{\rm meas}$ is the energy of a reconstructed jet and $O_{\rm meas}$ is the measured offset correction described in Sec. V A. The same MC events are reconstructed with and without zero bias event overlay (offset). The zero bias event sample was collected without any calorimeter zero suppression so that its effect can be studied in detail. Figure 17 shows the effect of zero-suppression on the offset correction for jets in the CC. For jet $p'_T > 50$ GeV, where $p'_T = E'/\cosh\eta_{\rm jet}$, the resulting bias on jet energy varies between 5% at low p'_T and 2% at higher p'_T.

The bias in offset is almost fully canceled by an opposite bias in the MPF response, defined as

$$k_R = \frac{\langle R_{\rm had}(\text{no ZB overlay})\rangle}{\langle R_{\rm had}(\text{ZB overlay})\rangle}, \qquad (16)$$

because the increased offset inside the jet increases the $\not\!\!E_T$ in the photon direction. This artificially increases the estimated MPF response (see Eq. 5). Only the ratio k_O/k_R is therefore relevant for the final bias correction due to the zero suppression bias. The combined bias is

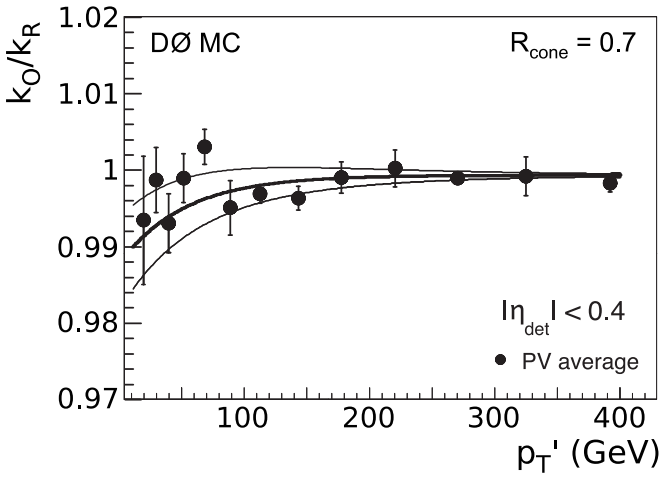

FIG. 18: Zero suppression bias k_O/k_R in CC. The outer solid lines show the uncertainty attributed to the bias correction and the 1σ contours.

found to be less than 0.5% for jet $p_T > 50$ GeV in all rapidity bins, largely cancelling the topological bias, and approaches zero at high p_T, as shown in Fig. 18.

3. *Rapidity bias*

Since the inclusive jet cross section is measured in bins of rapidity, we checked for any potential bias in the reconstruction of jet rapidity using the simulation, as shown in Fig. 19. The rapidity is generally biased towards the central calorimeter, with the largest deviations observed in the ICR. This is attributed to detector effects in the ICR in addition to the jet cone algorithm itself. The absolute effect on the inclusive jet measurement is small compared to the effect of jet p_T calibration.

E. Final jet energy scale corrections and uncertainties

Figure 20 shows the jet energy scale corrections as a function of jet p_T for central and forward rapidity, and as a function of jet rapidity at low and high jet p_T. The corrections range between 1.2 and 1.8 for the kinematic range of the cross section measurement. The response correction is by far the largest one, while the showering correction starts to be noticeable at large rapidity. At high rapidity, the actual angular distance for each $\Delta\eta$ bin is small, while the radius of the showering is slightly increasing due to the increasing energy of the jet at fixed p_T as one goes forward. The total correction is computed using Eq. 3. The combined effects of the uncertainties associated with each component of the correction are summarized in Fig. 21 as a function of jet p_T for central and forward rapidity, and as a function of jet rapidity for low and high jet p_T — high jet energy corresponds to low p_T

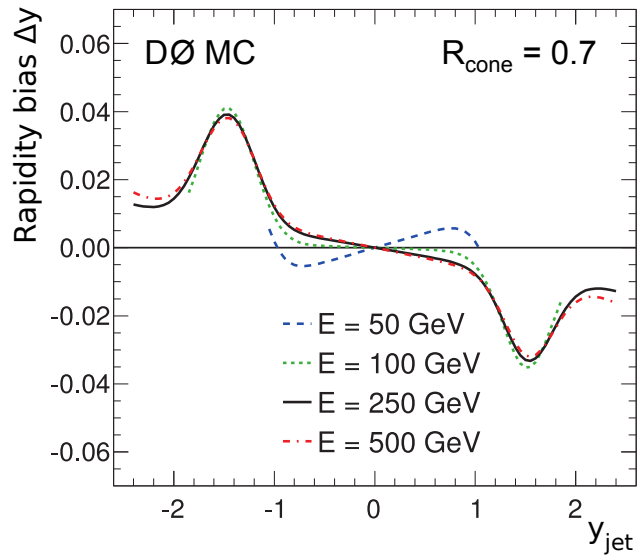

FIG. 19: (color online) Rapidity bias obtained in MC for different jet energies E. The curves cover the range $p_T > 30$ GeV and $|y_{\rm jet}| < 2.4$.

at high rapidity.

The corrections do not show a significant dependence as a function of jet rapidity except in the region of the ICR. The uncertainties vary between 1.2 and 2.5% for the kinematic range of the cross section measurement and are dominated by the uncertainties of the jet response. The uncertainties obtained in the CC and for jet $p_T \approx 100$–500 GeV are the smallest ones obtained by any experiment operating at a hadron collider. These uncertainties do not depend strongly on jet pseudorapidity and p_T.

F. Closure tests

The aim of the closure tests is to verify the accuracy of the jet energy scale correction using either MC or data and to evaluate the remaining difference as an additional systematic uncertainty related to the method. As an example, one test is to use the full method in MC and to compare the results with the particle level jet energy. The direct closure variable is defined as

$$D = \frac{\left\langle E_{\rm jet}^{\rm corr} \right\rangle}{\left\langle E_{\rm jet}^{\rm particle} \right\rangle}, \tag{17}$$

where $E_{\rm jet}^{\rm corr}$ is the corrected jet energy and $E_{\rm jet}^{\rm particle}$ is the energy of the closest particle jet matching the reconstructed jet within $\Delta R < R_{\rm cone}/2$. Results from the direct closure test are shown in Fig. 22 in two regions of jet rapidity. We note that we obtain consistency of the method within statistical uncertainties (D is close to unity within less than 1%) and no additional systematic

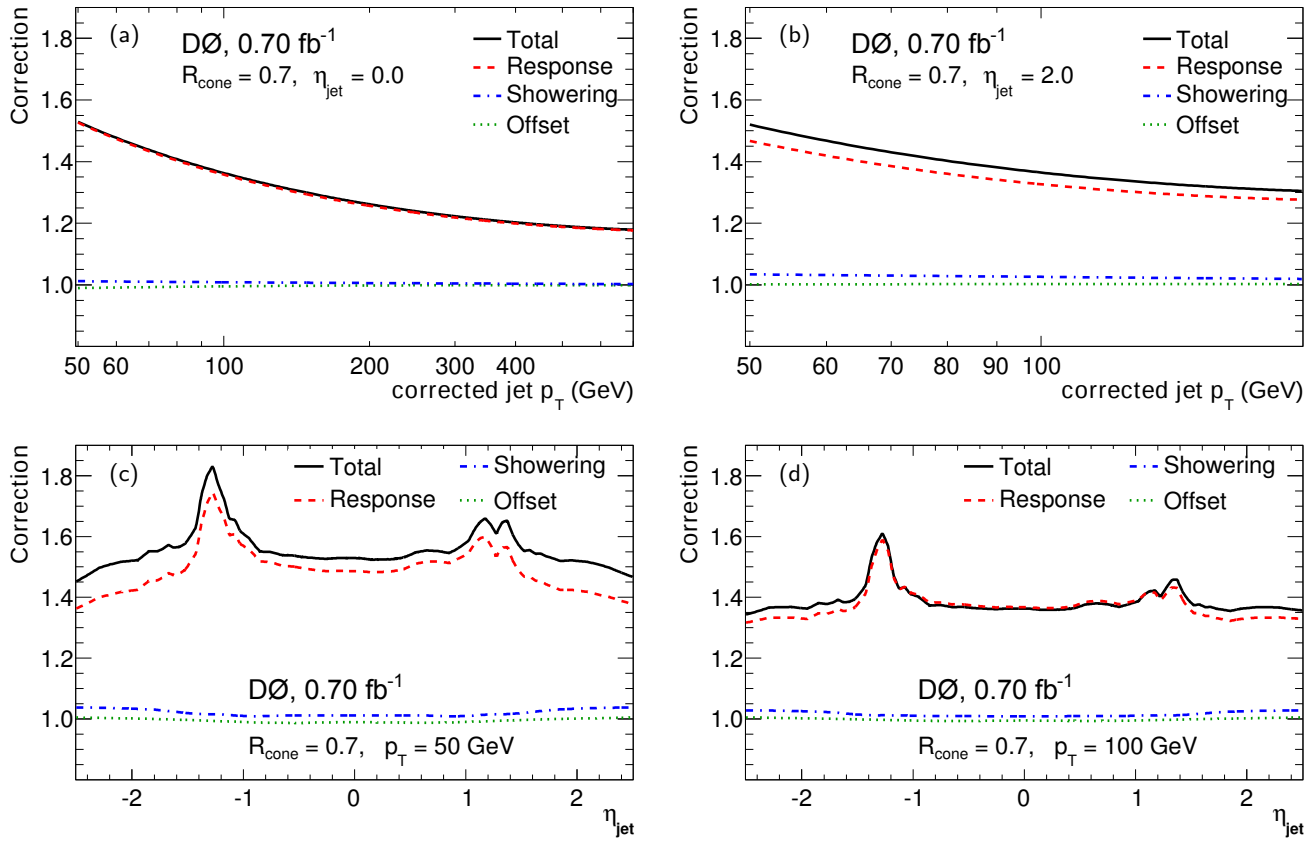

FIG. 20: (color online) Jet energy scale corrections as a function of jet p_T for (a) central and (b) forward rapidity, and as a function of jet rapidity for (c) low and (d) high jet p_T.

uncertainty is introduced. Closure tests using data are performed relative to MC by comparing ratios of fully corrected jet energies $< E_{data}^{corrected} > / < E_{MC}^{corrected} >$ in fixed regions of E' and η. Again we find good agreement within the expected uncertainties of the jet energy scale.

VI. TRIGGERING ON JETS

In this section, we briefly describe how we determine the absolute jet trigger efficiencies. Two different samples based on jet or muon triggers are used. The D0 trigger system is composed of three consecutive levels called L1, L2, and L3. At L1, a single jet trigger typically requires n calorimeter trigger towers above a given threshold, where a trigger tower is defined by the hardware summation of energies in 2×2 calorimeter towers. The trigger towers are read out separately from the precision calorimeter electronics via a fast digitizer and are used in both L1 and L2 triggers. All events used in this analysis are required to pass a trigger designed to fire if a single jet with $p_T > 50$ GeV is in the event. For instance, the 65 GeV single jet trigger requires the presence of three calorimeter towers with a transverse momentum above 5 GeV. This requirement is often satisfied by the presence of trigger towers belonging to different jets, ensuring high trigger efficiency. In most of these events, there are two high-p_T jets in the event or more than two low-p_T jets, which ensures that the event passes the L1 threshold. A detailed analysis shows that the L1 single jet efficiency is more than 98% for the full kinematic range of our measurement, which is corrected for the residual inefficiency. At L2 we perform a clustering of the trigger tower energies and apply a threshold based on the p_T of highest energy cluster. Seven L3 triggers corresponding to uncorrected L3 jet p_T thresholds of 8, 15, 25, 45, 65, 95, and 125 GeV are used in the analysis. The highest-p_T L3 trigger was never prescaled during data collection. In Fig. 23, we show the jet cross section before any unfolding corrections as a function of jet p_T for the different jet triggers for two domains in jet rapidity $|y| < 0.4$, and $2.0 < |y| < 2.4$.

The first method used for computing the jet efficiency is to obtain the relative jet trigger efficiency with respect to the lower p_T jet trigger. For instance, the ratio of the 95 and 65 GeV triggers is shown in Fig. 24. For this purpose, we plot the ratio of the number of events that pass the 95 GeV trigger to those that pass the 65 GeV threshold as a function of jet p_T after jet energy scale and vertex efficiency corrections to cancel known luminosity dependencies as discussed in Sec. VII. The ratio

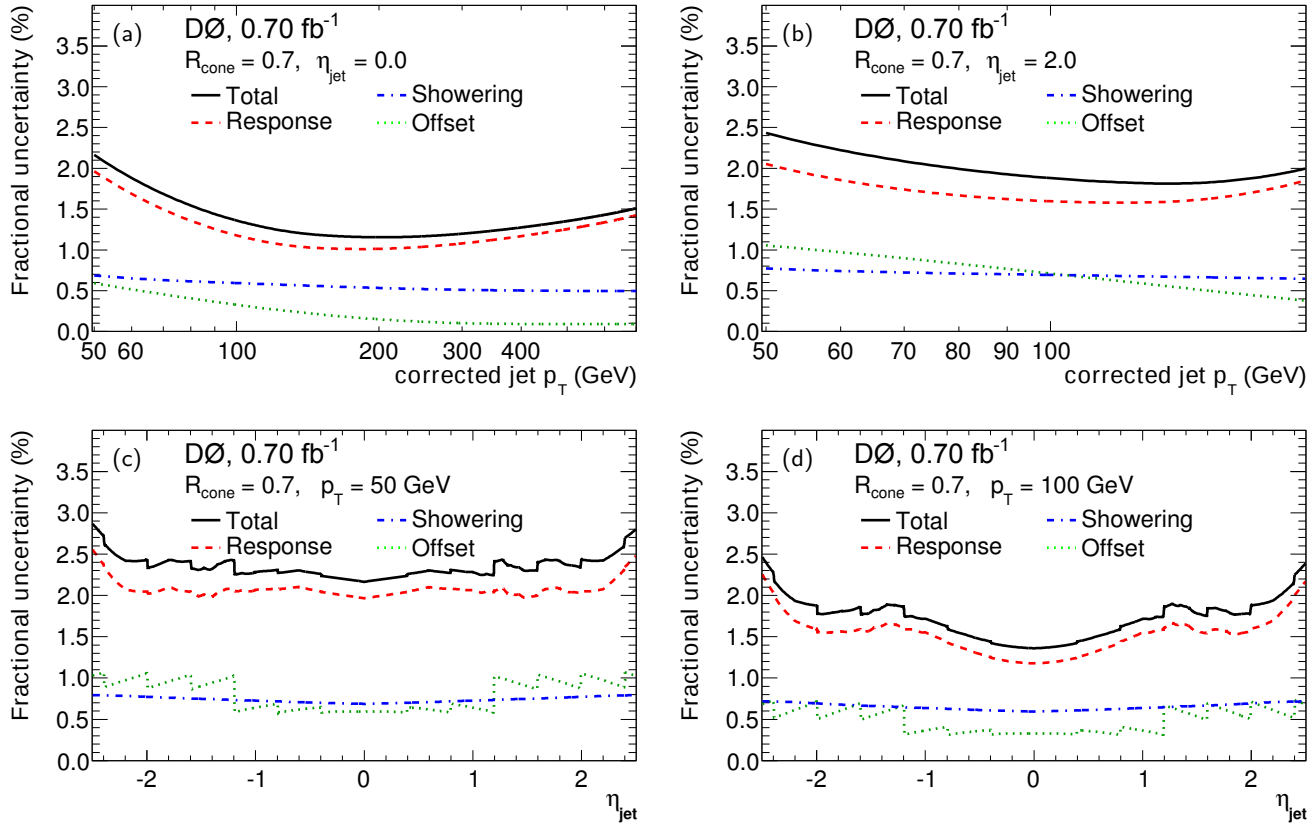

FIG. 21: (color online) Jet energy scale uncertainties as a function of jet p_T for (a) central and (b) forward rapidity, and as a function of jet pseudorapidity for (c) low and (d) high jet p_T.

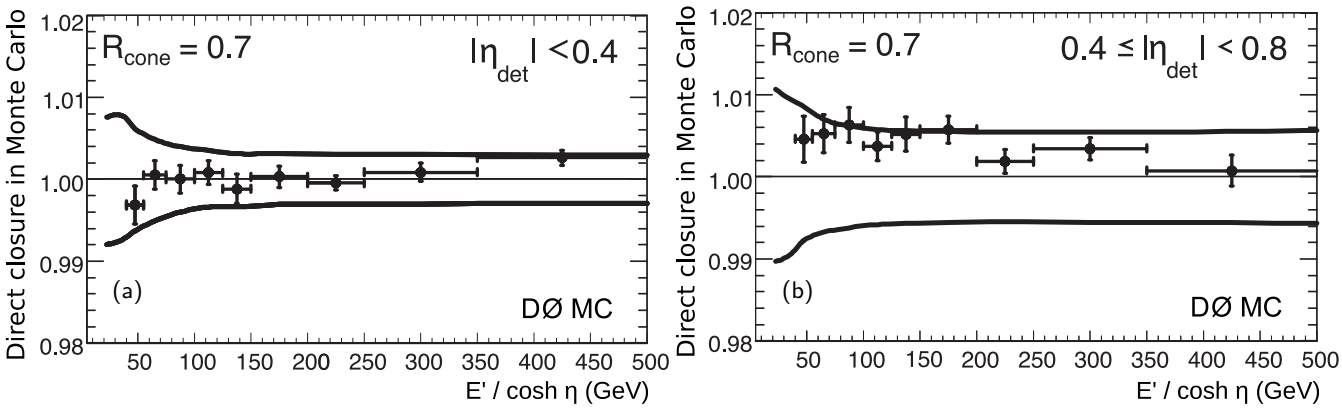

FIG. 22: Closure test of jet energy scale in MC for (a) $|\eta_{det}| < 0.4$ and (b) $0.4 < |\eta_{det}| < 0.8$. The band outlined by the solid curves corresponds to the uncertainties in the extraction of jet energy scale in MC which are mainly statistical.

is scaled by the relative integrated luminosities of these triggers to account for the different prescales. When this ratio reaches 1, the 95 GeV threshold trigger is 100% efficient with respect to the 65 GeV one. A fit to this ratio gives the different thresholds for which the triggers are fully efficient (>99.9%). The jet energy scale corrected p_T at which each trigger becomes fully efficient is given in Table I. These thresholds take into account the p_T binning used in the analysis and can be significantly higher than the minimum usable threshold. We note that this method does not allow us to obtain the absolute trigger efficiency since it gives all efficiencies with respect to the lowest 8 GeV p_T trigger as a reference.

A second method is used to measure the absolute single jet trigger efficiency. It uses independent muon and minimum bias triggers. The minimum bias trigger only requires energy deposits in the luminosity monitors. As its name indicates, it shows very little selection bias and

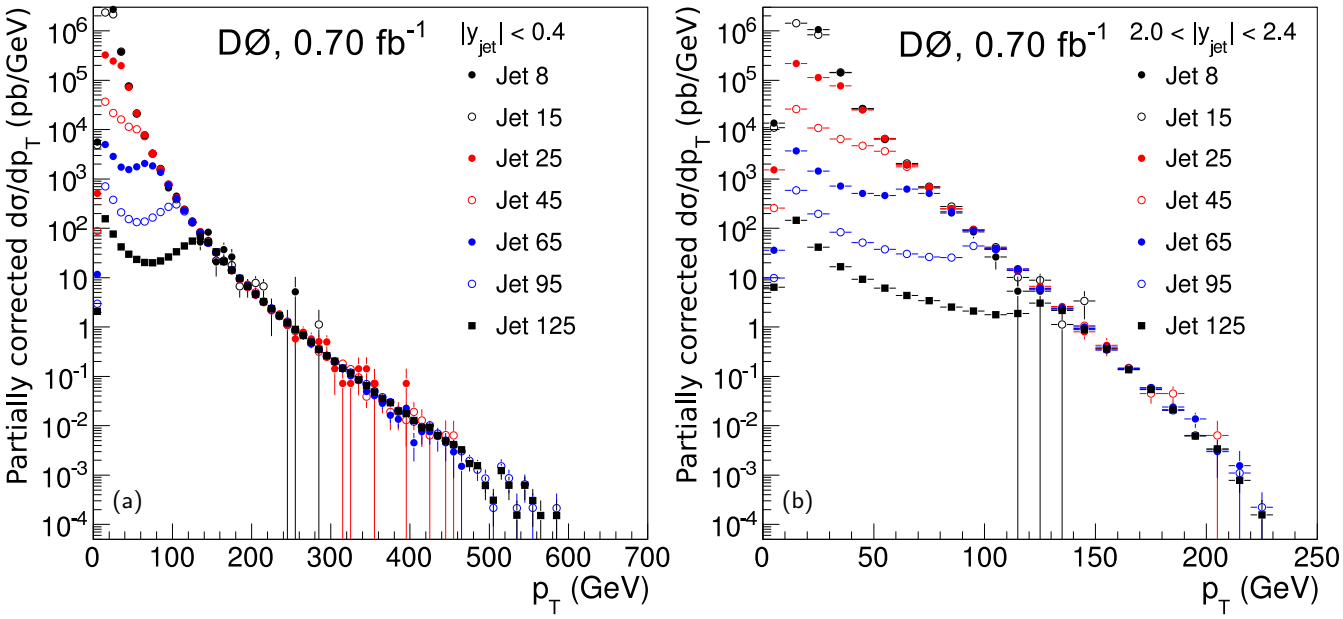

FIG. 23: (color online) Inclusive jet p_T cross section without unfolding corrections for the different single jet triggers as a function of jet p_T for (a) $|y| < 0.4$ and (b) $2.0 < |y| < 2.4$. The average prescales are 34000, 7100, 460, 41, 9.6, 1.4 and 1 for the 8, 15, 25, 45, 65, 95, and 125 GeV triggers, respectively.

is ideal for trigger studies. Unfortunately, the sample collected during all of Run II at the Tevatron at 0.5 Hz only yields statistics adequate to study jets below 70 GeV using this trigger, and this method does not allow exploration of the high p_T jet trigger efficiency. For this reason, inclusive muon triggers without any calorimeter requirements are also used. This allows us to check what fraction of the offline reconstructed jets in muon triggered events pass the calorimeter jet trigger requirement, providing a direct estimate of trigger efficiencies up to 400 GeV in the CC. The conclusion of this study is that all jet triggers are more than 98% efficient above the thresholds defined above, and the residual inefficiency is determined to a precision of better than 1%. Both methods to obtain the trigger efficiencies are useful since the muon triggers have a tendency to enrich the inclusive jet samples in b and c-jets where the b and c quarks decay leptonically, which might lead to different trigger efficiencies as a function of jet p_T.

Rapidity / L3 trigger	15	25	45	65	95	125
$\lvert y\rvert < 0.4$	50	60	100	120	160	200
$0.4 \leq \lvert y\rvert < 0.8$	50	60	100	120	160	200
$0.8 \leq \lvert y\rvert < 1.2$	50	90	110	140	190	230
$1.2 \leq \lvert y\rvert < 1.6$	50	80	90	140	190	240
$1.6 \leq \lvert y\rvert < 2.0$	50	70	90	110	160	190
$2.0 \leq \lvert y\rvert < 2.4$	50	70	90	120	160	200

TABLE I: Jet energy scale corrected p_T in GeV at which each L3 trigger becomes fully efficient in different jet y bins.

VII. EVENT SELECTIONS AND EFFICIENCIES

In this section, we discuss the selections that are used to remove background events in the sample. The selections fall into three different categories. The event quality flags remove events suffering from diverse calorimeter noise issues. The vertex requirement selects events with a high quality vertex close to the center of the calorimeter to improve the jet p_T and y measurements and to reduce the background from cosmic ray events. The $\not\!\!E_T$ requirement is designed to remove the remaining cosmic ray background, especially at high jet p_T.

A. Event quality flags

Event quality flags ensure that the subdetectors used in the analysis were working properly when the data were collected. Calorimeter event quality flags allow removal of events showing coherent pedestal shifts in the analog-to-digital converters, parts of the calorimeter not correctly read out, or high coherent noise. This is especially important for high-p_T jets which can originate artificially from noisy towers in the calorimeter. Note that the vertex and $\not\!\!E_T$ requirements also remove most of these events. The inefficiency induced by the calorimeter event quality flag rejection is estimated using an independent sample whose trigger is known to be unaffected by the calorimeter problems, the zero bias trigger. The inefficiency is calculated to be $(3.2 \pm 1.0)\%$ where the 1.0% uncertainty covers the time and luminosity dependence of the inefficiency.

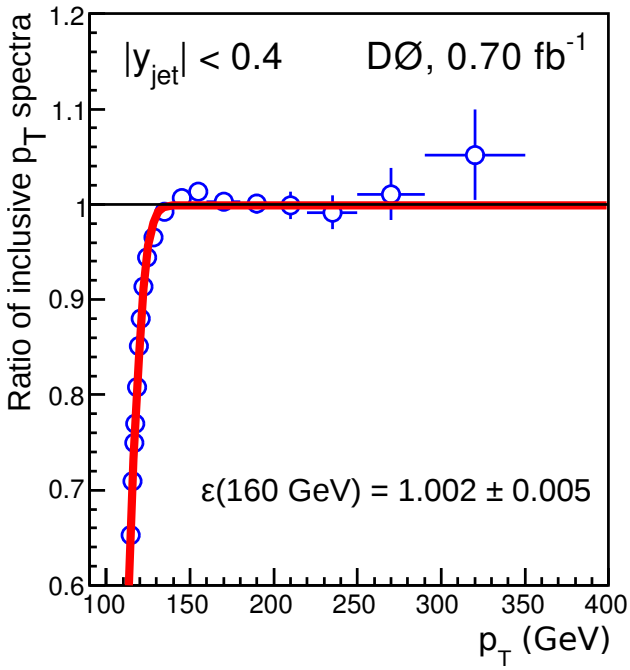

FIG. 24: (color online) Ratio of two consecutive jet triggers used to obtain the relative jet trigger efficiency for the 95 and 65 GeV single jet triggers. The fit of the turn-on curve determines the 95 GeV jet p_T 99%-threshold to be 130 GeV. A higher threshold of 160 GeV that is consistent with an efficiency $\epsilon = 1.00$ is used in the final analysis.

B. Reconstructed vertex requirement

The vertex selection is based on three different requirements: there must be at least one reconstructed vertex, the z-position along the beam line of the primary reconstructed vertex must be within 50 cm of the detector center ($|z_{\rm vertex}| < 50$ cm), and the number of tracks fitted to the vertex has to be at least three to ensure an accurate measurement. The z-vertex position requirement ensures that the vertex is in the high efficiency tracking region. The third requirement rejects vertices originating from fake high p_T tracks. To each reconstructed vertex is assigned a probability that it comes from a minimum bias interaction based on the $\ln(p_T)$ distributions of the tracks with $p_T > 0.5$ GeV pointing to the vertex. The vertex with the lowest minimum bias probability is selected as the primary vertex.

The efficiency of reconstructing a vertex with at least three tracks pointing to it (without the requirement on the z-vertex position) is found to be $(99.6 \pm 0.4)\%$, independent of jet p_T and y. The observed 0.4% inefficiency is consistent with about 0.6% of the primary vertices not being reconstructed because of tracking inefficiencies, and 0.2% being replaced by a minimum bias vertex.

The leading inefficiency comes from the requirement on the vertex position along the z-axis. The fraction of events rejected by this requirement is of the order of 7%. To determine the efficiency of this requirement we take into account the shape of the luminous region. The longitudinal shape of the luminous region is approximated by the expression

$$\frac{d\mathcal{L}(z)}{dz} = N_p N_{\bar{p}} \frac{1}{\sqrt{2\pi}\sigma_z} \frac{e^{-(z-z_{0z})^2/2\sigma_z^2}}{4\pi\sigma_x(z)\sigma_y(z)}, \qquad (18)$$

where the overlap of the proton and antiproton beam bunches having N_p and $N_{\bar{p}}$ particles is described with a Gaussian distribution of width σ_z in the z direction, with a possible offset z_{0z} relative to the nominal interaction point. $\sigma_x(z)$ and $\sigma_y(z)$ represent the transverse size of the beam spot and vary as a function of z:

$$\sigma_T^2(z) = \frac{1}{6\pi\gamma}\epsilon_T\beta_T^* \left[1 + \frac{(z - z_{0T})^2}{\beta_T^{*2}}\right]. \qquad (19)$$

Here T is either x or y, z_{0T} is the minimum of the β function describing the beam dimensions near the interaction point in direction T and any offset in the x and y directions with respect to the nominal interaction point, γ is the Lorentz factor of the beam particles. The emittance ϵ_T and beta parameter β_T^* describe the beam dimensions at the interaction point. The parameterization can be integrated to yield

$$\epsilon_{|z_{\rm vertex}|<50\ {\rm cm}} = \frac{\int_{-50\ {\rm cm}}^{50\ {\rm cm}} f(z_{\rm vertex}, {\rm run}, \mathcal{L})}{\int_{-140\ {\rm cm}}^{140\ {\rm cm}} f(z_{\rm vertex}, {\rm run}, \mathcal{L})}, \qquad (20)$$

where the limits of integration in the denominator come from the requirements used in the luminosity determination. This parameterization is fitted to minimum bias data in the high tracking efficiency region ($|z_{\rm vertex}| < 40$–60 cm) in bins of instantaneous luminosity for several run ranges (the changes in beam optics as a function of time affect the beam shape as described by the β^* parameter). The changes as a function of instantaneous luminosity are primarily due to the variations in the beam parameters during a store. The vertex efficiency varies by up to 6% as a function of instantaneous luminosity and by up to 4% as a function of the period of data taking for a fixed value of luminosity. The parameterizations have been determined as a function of time and instantaneous luminosity, and are applied as such on a per-event basis. Figure 25 shows the mean vertex efficiency as a function of instantaneous luminosity, with the range of efficiencies overlaid. The uncertainty on the vertex acceptance is estimated to be 0.5% by comparing results from fits to minimum bias data at $|z_{\rm vertex}| < 60$ cm and $|z_{\rm vertex}| < 40$ cm. In addition, an increased uncertainty of 0.4% added in quadrature at high $|y|$ is introduced to account for the possibility of a lower vertex reconstruction efficiency.

C. Missing transverse energy requirement

A requirement on the missing transverse energy in an event is applied to remove the remaining background

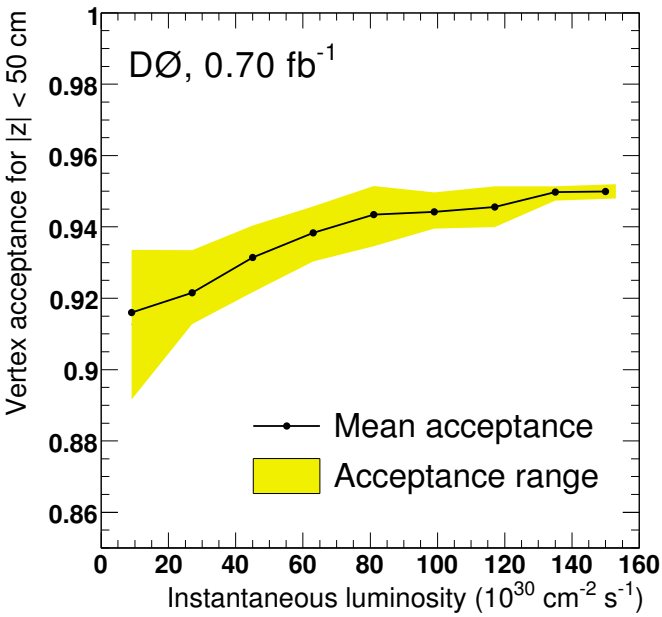

FIG. 25: (color online) Vertex acceptance for the requirement on the z-vertex position $|z_{\rm vertex}| < 50$ cm as a function of instantaneous luminosity. The shaded band indicates the variation for different running periods.

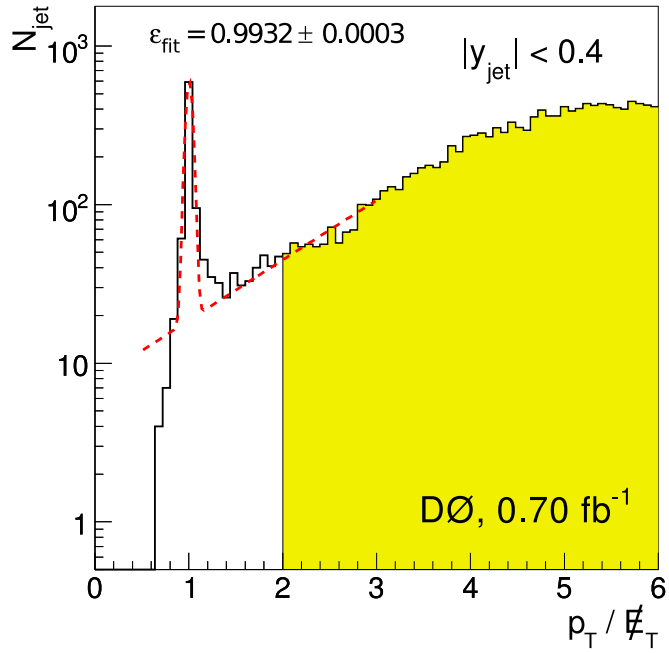

FIG. 26: (color online) Distribution of $p_{T,\rm lead}/\not{E}_T$ for jet events with leading jet $p_T > 200$ GeV. A peak from cosmic ray background is visible around 1. The shaded region shows jets passing the $p_{T,\rm lead}/\not{E}_T$ requirement.

from cosmic rays that induce showers in the calorimeter. The cross section for these cosmic ray interactions falls much less steeply versus p_T than the inclusive jet cross section, and is typically comparable at $p_T \approx 400$ GeV. The issue of background from cosmic rays is thus more important for high-p_T jets. Fortunately, cosmic ray showers deposit most of their energy on one side of the calorimeter, have no reconstructed vertex, and produce high uncorrected $\not{E}_T$ that peaks at $p_{T,\rm lead}/\not{E}_T \approx 1$ where $p_{T,\rm lead}$ is the uncorrected p_T of the leading jet of the event. These events are fully and efficiently removed by requiring $p_{T,\rm lead}/\not{E}_T > 1.4$, when $p_{T,\rm lead} < 100$ GeV and $p_{T,\rm lead}/\not{E}_T > 2.0$, when $p_{T,\rm lead} \geq 100$ GeV. Figure 26 shows the distribution of $p_{T,\rm lead}/\not{E}_T$ for the high-p_T jet trigger with $p_T > 200$ GeV, with the selected events at $p_{T,\rm lead}/\not{E}_T > 2.0$ shown by the shaded region. A spike coming from cosmic ray events is visible at 1. An upper limit of 0.4% is estimated on the inefficiency of the $\not{E}_T$ requirement and used as an uncertainty, but no correction is applied. This upper limit is based on studies of fits of distributions like the one in Fig. 26, and track-matching inefficiency for jets since cosmic ray events are usually out-of-time with the tracking read-out.

VIII. JET IDENTIFICATION REQUIREMENTS AND EFFICIENCIES

The jet identification requirements are designed to remove instrumental backgrounds such as jets formed from sources of transient noise in the calorimeter and also physics background from electrons and photons. The jet requirements are based on the fractions of jet energy deposited in the electromagnetic calorimeter (EMF) and in the coarse hadronic calorimeter (CHF). EMF< 0.95 is required to remove overlaps between jets and electromagnetic objects, i.e. electrons and photons. This retains true jets with a 99% efficiency. A lower limit on EMF (either 0 or varying between 0.03 and 0.05 depending on the pseudorapidity region in the calorimeter) as well as an upper limit on CHF (varying between 0.4 and 0.6) removes jets that are formed predominantly out of noise in the hadronic calorimeter. An additional requirement, L1 confirmation, is based on the ratio of the p_T as measured by the L1 trigger system and as measured by the precision read-out. It is required to be above 0.5 for jet $p_T <$ 80 GeV, and there is no requirement for higher p_T jets. This removes jets formed out of noise, for example due to coherent noise in the precision readout electronics.

The jet identification efficiencies are determined using a data driven method. This method uses track jets which are jets built with a cone algorithm using charged particle tracks instead of calorimeter energy clusters. We select a leading p_T tagged object, which in this case is a photon or a track jet associated with a good calorimeter jet, and a probe object, which is the leading track jet that is back-to-back in ϕ with the tag object. Events with additional track jets are vetoed to ensure that the leading objects are balanced in p_T. The reconstruction efficiency is defined as the fraction of probe objects with a calorimeter jet found within the 0.7 jet cone, and the jet identification efficiency is the fraction of those calorimeter jets pass-

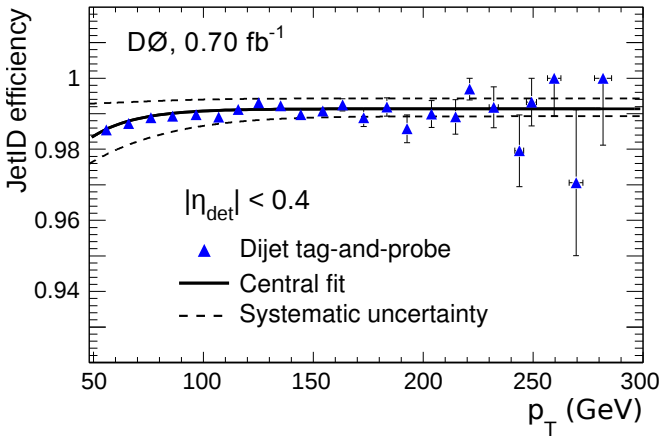

FIG. 27: (color online) Jet identification efficiencies obtained for the dijet sample. Dashed lines indicate the systematic uncertainty.

ing the jet identification requirements. The data driven method has been used for three different samples: dijet, γ+jet and, Z+jet, which all lead to the same result. The central value for the jet identification efficiency shown in Fig. 27 is taken from the dijet sample. The efficiency for $p_T > 50$ GeV, where we perform the measurement of the inclusive jet p_T cross section, is 99% in all calorimeter regions except in the region $0.8 < |y| < 1.2$ where it is about 98%.

Because the data driven method is used for calorimeter jets that are independently identified as track jets, we also directly measure the efficiencies by computing the fraction of events removed by each jet identification requirement individually after applying all other requirements in the inclusive jet sample. This method assumes that each jet identification cut removes only good jets. The efficiencies described above are found to be in good agreement with those from the tag-and-probe method.

IX. JET TRANSVERSE MOMENTUM RESOLUTION

In this section, we discuss the determination of the jet p_T resolution, which is needed for the unfolding of the inclusive jet p_T cross section. The jet p_T resolution is determined from data using the dijet asymmetry distribution, which can be obtained with minimal input from MC. This method requires corrections for the presence of additional unreconstructed jets (soft radiation), momentum imbalance at the particle level, and asymmetry bias due to non-Gaussian tails. We describe each correction needed to obtain the jet p_T resolution.

A. Dijet asymmetry

The jet p_T resolutions are determined starting from the dijet asymmetry

$$A = \frac{p_{T,1} - p_{T,2}}{p_{T,1} + p_{T,2}} \tag{21}$$

computed in a pure dijet sample with no additional jet identified, where $p_{T,1}$ and $p_{T,2}$ are the p_T of the leading and second-leading jets and the two leading jets are randomly assigned an index of 1 or 2. Both jets are required to be back-to-back with $\Delta\phi > 3.0$ to avoid any large effects from QCD radiation. The RMS of the asymmetry distribution is directly proportional to the jet p_T resolution

$$\sigma_A = \frac{1}{\sqrt{2}} \frac{\sigma_{p_T}}{p_T}, \tag{22}$$

if the jets are in the same y region to ensure that the p_T resolution of both jets is the same. To characterize the p_T dependence of the resolution for a single jet, σ_A is measured in bins of $p_T = (p_{T,1} + p_{T,2})/2$. This method can be used directly to measure the jet p_T resolution in the central region where the statistics are high. However, in the forward region, the statistics for forward-forward jet pairs is small compared to central-forward jet pairs. If one of the jets is in the central region and the other in the forward region, it is possible to infer the jet p_T resolution σ_{p_T} in the forward region once the resolution for jets in the central reference region $\sigma_{\rm ref}$ is known

$$\frac{\sigma_{p_T}}{p_T} = \sqrt{4 \cdot \sigma_A^2 - \left(\frac{\sigma_{\rm ref}}{p_T}\right)^2}. \tag{23}$$

The central reference region used in this study is $|y_{\rm ref}| < 0.8$, with the probe jet binning following the same 0.4 binning in rapidity as the rest of the analysis. The asymmetry distribution in the central region is shown in Fig. 28 for $80 < p_T < 100$ GeV as an example and other p_T^{jet} bins also show similarly small non-gaussian tails.

B. Corrections to the resolution

The jet p_T resolution determined from the dijet asymmetry can be affected by physics and instrumental effects. The final parameterization of the resolution used in this analysis includes corrections to remove biases in the measurement as described below.

1. *Soft radiation corrections*

The asymmetry method to compute the jet p_T resolution is biased by the presence of non-reconstructed jets in the sample. The p_T threshold to reconstruct a jet is 6 GeV, and requesting the presence of only two jets in the

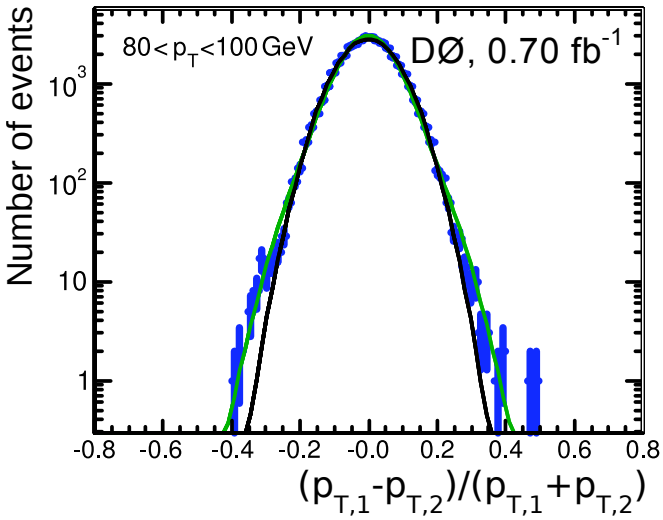

FIG. 28: (color online) Asymmetry distribution for jets in the central region with $80 < p_T < 100$ GeV. The probe jet is at $|y| < 0.4$, the reference jet at $|y_{\rm ref}| < 0.8$. The two lines display the result of a Gaussian fit and a Gaussian with smeared exponential tails (see Sec. IX C).

sample to compute the asymmetry does not ensure the absence of jets with p_T below 6 GeV. The corrections for such soft radiation are determined directly in data. We compute the asymmetry and the jet p_T resolution for different p_T thresholds for jet reconstruction, namely 7, 8, 10, 12, 15, 20, and 40 GeV. The jet p_T resolution as a function of the jet reconstruction threshold is shown in Fig. 29 (a) for one bin in jet p_T and $|y|$. A linear fit allows for extrapolating the jet p_T resolution to a threshold p_T of 0. The soft radiation factor,

$$K_{\rm soft} = \frac{\sigma_{p_T}(p_{T,\rm soft}^{\rm cut} \to 0)/p_T}{\sigma_{p_T}(p_{T,\rm soft}^{\rm cut} = 6\ {\rm GeV})/p_T}, \tag{24}$$

is studied as a function of the average jet p_T in each $|y|$ bin as illustrated in Fig. 29 (b). To better describe the low p_T region and limit the statistical fluctuations, the dependency of $K_{\rm soft}$ versus p_T is fitted with

$$K_{\rm soft}(p_T) = 1 - \exp(-p_0 - p_1 p_T), \tag{25}$$

where p_0 and p_1 are two parameters of the fit.

2. *Particle imbalance and combined corrections*

The remaining correction needed to obtain the final jet p_T resolution is the particle imbalance correction. Even in the ideal situation of only two particle jets and no soft radiation, the two jets are not necessarily perfectly balanced. In particular, fragmentation effects cause some energy and p_T to be found outside the jet cone. This effect is purely related to QCD and is determined using a MC simulation. The particle level imbalance is corrected for soft radiation using the same method as introduced for data

$$K_{\rm soft}^{\rm MC} = \frac{\sigma_{p_T}^{\rm ptcl}(p_{T,\rm ptcl}^{\rm threshold} \to 0)/p_T}{\sigma_{p_T}^{\rm ptcl}(p_{T,\rm ptcl}^{\rm threshold} = 6\ {\rm GeV})/p_T}, \tag{26}$$

$$\sigma_{\rm MC} = K_{\rm soft}^{\rm MC} \cdot \sigma_{p_T}^{\rm ptcl}, \tag{27}$$

where $\sigma_{p_T}^{\rm ptcl}$ is the resolution evaluated at the particle level in the MC and $p_{T,\rm ptcl}^{\rm threshold}$ is the p_T threshold of jet reconstruction at the particle level.

The corrected particle level imbalance $\sigma_{\rm MC}$ is subtracted in quadrature from the soft-radiation corrected resolution computed in data (see previous section),

$$\sigma_{\rm corr} = \sqrt{(K_{\rm soft}\sigma_{p_T})^2 - \sigma_{\rm MC}^2}. \tag{28}$$

The relative correction due to particle level imbalance is about (7–9)% in the CC, (2–6)% in the ICR and the EC, for $p_T > 50$ GeV. The systematic uncertainties on particle imbalance corrections are mainly due to the differences between the Gaussian one standard deviation and the RMS of the particle level imbalance distribution due to non-Gaussian tails. The RMS is used for the central correction. The main non-Gaussian tails in particle level imbalance corrections are caused by muons and neutrinos, which are not included in the definition of D0 particle jets.

C. Final jet p_T resolutions

Using the asymmetry method and the various corrections discussed above, we obtain the jet p_T resolutions shown in Fig. 30. The measured resolutions are fitted with the parameterization

$$\frac{\sigma_{p_T}}{p_T} = \sqrt{\frac{N^2}{p_T^2} + \frac{S^2}{p_T} + C^2}, \tag{29}$$

where N is the noise term, S the stochastic term, and C the constant term. The values of the parameters are given in Table II. These resolutions are used to obtain the inclusive jet p_T cross section as described in the next section.

We note that the resolution is not Gaussian at high p_T even in the central region because of calorimeter punch-through: jets at very high p_T are not always fully contained in the calorimeter and can deposit energy into the muon system. In Fig. 31 (a), we show the distribution of $(p_{T,\rm jet}/p_{T,\rm ptcl} - 1)$ — the ratio of the reconstructed to the particle level jet p_T — obtained from MC simulation of the detector in the central region of the calorimeter at high p_T. The ICR also exhibits non-Gaussian tails as shown in Fig. 31 (b), which are explained by the changing structure of the calorimeter in this region. The non-Gaussian tails are modeled using a smeared exponential

$$f(p_T, \mu, \sigma, P, \lambda) = (1-P) \cdot \frac{1}{\sqrt{2\pi}\sigma} e^{(p_T-\mu)^2/(2\sigma^2)}$$

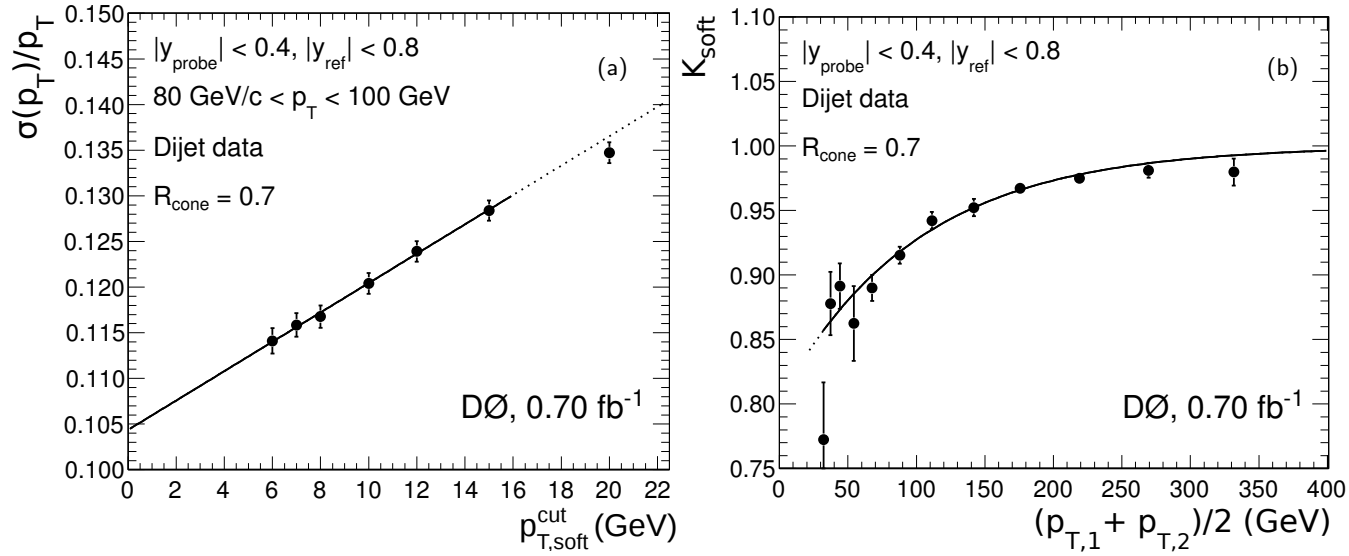

FIG. 29: (a) Jet p_T resolution extrapolated to a jet p_T reconstruction threshold of 0 GeV (in the $80 < p_T < 100$ GeV and $|y| < 0.4$ bin). (b) Soft radiation correction factor as a function of the average jet p_T for the $0.4 < |y| < 0.8$ bin. The solid lines are the fit result and the dashed lines are the result of the extrapolations.

$$+ \frac{P\lambda}{2} \cdot \exp\left[\lambda(p_T - \mu + \frac{\lambda\sigma^2}{2})\right] \times \mathrm{erfc}\left(\frac{p_T - \mu + \lambda\sigma^2}{\sqrt{2}\sigma}\right), \qquad (30)$$

with μ, σ, P, and λ as free parameters. The fitted shape from MC is scaled by varying the parameter σ such that folding the distributions for the leading jets with the exponential p_T spectrum from data results in precisely the same RMS of the jet p_T resolution as observed in data. This method can account for any shaping of the non-Gaussian tails that takes place due to bin-to-bin migrations in data. The full MC shape with tuned σ is later used in the unfolding of the data.

The uncertainties on jet p_T resolution are given in Fig. 32 for two bins in rapidity as an example. The uncertainties come primarily from the statistical uncertainties in the fits. An additional component is added to cover non-statistical variations between the fit model and the data. The total uncertainty coming from the jet p_T resolution is (5–10)% over the full kinematic range covered by the inclusive jet cross section measurement ($p_T > 50$ GeV). The leading systematic uncertainty in the central region is (4–5)% due to the uncertainties on the particle level imbalance corrections. In the ICR, an important systematic is due to the uncertainty on the tails in the resolution for this region. This systematic is estimated by varying the size of the tails by a factor of two, and is not included in the RMS of the resolution, but rather the resulting variation in shape was used in the unfolding procedure for data. Another important source of uncertainty is taken from the following MC closure test: the full resolution measurement using the asymmetry is redone using a full simulation of the D0 detector, and the difference between the MC input true resolution and the result of the method is taken as a systematic uncertainty. This amounts to up to about 10% uncertainty in the resolution at $p_T = 50$ GeV in the forward region.

	N(oise)	S(tochastic)	C(onstant)
$\lvert y\rvert < 0.4$	2.07	0.703	0.0577
$0.4 < \lvert y\rvert < 0.8$	2.07	0.783	0.0615
$0.8 < \lvert y\rvert < 1.2$	2.07	0.888	0.0915
$1.2 < \lvert y\rvert < 1.6$	2.07	0.626	0.1053
$1.6 < \lvert y\rvert < 2.0$	2.07	0.585	0.0706
$2.0 < \lvert y\rvert < 2.4$	2.07	0.469	0.0713

TABLE II: Parameters of the fits to the jet p_T resolution versus p_T for data. The noise term is fixed to the MC value with an uncertainty of 1 GeV since it is not constrained by the data.

X. JET RAPIDITY RESOLUTION

Compared to the jet p_T resolution, the rapidity resolution is a small effect which is determined using a MC simulation of the detector. The bin width in y is much larger than the y resolution and bin-to-bin migrations only occur at the bin edges. To unfold the effect of the rapidity resolution, a smooth parameterization of the resolution as a function of y is used. The result of the parameterization of the y resolution in different p_T bins is shown in Fig. 33.

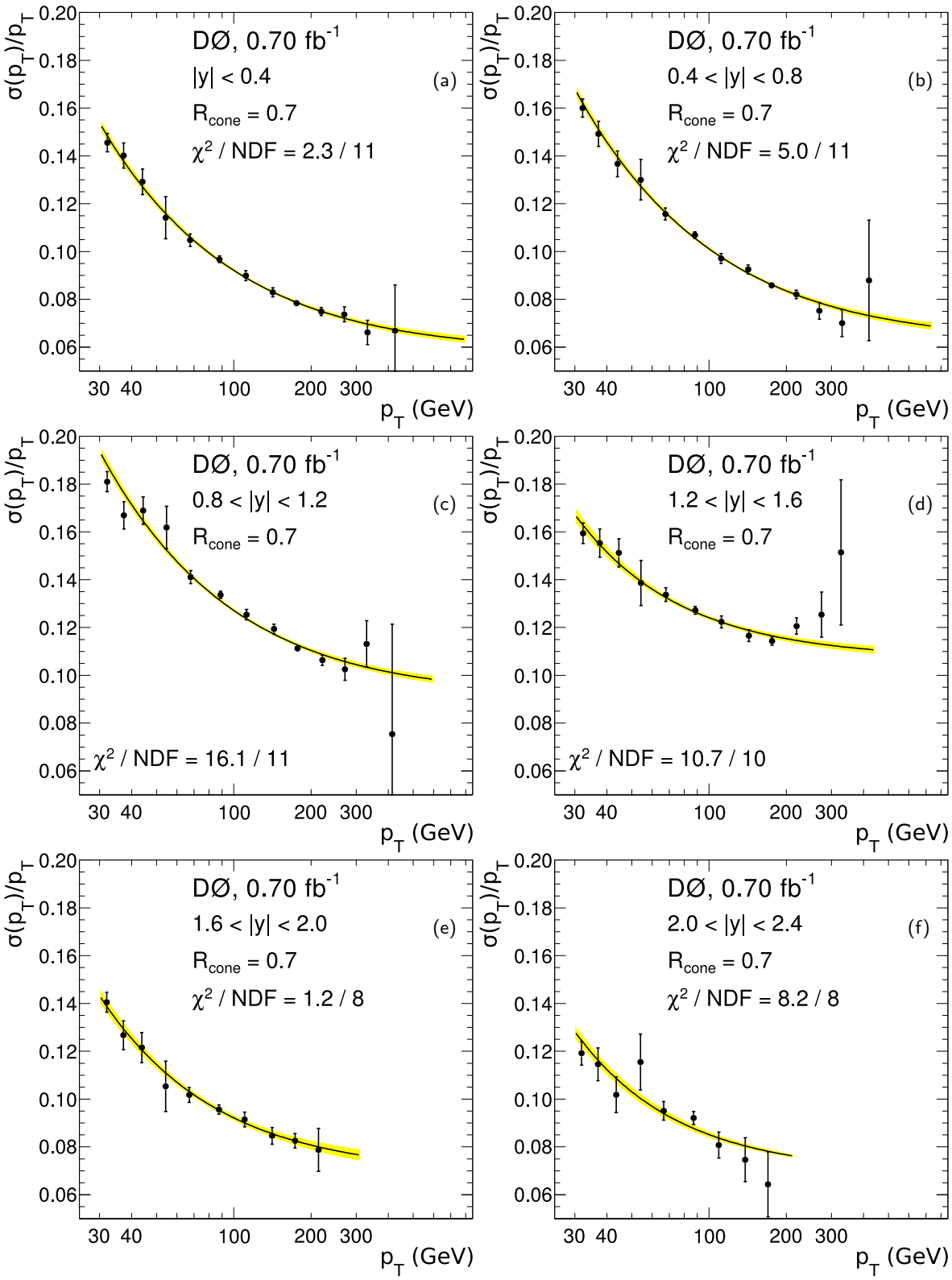

FIG. 30: (color online) Jet p_T resolution determined in data for the six rapidity regions. The solid curves are the results of the fit. The fit uncertainty is given by the shaded band.

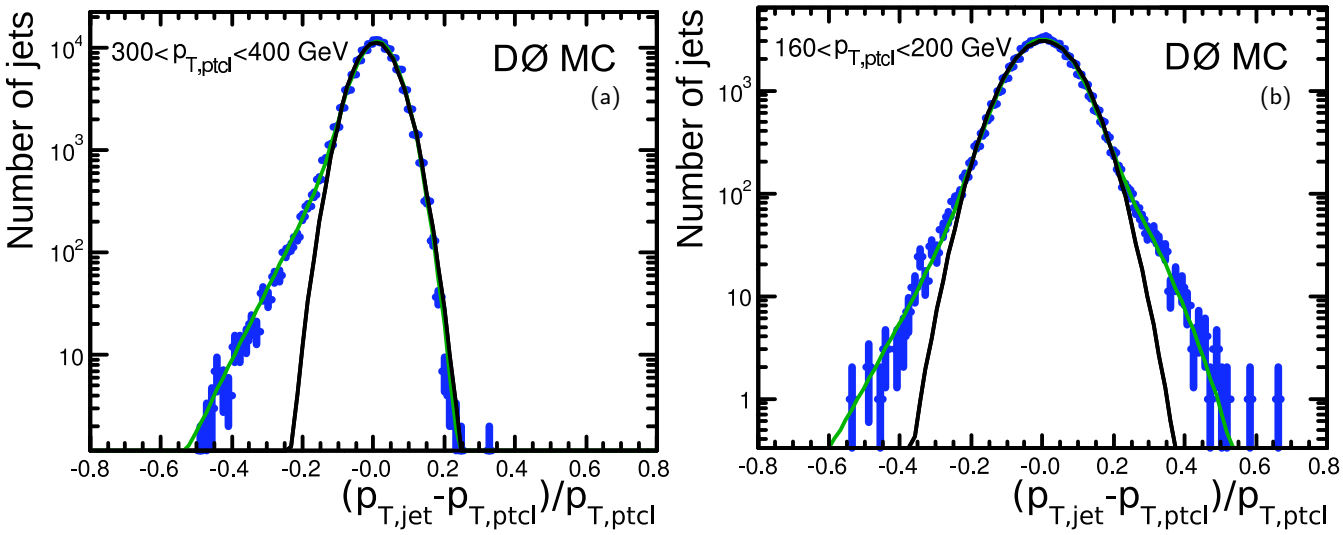

FIG. 31: (color online) (a) Example of punch through for $|y| < 0.4$ at high jet p_T for $300 < p_T < 400$ GeV and $|y| < 0.4$. (b) Example of tails of the jet p_T resolution in the ICR for $160 < p_T < 200$ GeV and $0.8 < |y| < 1.2$. The two curves are the result of the Gaussian fit and of a Gaussian plus exponential tails.

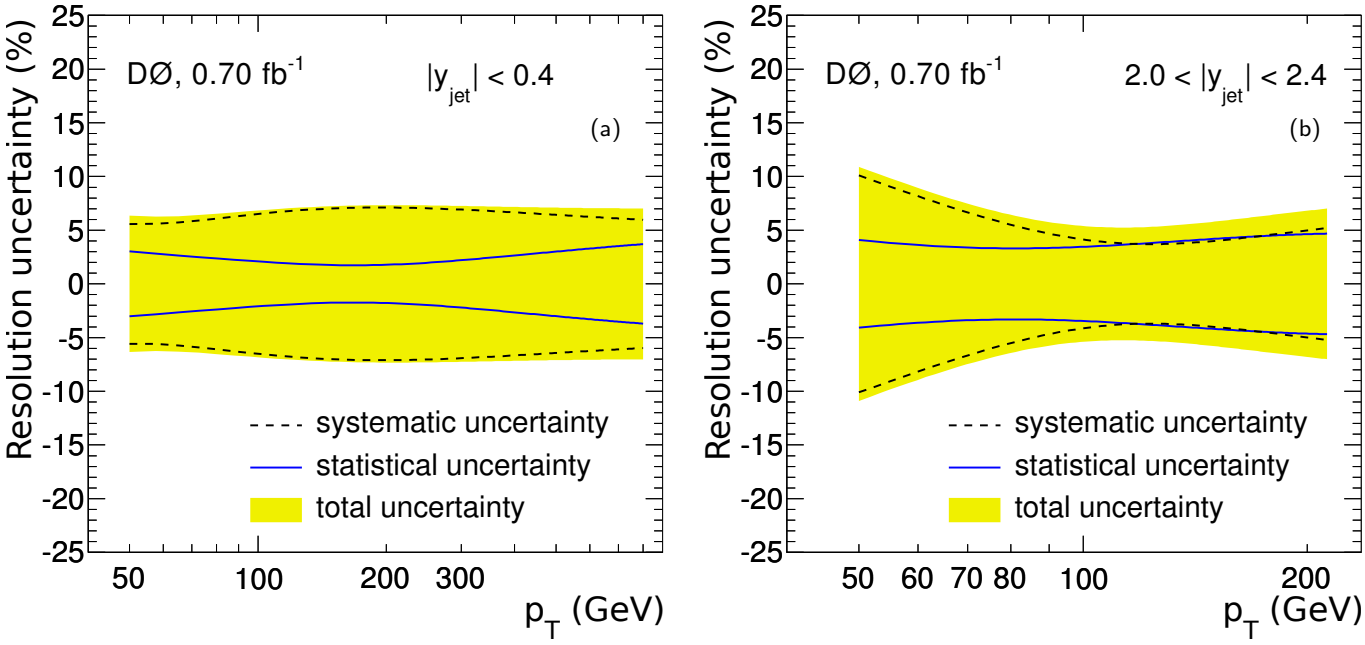

FIG. 32: (color online) Relative statistical and systematic uncertainties on jet p_T resolution for (a) $|y| < 0.4$ and (b) $2.0 < |y_{\rm jet}| < 2.4$.

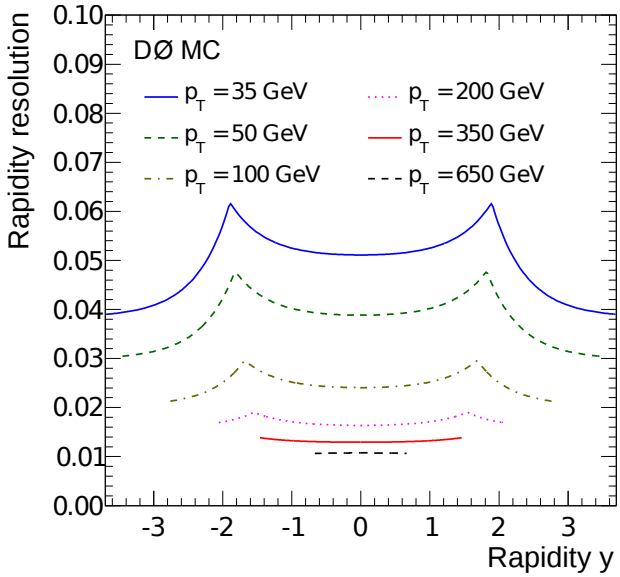

FIG. 33: (color online) Rapidity resolution (RMS) as a function of y in different jet p_T regions.

XI. UNFOLDING

In this section, we describe the method used to unfold the data as a function of jet p_T and y. As we already mentioned, the main smearing effect is due to the jet p_T resolution while the y smearing is only a second order effect. The steeply falling jet p_T cross section convoluted with the jet p_T resolution leads to an increase of the observed cross section as a function of the measured jet p_T. To unfold the data, we use the so-called ansatz method. We start with a functional form for the cross section that has only a few parameters, smear it with the jet p_T and y resolutions, and fit the parameters so that it describes the raw cross section measurement before unfolding.

The ansatz used in each rapidity bin contains a p_T dependence term and an additional rapidity dependence

$$f(p_T,\eta) = N_0 \left(\frac{p_T}{100\ \mathrm{GeV}}\right)^{-\alpha} \left[1 - \frac{2p_T \cosh(|y_{\min}|)}{\sqrt{s}}\right]^{\beta} \cdot \exp\left(-\gamma p_T\right). \quad (31)$$

Here $\sqrt{s} = 1960$ GeV is the center-of-mass energy and $|y_{\min}|$ is the low edge of the bin in absolute rapidity. The ansatz is based on phenomenological fits and motivated by the parton model [27]. The exponential term represents hydrodynamic production by freezing out particles from the quark and gluon sea. The value of γ is expected to be of the order of 0.3–0.6 GeV^{-1}, typical of the proton size. The first power term characterized by α represents the scaling violations associated with hard production. Typical values of α are 4–6 for single particle production. The second power term characterized by β represents the kinematic suppression effect at the edges of the phase space of particle production.

The ratios between the data and the smeared ansatz are shown in Fig. 34, where the ansatz correctly describes the data in all y bins. The unsmearing corrections for the p_T resolution effects are shown by the dashed lines in Fig. 35. The unfolding corrections are (10–40)% in the CC, (20–80)% in the ICR where the jet p_T resolution is worse, and (15–80)% in the EC where the jet cross section falls steeply. The highest p_T bin (where the unfolding corrections are the largest) where the cross section is measured is chosen so that the cross section measurement is still meaningful; the number of events should still be sufficient to give a lower limit on the measured cross section at the 95% C.L. ($N_{\mathrm{theory}}/\sqrt{N_{\mathrm{smeared\ theory}}} \geq 1.645$). Although in some bins most of the events migrate from lower p_T, the migrations are well understood and result in a relatively small uncertainty compared to the uncertainty from the jet energy scale. The ansatz unfolding is found to be in good agreement with the results using the PYTHIA MC where the cross section is rescaled to data and the jets at particle level are smeared according to the p_T resolutions obtained in Sec. XI.

The same ansatz unfolding method can be used to unfold the cross section for effects of the resolution for resolving rapidity, assuming the p_T and y resolutions are uncorrelated. Since the y resolution is much better than the p_T resolution, the effects of the y resolution are a small perturbation on top of the p_T smearing. The fits to the unfolded p_T spectra (unfolded for p_T resolution effects only) in neighboring rapidity bins are interpolated with respect to rapidity to produce a smooth, continuous two dimensional spectrum in p_T and y. A final unfolding is performed to correct for events that migrate into neighboring rapidity regions due to effects of the y resolution. The results of the y unfolding as a function of jet p_T in the different y bins are given in Fig. 35, together with the results of the global unfolding corrections in jet p_T and y. As expected, the effects of y unfolding are very small with respect to the effects of the p_T unfolding.

XII. INCLUSIVE JET p_T CROSS SECTION MEASUREMENT

In this section, we describe the final result on the inclusive jet p_T cross section measurement applying the corrections defined in the previous sections: jet energy scale, efficiencies, and unfolding, used in order to compute the true number of events observed in each p_T and y bin. The cross section results are given in Fig. 36 in the six y bins as a function of jet p_T. The data points are plotted according to the prescription described in [28] and the tabulated data are available from Ref. [29].

The method used to extract the cross section is repeated and cross checked using a MC simulation of the detector. Events are generated using PYTHIA and weighted to match the NLO prediction calculated using the CTEQ6.5M PDFs and including nonperturbative corrections. The MC events are treated in the same way as data, all corrections are rederived using MC events,

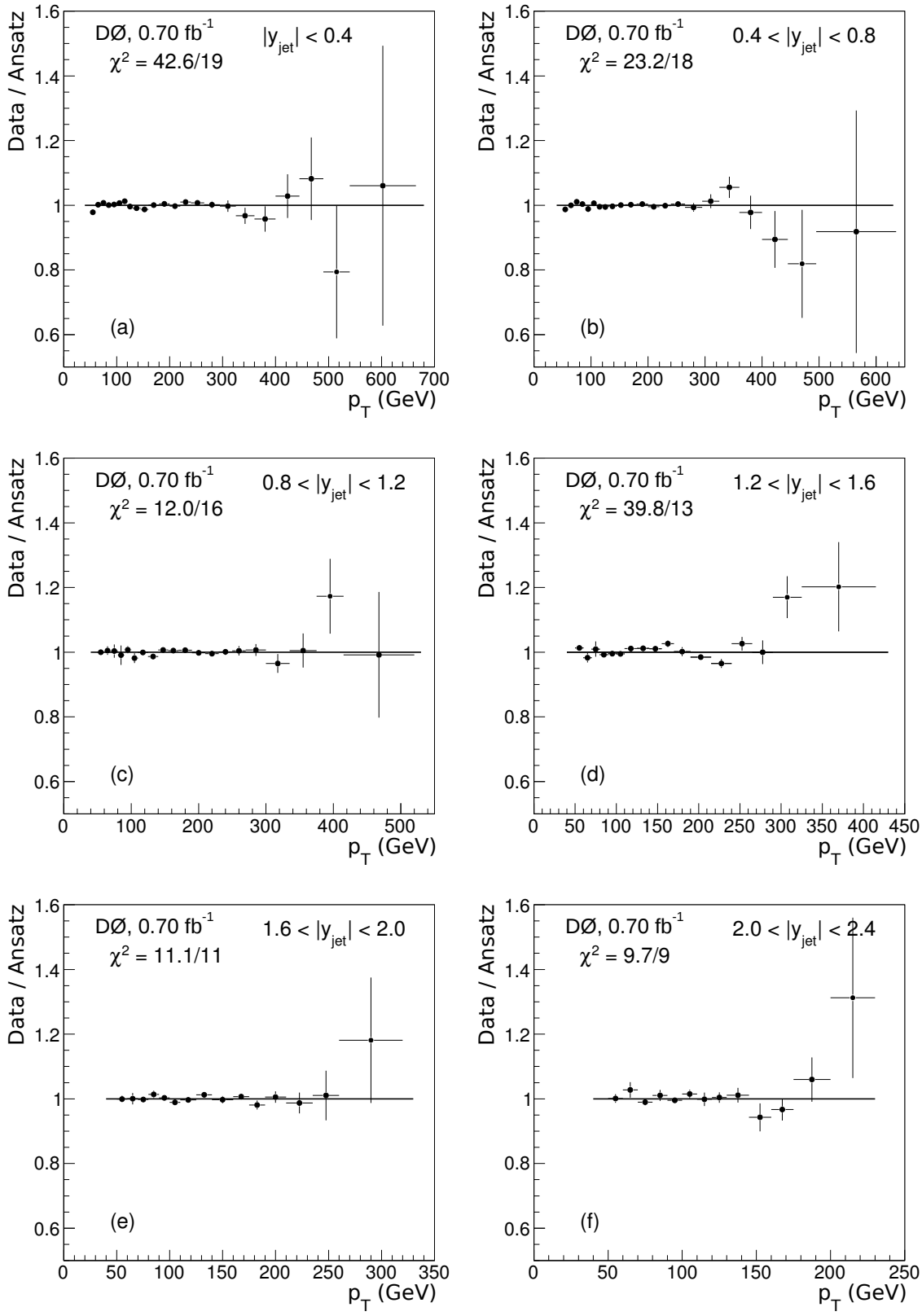

FIG. 34: Data divided by the ansatz fit with models for p_T and y smearing in the six rapidity regions.

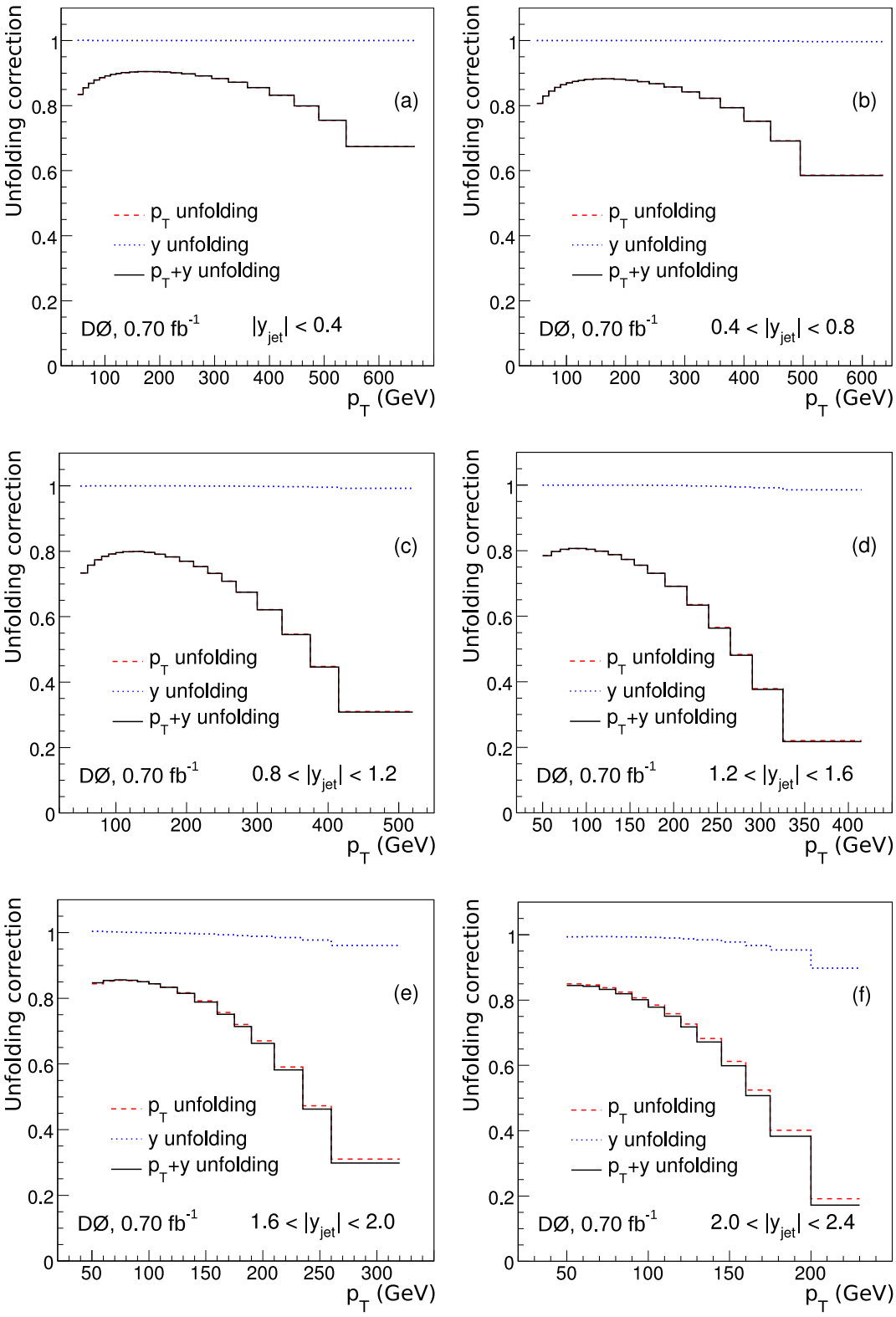

FIG. 35: (color online) Unfolding corrections in the six rapidity regions as a function of jet p_T. The corrections are given for p_T, y unfolding separately and combined.

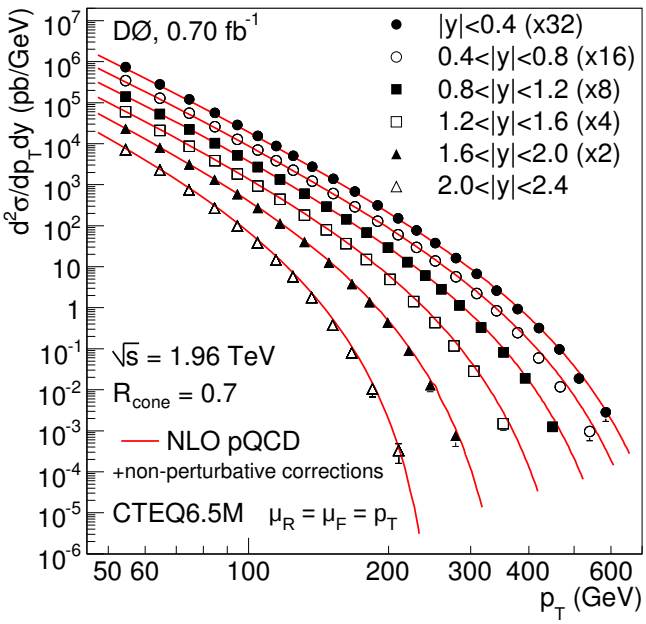

FIG. 36: (color online) Inclusive jet cross section measurements as a function of jet p_T in six $|y|$ bins. The data points are multiplied by 2, 4, 8, 16, and 32 for the bins $1.6 < |y| < 2.0$, $1.2 < |y| < 1.6$, $0.8 < |y| < 1.2$, $0.4 < |y| < 0.8$, and $|y| < 0.4$, respectively.

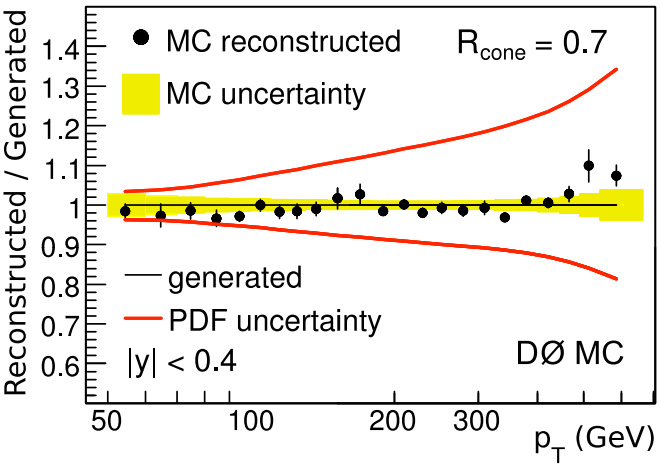

FIG. 37: (color online) MC closure test of the method used to extract the inclusive jet p_T cross section for the jet $|y| < 0.4$ bin. The full analysis was repeated treating MC events as data and comparing the result to the input cross section. Good agreement is found within the statistical uncertainties of fits to jet energy scale and resolution, and unfolding present in MC (shaded band), which are much smaller than the systematic uncertainties in data.

and the derived cross section is compared to the input cross section to perform a closure test of the measurement. The results given in Fig. 37 show that the method used to extract the cross section works well within the statistical uncertainties of the fits to the jet response, jet p_T resolution and p_T spectrum. These MC uncertainties are significantly smaller than the systematic uncertainties present in data.

In Fig. 36 the measurement is compared to the prediction of NLO QCD using the CTEQ6.5M PDF parameterization computed using the NLOJET++ program and FastNLO. The central CTEQ6.5M prediction uses the factorization and renormalization scales $\mu_F = \mu_R = p_T$. The alternative scale choices $\mu_F = \mu_R = 0.5p_T$ and $\mu_F = \mu_R = 2p_T$ are used to estimate the theoretical uncertainty on the higher order corrections.

The NLO PQCD prediction is corrected for non-perturbative effects to connect the parton level jets predicted by theory to the measured particle level jets. The leading non-perturbative corrections are hadronization and underlying event which partially cancel. Another small correction is the exclusion of muons and neutrinos from the definition of the particle jets. The muon/neutrino energy loss is not corrected by the JES procedure using the MPF method in γ+jet events. The MC corrections have been obtained using Pythia v6.412 with parameters for tune QW [30] obtained by tuning Pythia to reproduce CDF Run II data. The strong coupling constant is fixed to $\alpha_s(M_Z) = 0.118$ at the Z boson mass and uses the 2-loop formula for the Q^2 evolution of α_s. The Pythia cross section is reweighted in $\hat{s}$ so that the Pythia parton shower prediction agrees with NLO pQCD. The correction factors for hadronization and the underlying event are shown in Fig. 38. As shown in Fig. 36, the measurement is well described by NLO QCD over eight orders of magnitude in the six y bins.

To check more precisely how well the measurement is described by the NLO QCD theory, we display the ratio of data over theory in Fig. 39, where the theory is calculated using the CTEQ6.5M PDF parameterization. The PDF uncertainties represented as dashed lines are calculated using the set of 20 eigenvectors provided by the CTEQ Collaboration for the CTEQ6.5M PDF fits. Data and theory agree within experimental and theoretical uncertainties, but data seems to favor the lower end of the CTEQ6.5M PDF 90% confidence level uncertainty band. Data are also compared to the NLO QCD calculations using the MRST2004 PDF parameterization and our agreement in shape is good. The experimental uncertainties are smaller than the present PDF uncertainties, so these data further constrain the PDFs.

Some recent parameterizations have already used our measured jet cross sections described here to further constrain the PDFs. As an example, we display in Fig. 40 the ratio data over theory, where the NLO theory is calculated using the MSTW08 NLO PDF [31] which displays good agreement between our measurement and this parameterization, with a tendency to be slightly different at high jet p_T where the uncertainties are larger. For reference, we also display in Fig. 41 the ratio of data over theory where the theory uses the recent HERA-PDFv1.0 PDF [32], which uses only HERA data to con-

strain PDFs. We notice some discrepancies between our measurement and the HERAPDFv1.0 PDF at medium jet p_T especially in the central region, and at high p_T in the forward region. We also compare our data with the ABKM09NLO [33] parameterization in Fig. 42 and we notice some disagreement between our data and the predictions in particular on the normalization. This shows the capability of our data to constrain further the PDFs. Furthermore, we compare our measurements to the recent CT10 [34] parameterization in Fig. 43. There is a good agreement with data with the tendency of the CT10 parameterization to be higher at large p_T in all $|y|$ bins. Finally, we compare our measurement with the predictions from the NNPDFv2.1 [35] parameterization in Fig. 44 and again good agreement is found with our data.

The details of the uncertainties on the inclusive jet p_T cross section are given in Fig. 45. The dominant uncertainty is due to the systematic uncertainties on the jet energy scale, but the unfolding and the uncertainties related to the resolution in jet p_T are also important, especially at high p_T and high $|y|$. The 6.1% luminosity uncertainty is the second largest uncertainty at low p_T and the third largest at high p_T, and leads to significant uncertainty in the overall normalization of the cross section. For a jet $p_T \approx 150$ GeV, it is similar to the jet energy scale uncertainty. The uncertainties related to efficiencies are small everywhere.

XIII. UNCERTAINTY CORRELATIONS

Correlations between systematic uncertainties are studied in detail to increase the value of these data in future fits to model parton distributions and their impact on LHC physics predictions in particular. In total, there are 91 independent sources of systematic uncertainty, and in this section we describe the method we use to group those with similar impact on the shape of the cross section to find the principal components of the uncertainty without significantly impacting the overall quality of the data. Many of the systematic sources we describe above are small in magnitude and highly correlated in shape with other sources.

The traditional interpretation of uncertainties to be independent requires that at each point the sum of all sources in quadrature must equal the total systematic uncertainty. In practice, adding in quadrature sources with similar shapes whose orthogonal components (defined later) are small will lose very little information compared to the full information given in the 91 different systematic uncertainties.

We combine uncertainties that are correlated and of similar shape to reduce the number of components in the covariance matrix. We develop a robust systematic approach for regrouping the sources based on the notions of source size, shape similarity, and orthogonality. The natural measure for the size of a source is the impact it has on the overall χ^2 in the fit with the ansatz function when shifted by one standard deviation around the minimum. To assess the similarity in shape between different systematic uncertainties, we define the inner product for sources h and g as

$$\langle h \cdot g \rangle = \sum_{i \in \text{bins}} \frac{h_i \cdot g_i}{\sigma^2_{\text{stat},i}}, \tag{32}$$

where h_i and g_i are the values of two systematic uncertainties and the sum is over the p_T and $|y|$ bins. The size, or magnitude, of a source h can be written using this notation as

$$||h|| = \sqrt{\langle h \cdot h \rangle}. \tag{33}$$

The shape similarity of two sources h and g can be quantified by calculating their correlation, which is written in the notation of Eq. 32 as

$$\rho = \frac{\langle h \cdot g \rangle}{||h|| \cdot ||g||}, \tag{34}$$

which varies between -1.0 and 1.0. When ρ =1.0, the sources are fully correlated, -1.0 fully anti-correlated and 0.0 completely uncorrelated. The source g can be broken into a component that is fully correlated with source h and another component that is fully uncorrelated by considering a linear transformation

$$g' = g - \alpha h. \tag{35}$$

When the orthogonality of h and g' is defined in terms of the inner product,

$$h \perp g' \equiv \langle h \cdot g' \rangle = 0, \tag{36}$$

Eq. 35 and Eq. 36 together yield

$$\alpha = \frac{\langle h \cdot g \rangle}{\langle h \cdot h \rangle}, \tag{37}$$

defining g' as the orthogonal component that is fully uncorrelated with source h. The value g' has the property $\langle g' \cdot g' \rangle \leq \langle g \cdot g \rangle$, $\langle g' \cdot g' \rangle = \langle g \cdot g \rangle$ is equivalent to h being orthogonal to g, and $\langle g' \cdot g' \rangle = 0$ to h being parallel to g. Small values of $||g'||$ indicate that the sources can be combined with little impact on the freedom of the fit to the ansatz.

The sources due to statistical uncertainties in fits are first assigned as uncorrelated. The remaining sources are sorted by size and are then iteratively recombined with other sources most similar in shape and having the smallest orthogonal components. The sources are combined when their correlation is greater than about 85% and the orthogonal components have a magnitude smaller than 10% of the largest individual systematic $\epsilon_{\max}$. At the end of the iterative procedure, the remaining set of sources no longer has any pairings with an orthogonal component less than $0.1\epsilon_{\max}$. The smallest remaining sources with

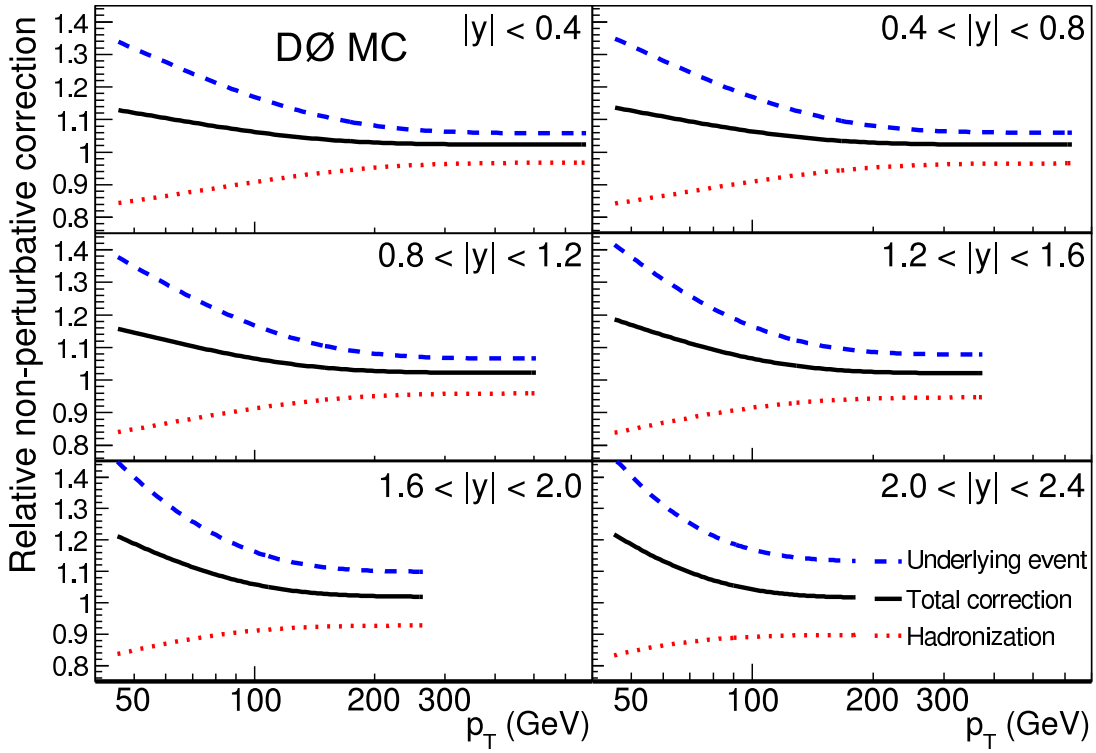

FIG. 38: (color online) Hadronization (dashed line) and underlying event (dotted line) corrections for inclusive jet cross section and the product of both corrections (solid line). The uncertainty on the theory is estimated as 50% of the individual corrections added in quadrature.

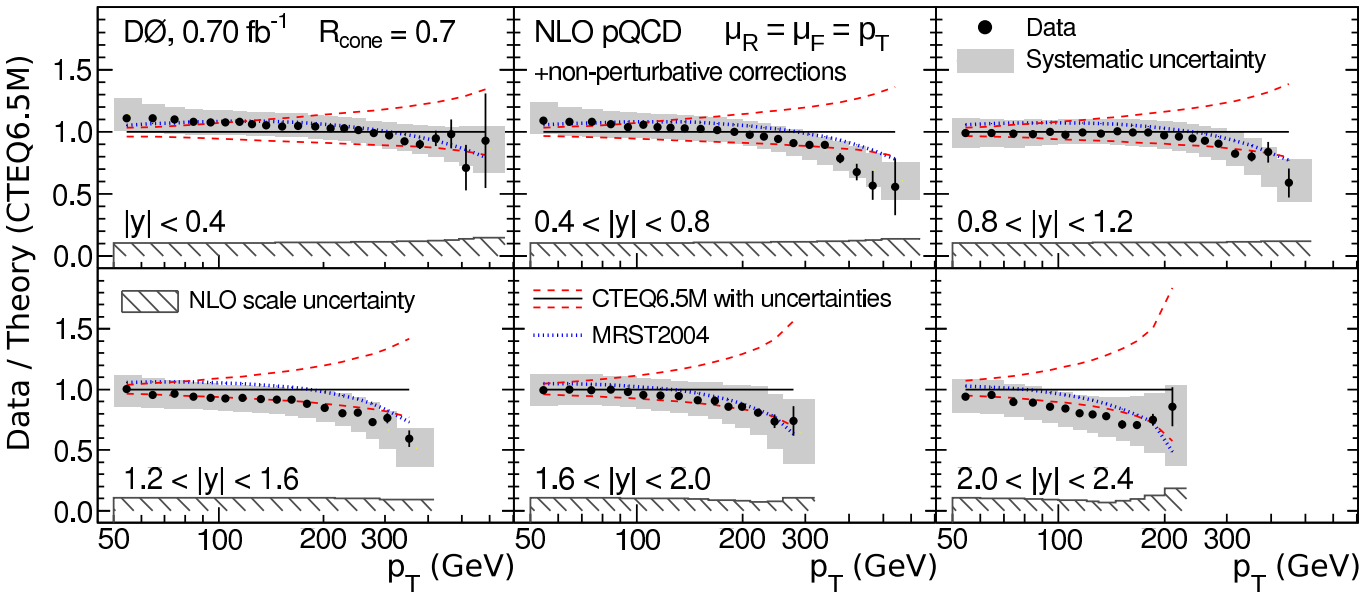

FIG. 39: (color online) Measured data divided by theory for the inclusive jet cross section as a function of jet p_T in the six $|y|$ bins. The data systematic uncertainties are displayed by the shaded band. NLO pQCD calculations, with renormalization and factorization scales set to jet p_T using the CTEQ6.5M PDFs and including non-perturbative corrections, are compared to the data. The CTEQ6.5 PDF uncertainties are shown as dashed lines and the predictions with MRST2004 PDFs as dotted lines. The theoretical uncertainty, determined by changing the renormalization and factorization scales between $p_T/2$ and $2p_T$, is shown at the bottom of each figure.

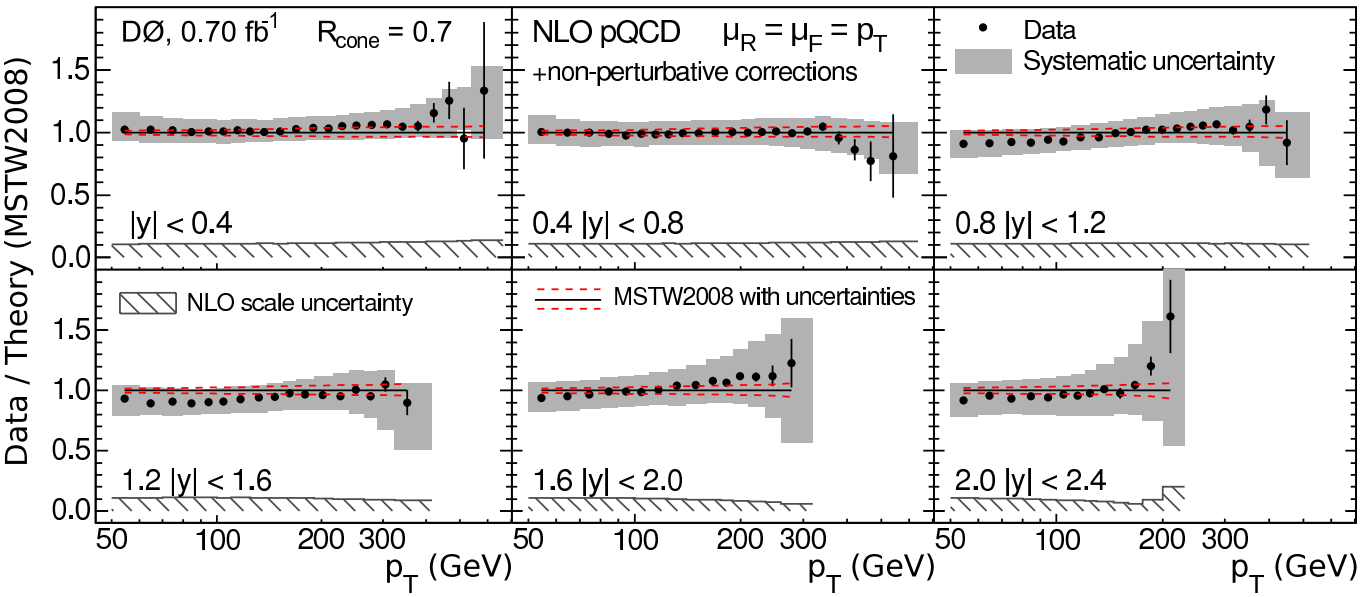

FIG. 40: (color online) Measured data divided by theory for the inclusive jet cross section as a function of jet p_T in the six $|y|$ bins using the MSTW2008 parameterization. The data systematic uncertainties are displayed by the shaded band. The theoretical uncertainty, determined by changing the renormalization and factorization scales between $p_T/2$ and $2p_T$, is shown at the bottom of each figure.

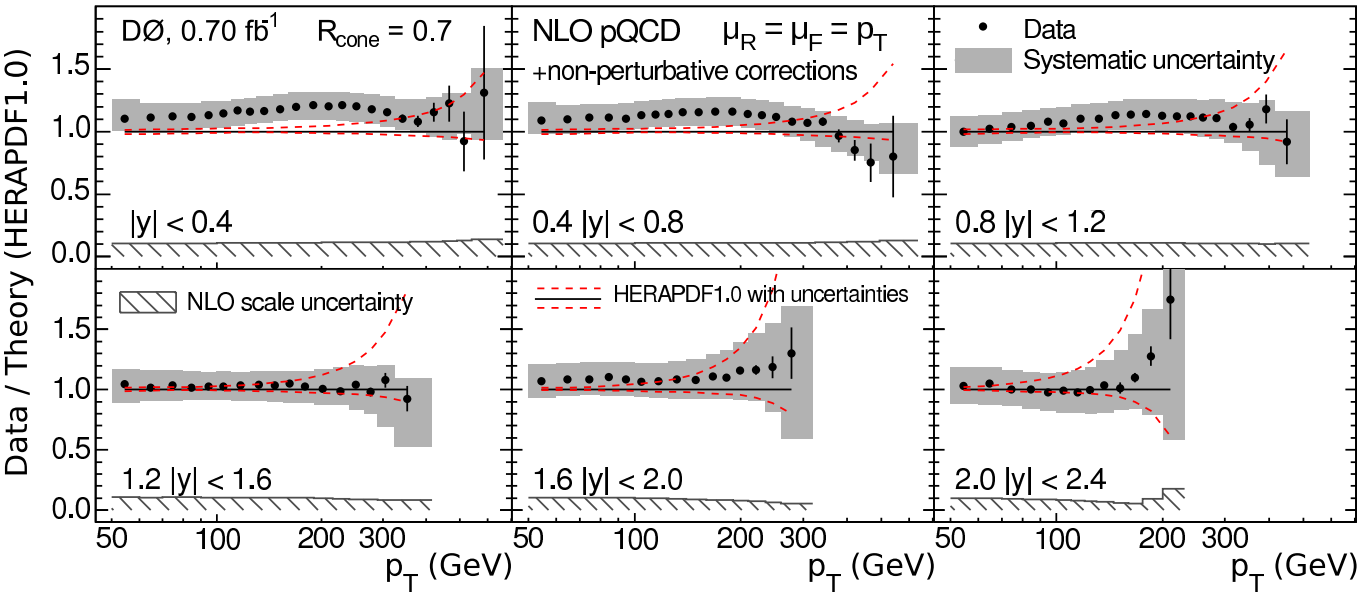

FIG. 41: (color online) Measured data divided by theory for the inclusive jet cross section as a function of jet p_T in the six $|y|$ bins using the HERAPDF1.0 parameterization. The data systematic uncertainties are displayed by the shaded band. The theoretical uncertainty, determined by changing the renormalization and factorization scales between $p_T/2$ and $2p_T$, is shown at the bottom of each figure.

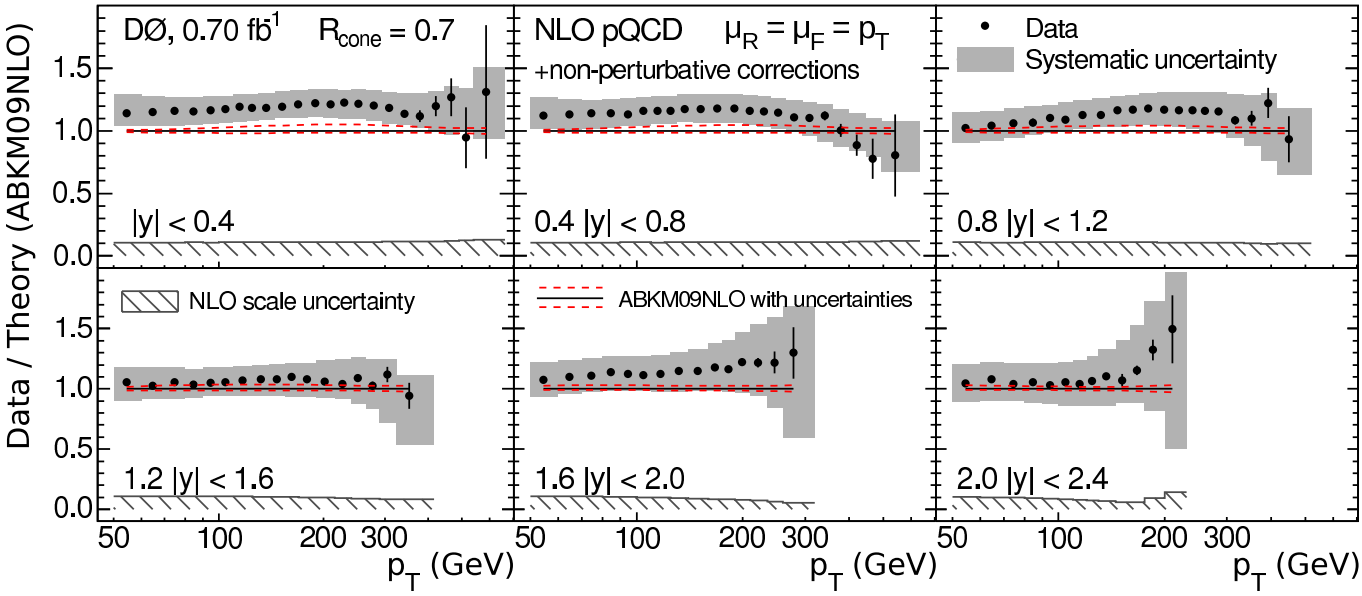

FIG. 42: (color online) Measured data divided by theory for the inclusive jet cross section as a function of jet p_T in the six $|y|$ bins using the ABKM09 parameterization. The data systematic uncertainties are displayed by the shaded band. The theoretical uncertainty, determined by changing the renormalization and factorization scales between $p_T/2$ and $2p_T$, is shown at the bottom of each figure.

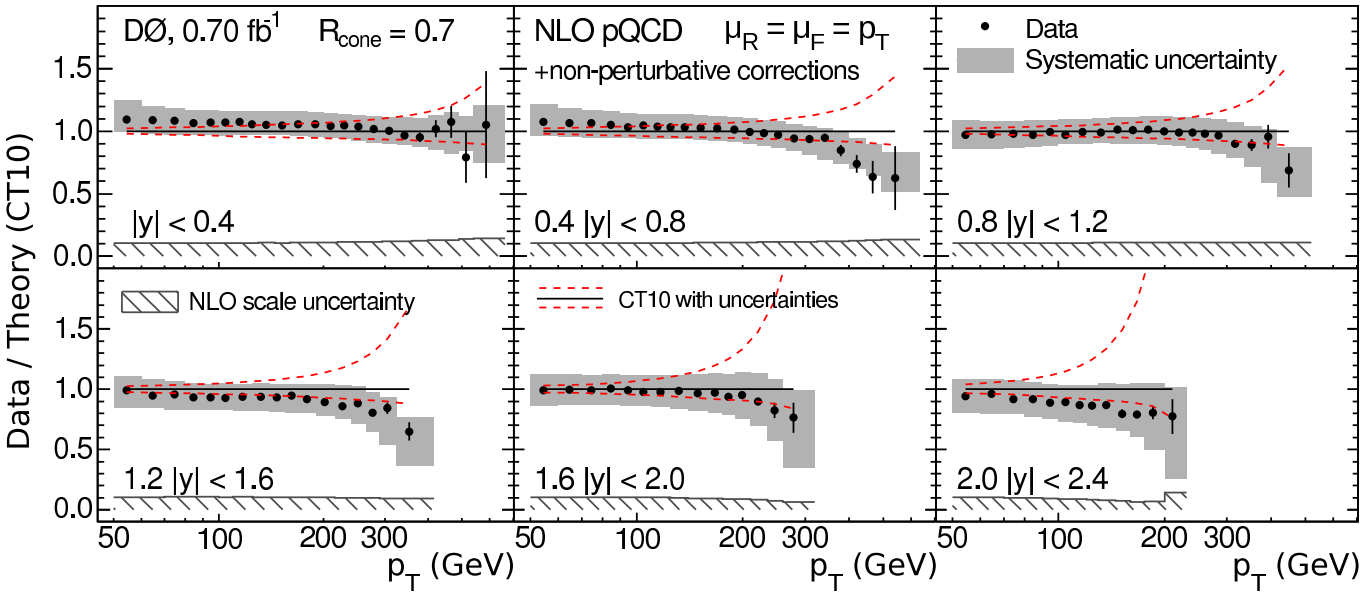

FIG. 43: (color online) Measured data divided by theory for the inclusive jet cross section as a function of jet p_T in the six $|y|$ bins using the CT10 parameterization. The data systematic uncertainties are displayed by the shaded band. The theoretical uncertainty, determined by changing the renormalization and factorization scales between $p_T/2$ and $2p_T$, is shown at the bottom of each figure.

magnitude less than $0.1\epsilon_{\max}$ are added in quadrature to the uncorrelated uncertainty. The final reduced set of uncertainties has 23 correlated sources (principal components) and one fully uncorrelated uncertainty, which is a significant reduction compared to the original 91 sources. The reduced set of 23 correlated sources and the total uncorrelated uncertainty are provided in Ref. [29].

The five leading sources from the reduced set of combined systematic uncertainties, the total uncorrelated uncertainty, and the total uncertainty are shown in Figs. 46 and 47 in the six $|y|$ bins. These sources summarize the leading systematic uncertainties for the measurement. The EM scale uncertainty comes from the calibration of the EM calorimeter using $Z \to e^+e^-$ events. The photon

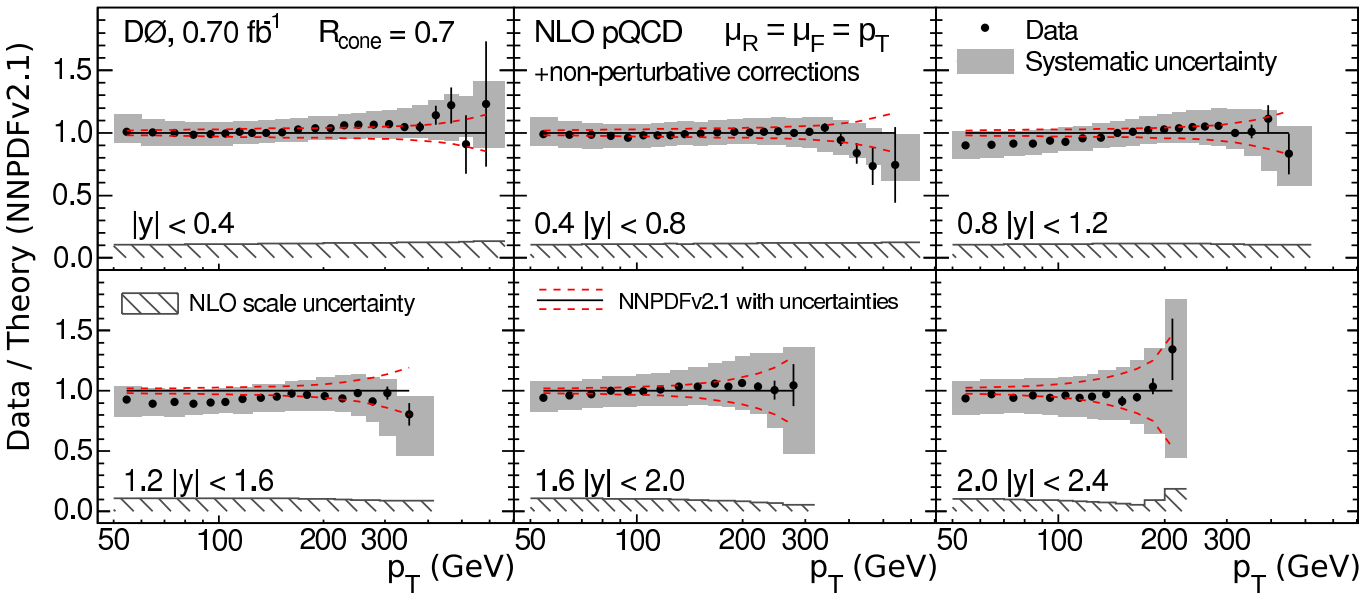

FIG. 44: (color online) Measured data divided by theory for the inclusive jet cross section as a function of jet p_T in the six $|y|$ bins using the NNPDFv2.1 parameterization. The data systematic uncertainties are displayed by the shaded band. The theoretical uncertainty, determined by changing the renormalization and factorization scales between $p_T/2$ and $2p_T$, is shown at the bottom of each figure.

energy scale includes the uncertainty in the MC description of the difference in the electron and photon responses and the uncertainty in the amount of passive material in front of the calorimeter, which affects the response difference as a function of photon p_T. The uncertainty in the high p_T extrapolation is due to differences in fragmentation models of Pythia and Herwig, which lead to an additional uncertainty in the high p_T extrapolation of the central response. The rapidity-intercalibration uncertainty summarizes the uncertainty in the relative response calibration between calorimeter regions. The detector showering uncertainty includes the uncertainties on showering, but also additional significant contributions from other uncertainties such as sample purity and the difference between alternate tunes of Pythia (tunes A and QW).

XIV. CONCLUSION

In this paper, we described the measurement of the inclusive jet cross section by the D0 experiment. The measured inclusive jet cross section corrected for experimental effects to the particle level in $p\bar{p}$ collisions at $\sqrt{s} = 1.96$ TeV with $\mathcal{L} = 0.70$ fb^{-1} was presented for six $|y|$ bins as a function of jet p_T. The precision reached in this measurement is unprecedented for results from a hadron collider, particularly for processes dependent on gluons at high-x. The measurement was found to be in good agreement with NLO QCD calculations with CTEQ6.5M and MRST2004 PDFs. These results will also be useful for any experiment at a hadron collider such as the LHC where the same techniques can be used to extract the jet energy scale with high precision and to measure the inclusive jet cross section. In addition, a full analysis of correlations between sources of systematic uncertainty was performed, demonstrating a useful method to reduce the complexities of describing numerous sources of uncertainties in the cross section, and increasing the potential impact of these data in global PDF fits.

We thank the staffs at Fermilab and collaborating institutions, and acknowledge support from the DOE and NSF (USA); CEA and CNRS/IN2P3 (France); FASI, Rosatom and RFBR (Russia); CNPq, FAPERJ, FAPESP and FUNDUNESP (Brazil); DAE and DST (India); Colciencias (Colombia); CONACyT (Mexico); KRF and KOSEF (Korea); CONICET and UBACyT (Argentina); FOM (The Netherlands); STFC and the Royal Society (United Kingdom); MSMT and GACR (Czech Republic); CRC Program and NSERC (Canada); BMBF and DFG (Germany); SFI (Ireland); The Swedish Research Council (Sweden); and CAS and CNSF (China).

[1] D0 Collaboration, V. M. Abazov *et al.*, Phys. Rev. D **80**,111107 (2009).
[2] A. Belyaev *et al.*, JHEP **01**, 069 (2006).
[3] Z. Nagy, Phys. Rev. D **68**, 094002 (2003) and references therein.
[4] E. Eichten *et al.*, Rev. Mod. Phys. **56**, 579 (1984); **58**,

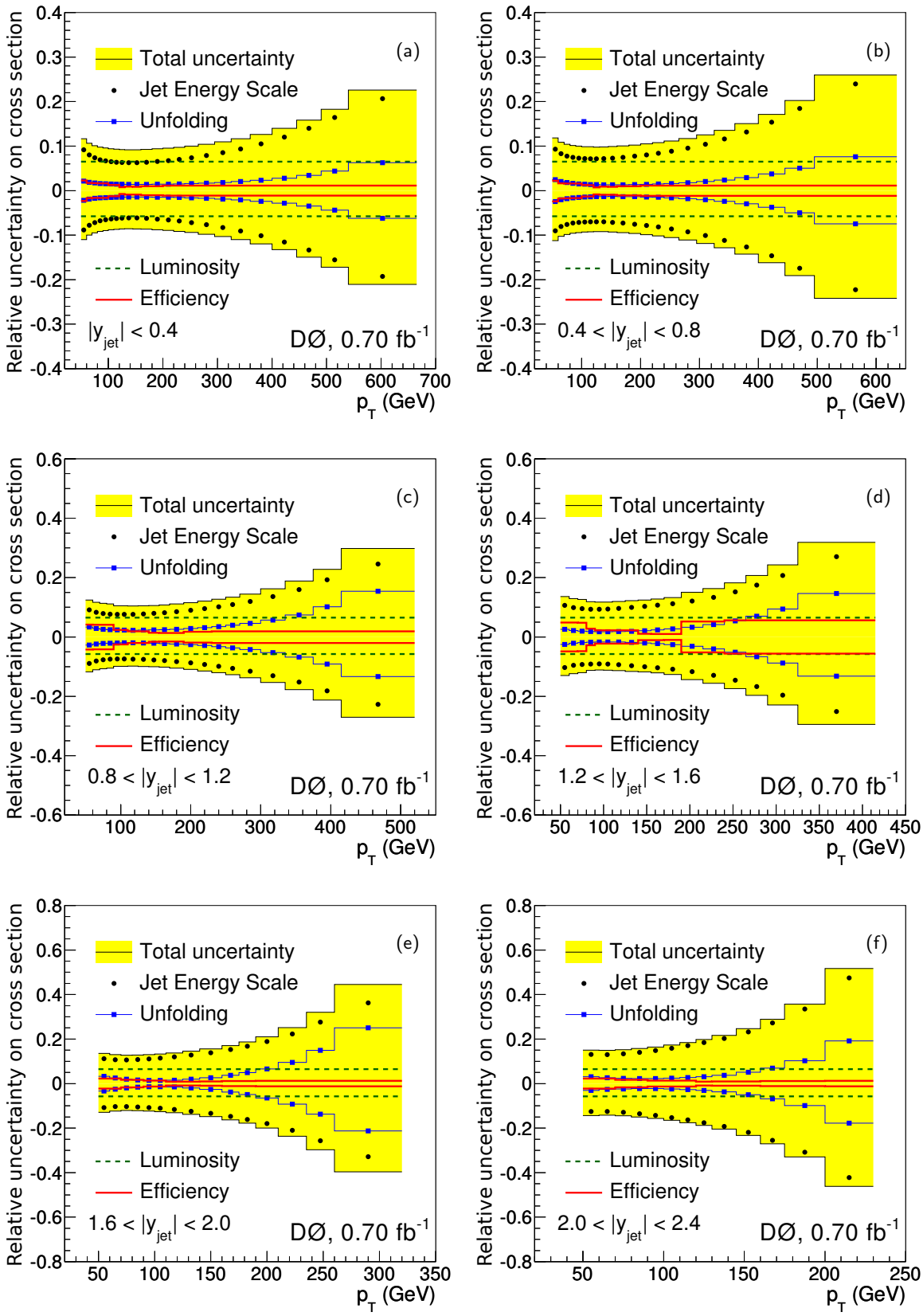

FIG. 45: (color online) Different components of the systematic uncertainty as a function of jet p_T in the six y bins.

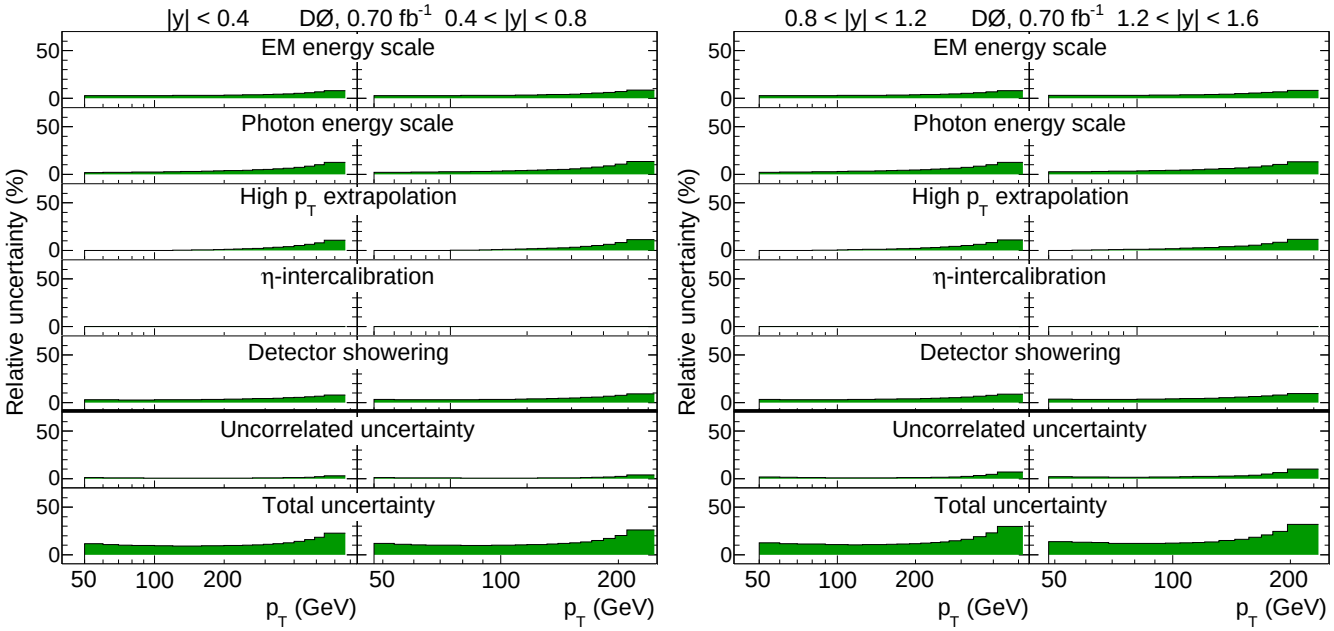

FIG. 46: (color online) Correlated uncertainties for all central regions and the ICR as a function of jet p_T for four $|y|$ bins, $|y| < 0.4$, $0.4 < |y| < 0.8$, $0.8 < |y| < 1.2$, and $1.2 < |y| < 1.6$. The five largest systematic uncertainties are shown together with uncorrelated and total uncertainties, computed as the sum in quadrature of all sources.

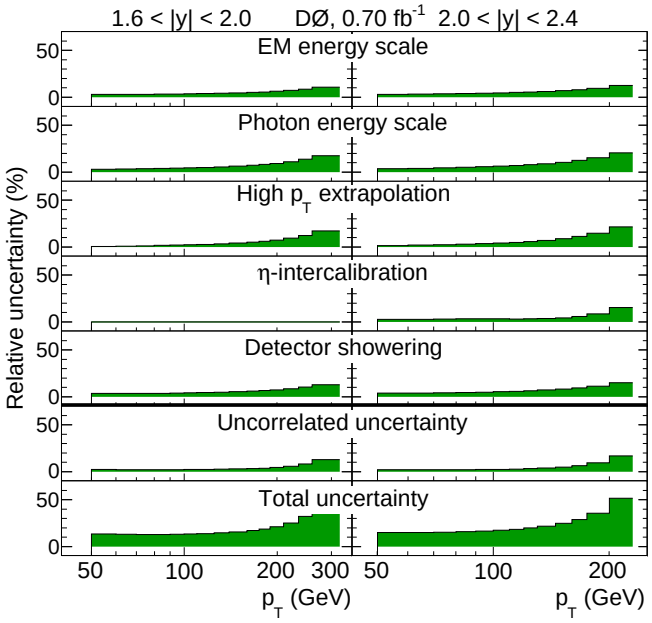

FIG. 47: (color online) Correlated uncertainties for $1.6 < |y| < 2.0$ and $2.0 < |y| < 2.4$ as a function of jet p_T. The five largest systematic uncertainties are shown together with uncorrelated and total uncertainties, computed as the sum in quadrature of all sources.

1065 (1986).

[5] D0 Collaboration, V. M. Abazov *et al.*, Phys. Rev. Lett. **101**, 062001 (2008).

[6] M. Voutilainen, Fermilab thesis FERMILAB-THESIS-2008-19 (2008).

[7] T. Andeen *et al.*, Fermilab report FERMILAB-TM-2365 (2007).

[8] CDF Collaboration, T. Aaltonen *et al.*, Phys. Rev. D **78**, 052006 (2008).

[9] CDF Collaboration, A. Abulencia *et al.*, Phys. Rev. D **75**, 092006 (2007); CDF Collaboration, A. Abulencia *et al.*, Phys. Rev. D **74**, 071103 (2006).

[10] D0 Collaboration, B. Abbott *et al.*, Phys. Rev. Lett. **82**, 2451 (1999);
Phys. Rev. Lett. **86**, 1707 (2001);

[11] CDF Collaboration, F. Abe *et al.*, Phys. Rev. Lett. **77**, 438 (1996).

[12] D0 Collaboration, V. M. Abazov *et al.*, Nucl. Instrum. Methods Phys. Res. A **565**, 463 (2006).

[13] D0 Collaboration, S. Abachi *et al.*, Nucl. Instrum. Methods Phys. Res. A **338**, 185 (1994).

[14] S. Klimenko, J. Konigsberg, T.M. Liss, Fermilab-FN-0741 (2003).

[15] G.C. Blazey *et al.*, in *Proceedings of the Workshop: "QCD and Weak Boson Physics in Run II"*, edited by U. Baur, R.K. Ellis, and D. Zeppenfeld, Batavia, Illinois (2000) p. 47.

[16] T. Kluge, K. Rabbertz, and M. Wobisch, arXiv:hep-ph/0609285.

[17] W.K. Tung *et al.*, JHEP **02**, 053 (2007);
J. Pumplin *et al.*, JHEP **07**, 12 (2002);
D. Stump *et al.*, JHEP **10**, 046 (2003).

[18] A.D. Martin *et al.*, Phys. Lett. B **604**, 61 (2004).

[19] A.D. Martin *et al.*, Eur. Phys. J. C **63**, 189 (2009).

[20] Buttar *et al.*, arXiv:hep-ph/0803.0678 [hep-ph].

[21] D0 Collaboration, B. Abbott *et al*, Nucl. Inst. Meth. Phys. Res. A **424**, 352 (1999).

[22] V.M. Abazov *et al.*, Phys. Rev. Lett. **103** 141801 (2009).

[23] D0 Collaboration, V. M. Abazov *et al.*, Phys. Lett. B **666**, 435 (2008).

[24] T. Sjöstrand *et al.*, Comp. Phys. Comm. **135**, 238 (2001).

[25] D0 Collaboration, V. M. Abazov *et al.*, Phys. Lett. B **639**, 151 (2006).

[26] G. Marchesini *et al.*, Comp. Phys. Comm. **67**, 465 (1992).

[27] S.M. Berman, J.D. Bjorken, and J.B. Kogut, Phys. Rev. D **4**, 3388 (1971);
R.P. Feynman, R.D. Field, and G.C. Fox, Phys. Rev. D **18** 3320 (1978).

[28] G.D. Lafferty and, T.R. Wyatt, Nucl. Instrum. Methods Phys. Res. A **355**, 541 (1995).

[29] Measurements and correlations are available at `http://hepdata.cedar.ac.uk/View/7662670`

[30] R. Field in M.G. Albrow *et al.* [TeV4LHC QCD Working Group], arXiv:hep-ph/0610012.

[31] A.D. Martin *et al.*, Eur. Phys. J. C **63**, 189 (2009).

[32] F.D. Aaron *et al.*, JHEP **01**, 109 (2010).

[33] S. Alekhin *et al.*, Phys. Rev. D**81** 014032 (2010).

[34] H.-L. Lai *et al.*, Phys. Rev. D **82**, 074024 (2010).

[35] R. D. Ball *et al.*, Nucl.Phys. B **838**, 136 (2010).